Exploring the role of *LZTR1* in an autosomal recessive form of Noonan Syndrome by genome-edited induced pluripotent stem cells

Dissertation

for the award of the degree

“Doctor rerum naturalium”

of the Georg-August-Universität Göttingen

within the doctoral program Molecular Medicine

of the Georg-August University School of Science (GAUSS)

submitted by

Robin Hindmarsh

born in Berlin, Germany

Göttingen, May 2021

Thesis Committee Members

Prof. Dr. med. Bernd Wollnik (first reviewer)
Institute of Human Genetics
University Medical Center Göttingen

Prof. Dr. med. Wolfram-Hubertus Zimmermann (second reviewer)
Institute of Pharmacology and Toxicology
University Medical Center Göttingen

Prof. Dr. med. Ralf Dressel
Institute for Cellular and Molecular Immunology
University Medical Center Göttingen

Additional Members of the Examination Board

PD Dr. rer. nat. Sven Thoms
Department of Child and Adolescent Health
University Medical Center Göttingen

PD Dr. rer. nat. Laura Zelarayán-Behrend
Institute of Pharmacology and Toxicology
University Medical Center Göttingen

Dr. rer. nat. Lukas Cyganek
Department of Cardiology and Pneumonology
University Medical Center Göttingen

PD Dr. rer. nat. Katrin Streckfuß-Bömeke
Department of Cardiology and Pneumonology
University Medical Center Göttingen

Date of oral examination: 21.07.2021

Affidavit

Here I declare that my doctoral thesis entitled

“Exploring the role of *LZTR1* in an autosomal recessive form of Noonan syndrome by genome-edited induced pluripotent stem cells”

has been written independently with no other sources and aids than quoted.

_____

Robin Hindmarsh

Göttingen, 15.05.2021

List of publications

Ulrich Hanses, Mandy Kleinsorge, Lennart Roos, Gökhan Yigit, Yun Li , Boris Barbarics, Ibrahim El-Battrawy, Huan Lan, Malte Tiburcy, **Robin Hindmarsh**, Christof Lenz, Gabriela Salinas, Sebastian Diecke, Christian Müller, Ibrahim Adham, Janine Altmüller, Peter Nürnberg, Thomas Paul, Wolfram-Hubertus Zimmermann, Gerd Hasenfuss, Bernd Wollnik, Lukas Cyganek (2020): Intronic CRISPR Repair in a Preclinical Model of Noonan Syndrome-Associated Cardiomyopathy. In: *Circulation* 142 (11), S. 1059–1076. DOI: 10.1161/CIRCULATIONAHA.119.044794

Jonas Peper, Daniel Kownatzki-Danger, Gunnar Weninger, Fitzwilliam Seibertz, Julius Ryan D. Pronto, Henry Sutanto, David Pacheu-Grau, **Robin Hindmarsh**, Sören Brandenburg, Tobias Kohl, Gerd Hasenfuss, Michael Gotthardt, Eva A. Rog-Zielinska, Bernd Wollnik, Peter Rehling, Henning Urlaub, Jörg Wegener, Jordi Heijman, Niels Voigt, Lukas Cyganek, Christof Lenz, Stephan E. Lehnart (2021): Caveolin3 Stabilizes McT1-Mediated Lactate/Proton Transport in Cardiomyocytes. In: *Circulation research* 128 (6), e102-e120. DOI: 10.1161/CIRCRESAHA.119.316547.

Für meine Tochter

Hanna Malina

Table of content

List of figures

List of tables

List of abbreviations

AU	Arbitrary unit
BACK	BTB and C-terminal Kelch
bp	Base pairs
BSA	Bovine serum albumin
BTB	Broad-Complex, Tramtrack and Bric a brac
Cas9	CRISPR associated 9 enzyme
CaT	Calcium transient
cDNA	Complementary DNA
CHF	Congestive heart failure
CM	Cardiomyocyte
CMV	Cytomegalovirus
CRISPR	Clustered regularly interspaced short palindromic repeats
crRNA	CRISPR-RNA
CUL3	Cullin 3
CV	Conduction velocity
DMEM	Dulbecco's Modified Eagle Medium
DMSO	Dimethyl sulfoxide
DNA	Deoxyribonucleic acid
DSB	Double strand break
EEA1	Early Endosome Antigen 1
EDTA	Ethylenediaminetetraacetic acid
ERK1/2	Extracellular signal-regulated kinase 1/2
ESC	Embryonic stem cell
FBS	Fetal bovine serum
FGF	Fibroblast growth factor
FPDc	Field potential duration with Fridericia correction
GAP	GTPase-activating protein
GAPDH	Glyceraldehyde 3-phosphate dehydrogenase
gDNA	Genomic DNA
GEF	Nucleotide exchange factor
GRB2	Adaptor protein growth factor receptor-bound protein 2
gRNA	Guide RNA
GSK3	Glycogen synthase kinase 3
HA	Hemagglutinin
HCl	Hydrochloric acid
HCM	Hypertrophic cardiomyopathy
HDR	Homology directed repair
HEK	Human embryonic kidney
HEPES	4-(2-hydroxyethyl)-1-piperazineethanesulfonic acid
HRAS	Harvey Rat Sarcoma Viral Oncogene Homolog
HRP	Horseradish peroxidase
indel	Insertion or deletion
iPSC	Induced pluripotent stem cell
iPSC-CM	Induced pluripotent stem cell derived cardiomyocyte

IWP-2	Inhibitor of Wnt production 2
KCl	Potassium Chloride
kDa	Kilodalton
KI	Knock-in
KLF4	Krüppel-like factor 4
KO	Knock-out
LAMP1	Lysosomal-associated membrane protein 1
LZTR1	Leucine zipper like transcription regulator 1
MAPK	Mitogen-activated protein kinases
MEA	Microelectrode array
MEK1/2	Mitogen-activated protein kinase kinases
MEM	Minimum Essential Medium
MG132	Benzyl *N*-[(2*S*)-4-methyl-1-[[(2*S*)-4-methyl-1-[[(2*S*)-4-methyl-1-oxopentan-2-yl]amino]-1-oxopentan-2-yl]amino]-1-oxopentan-2-yl]carbamate
MRAS	Muscle RAS Oncogene Homolog
mRNA	Messenger RNA
NaOH	Sodium hydroxide solution
NEAA	Non-essential amino acids
NHEJ	Non-homologous end joining
NRAS	Neuroblastoma RAS Viral Oncogene Homolog
NS	Noonan syndrome
OCT3/4	Octamer-binding transcription factor
PAM	Protospacer adjacent motif
PBS	Phosphate buffered saline
PCR	Polymerase chain reaction
PEX14	Peroxisomal membrane protein PEX14
RAB5	Ras-related protein Rab-5A
RAB11	Ras-related protein Rab-11A
RAS	Rat sarcoma
RNA	Ribonucleic acid
RNP	Ribonucleoprotein
rpm	Revolutions per minute
RPMI	Roswell Park Memorial Institute Medium
RT	Room temperature
RTK	Receptor tyrosine kinase
RT-qPCR	Quantitative real-time PCR
SEM	Standard error of the mean
SHC	Signaling and transforming protein containing Src homology 2 and 3 (SH2 and SH3) domains
SHP-2	Src homology region 2-domain phosphatase 2
SOS	Son-of-sevenless
SOX2	Sex determining region Y-box 2
SR	Sarcoplasmic reticulum
TBE	Tris/borate/EDTA buffer
TBS-T	Tris buffered saline with Tween-20
tracr-RNA	Trans-activating crRNA

TRIS	Tris(hydroxymethyl)aminomethan
TZV	Thiazovivin
WT	Wild type

1 Abstract

Noonan syndrome is a multisystemic developmental disorder and is characterized by variable symptoms such as facial dysmorphisms, short stature, webbing of the neck and mild intellectual disability. The most severe clinical feature of this disease is an early onset and often life-threatening hypertrophic cardiomyopathy. Noonan syndrome belongs to the class of RASopathies, which share increased activity of the RAS-MAPK pathway as a common feature. In a previous study, we presented a family with two children that were diagnosed with a rare recessive form of Noonan syndrome at 6 months and 3 years of age. Whole-exome sequencing revealed a biallelic loss of *LZTR1*, a gene whose functions were first described in 2018 as a mediator for RAS ubiquitination and degradation. Within recent years, *LZTR1* emerged as an etiologic factor in Noonan syndrome and dysfunctions are associated with a hyperactivation of the RAS-MAPK signaling pathway. Interestingly, this disorder caused by *LZTR1* dysfunction can be inherited in an autosomal dominant or an autosomal recessive manner, depending on the position of the mutation. However, most studies that investigated functions of *LZTR1* and its connection to Noonan syndrome were conducted in HEK293T cells or murine systems that have limited capacities to model human cardiac diseases. Thus, many open questions mainly regarding cardiac related fields remained unsolved. To further elucidate the effects of *LZTR1* loss in a cardiac related system, we generated *LZTR1*-deficient iPSC-CMs via CRISPR/Cas9, mimicking both the maternal and paternal mutations of the familial case of Noonan syndrome. We were able to demonstrate that biallelic but not monoallelic *LZTR1* loss increased RAS protein abundance in iPSC-CMs. Additionally, we showed that overexpression of full-length but not truncated LZTR1 in HEK293T cells reduced RAS protein levels with pronounced affinity for the MRAS isoform. Overexpression of full-length LZTR1 in iPSC-CMs showed a clearly spotted, vesicular like structure and high degree of co-localization with different RAS isoforms and CUL3, a key player in the ubiquitin-proteasome machinery. Strikingly, the subcellular localization of a truncated LZTR1 variant, resembling the paternal mutation from the familial Noonan syndrome case, showed homogenous cytosolic distribution. This led to a new proposed model for LZTR1 function, explaining the variable symptoms of the disease with different available level of functional LZTR1 proteins. Although the hypertrophic cardiac phenotype of Noonan syndrome patients was not reproducible in *LZTR1*-deficient iPSC-CMs, we observed an abnormal calcium handling, allowing first insights into the impact of *LZTR1* loss in a physiological, cardiac related cell system. In conclusion, the findings from this thesis further fortify the role of LZTR1 as a negative regulator of the RAS-MAPK signaling pathway by RAS degradation.

2 Introduction

2.1 Noonan syndrome

2.1.1 Clinical features of Noonan syndrome

Noonan syndrome (NS) is a multisystemic developmental disorder with a broad spectrum of heterogeneity regarding clinical features and its genetic causes. NS was first described in 1968 by Jacqueline Noonan in a report about 19 patients presenting a Turner syndrome-like phenotype with hypertelorism (Noonan 1968). With a prevalence of 1 in 1.000-2.500 live births (Mendez and Opitz 1985), NS is a relatively common disease and is characterized by its clinical variability with symptoms such as facial dysmorphism including ptosis, low-set ears, hypertelorism and a short webbed neck. General developmental delay and mild intellectual disability are described frequently as well as skeletal anomalies (most commonly sternal deformities), auditory deficits and a short statue (Roberts et al. 2013). Although most cases of NS are mild with patients having an average lifespan, cases with severe disease progression and high mortality rates exist. The primary cause of death of NS patients is congestive heart failure. 80-90% of NS patients display various forms of cardiac abnormities that manifest through early-onset hypertrophic cardiomyopathy (HCM) in 20% of cases (Gelb et al. 2015). This makes NS the second most common cause of congenital heart defects, only exceeded by trisomy 21 (Marino et al. 1999). The characteristics of HCM caused by NS differ in several ways from other forms of HCM associated with mutations of sarcomeric proteins. Compared to other forms of pediatric HCM that are diagnosed on average at 8 years of age, NS-associated HCM typically manifests extremely early in life, with over 50% cases diagnosed by 6 months of age (Wilkinson et al. 2012). Especially within the first two years after diagnosis, the survival rate of NS patients with HCM is significantly lower (Figure 1A). The prevalence of congestive heart failure (CHF) is much higher in NS-associated HCM than in other forms of pediatric HCM (24% vs. 9%) (Hickey et al. 2011; Wilkinson et al. 2012) and is the main determinant of survival rate in early life. While NS patients that suffer from HCM without CHF show a survival rate above 60%, the presence of CHF leads to a significantly lower survival rate 5 years after diagnosis (below 40%) (Figure 1B). A cure for NS does not exist and treatment is targeted towards supportive care and improvement of symptoms. Patients with left ventricular outflow obstruction can undergo surgical intervention and effects of short stature can be addressed by treatment with growth hormones. As multiple organs are affected and due to the high variability of symptoms, treatment remains challenging and is highly individual (Romano et al. 2010).

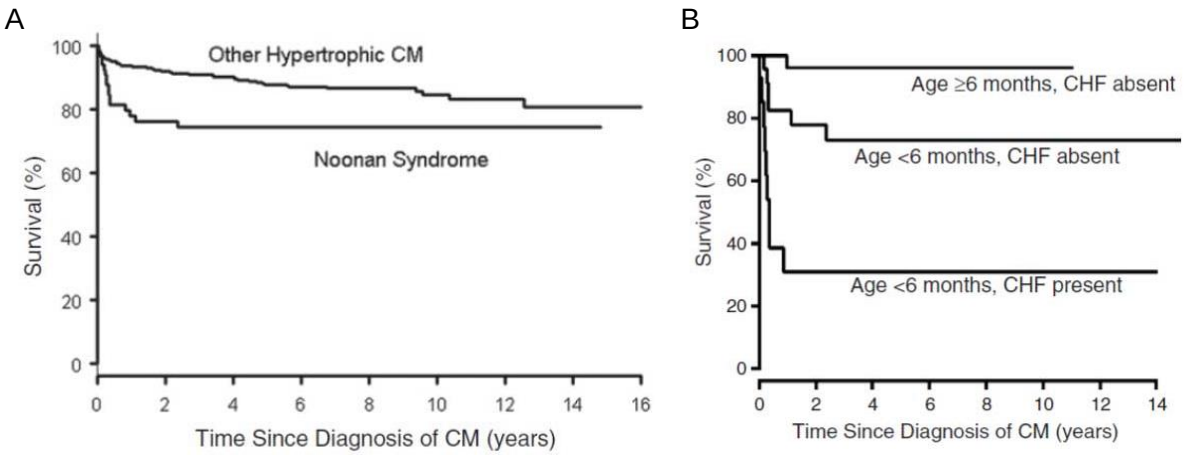

Figure 1: Survival rates of Noonan syndrome patients in early life

A, Patients diagnosed with pediatric HCM but not NS have a slow and steady mortality rate, while NS patients with HCM show a rapid drop of survival in early infancy. NS patients: n=72; other Hypertrophic CM patients: n=792. **B**, Survival rates from NS patients are mainly impaired by the presence of CHF in early life. Age ≥6 months, CHF absent: n= 33. Age <6 months, CHF absent: n=23 Age <6 months, CHF present: n=15. NS, Noonan syndrome; CM, cardiomyopathy; CHF, congestive heart failure. Reprinted with permission of "*American Heart Journal*" (Wilkinson et al. 2012).

2.1.2 RAS-MAPK signaling and Noonan syndrome

NS belongs to the class of RASopathies. The common underlying mechanism of RASopathies are mutations in genes that regulate the RAS–mitogen-activated protein kinase (RAS-MAPK) signaling pathway. The vast majority of mutations result in enhanced pathway activation (Rauen 2013), either through loss-of-function mutations in genes that negatively regulate RAS-MAPK activity, or through gain-of-function mutations that directly lead to increased pathway activity (Aoki et al. 2015; Simanshu et al. 2017). The RAS-MAPK signaling cascade plays a central role in proliferation, differentiation and cell cycle progression (Yoon and Seger 2006). Further, disturbances within RAS-MAPK signaling are strongly connected to oncogenesis as 40% of all human cancers show altered RAS-MAPK pathway activity. This is mainly caused by mutations in RAS and its downstream target BRAF (Bos 1989; Santarpia et al. 2012). Abnormal RAS-MAPK signaling during embryogenesis causes an impaired neural crest cell development and leads to malformations in the cardiac, craniofacial and central nervous system (Hamada et al. 2020). NS as the most frequent RASopathy (Tidyman and Rauen 2016) displays exactly these symptoms and is mostly described as an autosomal dominant disorder. Heterozygous mutations in *PTPN11* (Tartaglia et al. 2001), *SOS1* (Tartaglia et al. 2007), *RAF1* (Pandit et al. 2007), *KRAS* (Schubbert et al. 2006), *NRAS* (Cirstea et al. 2010), *RRAS* (Flex et

al. 2014), *SHOC2* (Cordeddu et al. 2009), *PPP1CB* (Gripp et al. 2016) and *CBL* (Martinelli et al. 2010) account for >80% of all NS cases. The first cases of autosomal recessive forms of NS were already reported in 2000, but the underlying genetic background was not elucidated (van der Burgt and Brunner 2000). More recently, whole-exome sequencing of NS patients allowed the discovery of novel NS causing genes, such as *RIT1* (Aoki et al. 2013; Chen et al. 2014) and *LZTR1* (Yamamoto et al. 2015), that are not a direct part of the signaling cascade.

The RAS-MAPK pathway is activated by the binding of growth factors to receptor tyrosine kinases (RTK) which leads to autophosphorylation of the receptor. Activated domains of the receptor act as docking sites for intracellular proteins such as adaptor protein growth factor receptor-bound protein 2 (GRB2), Signaling and transforming protein containing Src homology 2 and 3 (SH2 and SH3) domains (SHC) and Src homology region 2-domain phosphatase 2 (SHP-2). These proteins recruit son-of-sevenless (SOS), which acts as guanosine nucleotide exchange factor (GEFs), causing the switch from inactive RAS-GDP to the active RAS-GTP form. Activated RAS directly causes the subsequent activation of rapidly activated fibrosarcoma (RAF) proteins, which further phosphorylates mitogen-activated protein kinase kinases 1/2 (MEK1/2). Active MEKs activate the extracellular signal-regulated kinases 1/2 (ERK1/2) which are the final effectors of this pathway and exert their function on cytosolic and nuclear substrates (Figure 2), including transcription factors that control differentiation and proliferation processes. (Jorge et al. 2009; Tidyman and Rauen 2016). Activity of GTP bound RAS is terminated by the binding of GTPase-activating proteins (GAP), which causes a hydrolyzation of GTP into GDP (Maegley et al. 1996). Oncogenic variants of RAS that are refractory to GAP activity are prenatal lethal, therefore restricting germline transmission (Tuveson et al. 2004; Chen et al. 2009).

Within this pathway, RAS proteins are small guanosine nucleotide-bound GTPases that comprise a critical signaling hub within the cell. Different RAS proteins are described, including the closely related isoforms HRAS, KRAS and NRAS which share very similar, almost ubiquitous expression profiles and only differ in the so-called hypervariable region of the C-terminal region (Karnoub and Weinberg 2008; Abe et al. 2020). Compared to these three isoforms, the sequence of MRAS is less conserved and is mainly expressed in muscle tissues, especially in the heart (according to online databases; http://www.proteinatlas.org). Based on their frequent co-expression in a vast cellular context and their high level of homology combined with the fact that all RAS forms share common roles in the same pathways with identical downstream targets and upstream activators it was assumed that they facilitate mostly redundant functions (Castellano and Santos 2011). However, it is not fully understood

whether these different RAS proteins fulfill different or overlapping functions in physiological and pathological processes.

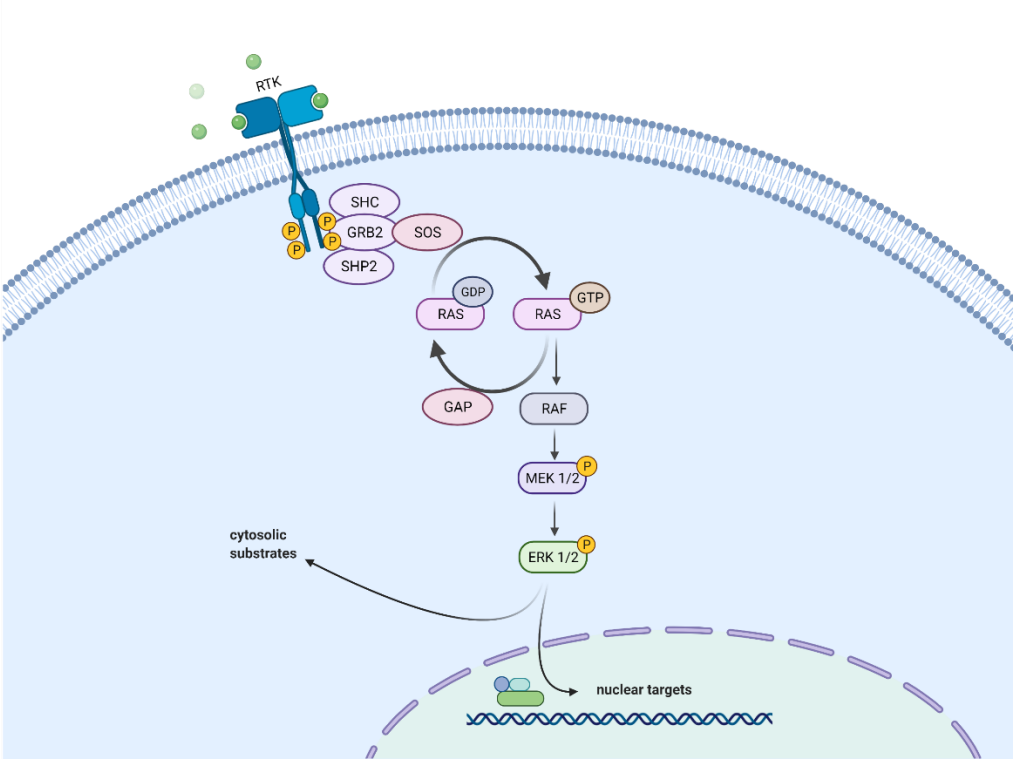

Figure 2: The RAS-MAPK signaling cascade

Binding of growth factors to the RTK starts the cascade of signals. Phosphorylated RTK binds GBR2, SHC and SHP2 which recruit SOS. This causes the switch from inactive RAS-GDP to RAS-GTP. Activated RAS further transmit the signal through RAF, MEK1/2 and ERK 1/2 which initiate transcription of nuclear targets and activation of cytosolic substrates GAPs which catalyze the hydrolyzation from GTP to GDP to terminate RAS activity. RAF, rapidly activated fibrosarcoma. MEK1/2, mitogen-activated protein kinase kinase 1/2. ERK1/2, extracellular signal-regulated kinase 1/2. GAP, GTPase activating protein. Image created with Biorender.

2.1.3 Compound heterozygous loss of *LZTR1* causes NS

In a previous study, our group and associates identified a nonconsanguineous family with two male children who were diagnosed with an early-onset HCM. Both parents were unaffected as evident in the family pedigree (Figure 3A). Echocardiography revealed the severity of the HCM which included outflow obstructions. For the younger brother, HCM was even diagnosed prenatally (Figure 3B). By the ages of 3,5 years and 6 months, both children underwent cardiac surgery. Specifically, a septum myectomy was performed which included the implantation of a cardioverter-defibrillator to prevent sudden cardiac death. Besides the cardiac abnormality,

both brothers showed common symptoms of NS including the typical facial characteristics such as ptosis, low set ears and a short neck (Figure 3C). Further, general developmental delay and short stature was diagnosed. Screening of typical NS-associated genes by next generation sequencing did not result in detection of a causative mutation. Whole-exome sequencing was subsequently performed by the group of Prof. Dr. Bernd Wollnik and revealed a compound heterozygous variant of Leucine zipper like transcription regulator 1 (*LZTR1*) in both children (Figure 3D-E). Upon discovery of this mutation, the function of *LZTR1* was completely unknown. The mutation of the first allele in exon 1 (c.27dupG) causes a frameshift which leads to early termination of protein synthesis (p.Q10Afs*24). On the second allele, an additional mutation of *LZTR1* was detected after further analysis in intron 16 of both brothers (c.1943-256C>T). This variant introduces an additional donor splice site that results in the inclusion of a cryptic exon. This 117 bps long abnormal exon carries a stop codon that leads to premature termination of protein synthesis, resulting in a truncated protein (p.T648fs*36) (Figure 3G). These findings were confirmed in the *LZTR1* transcripts of the parents, who carry one affected allele each. The *LZTR1* mutation in exon 1 (c.27dupG) was inherited by the mother, while the intronic variant in intron 16 (c.1943-256C>T) is paternal. Taken together, the compound heterozygous mutations in both children led to synthesis of a truncated, non-functional LZTR1 protein which causes NS (Hanses et al. 2020).

Skin biopsies of both children and parents were obtained and reprogrammed into induced pluripotent stem cells (iPSCs). Reverse transcription polymerase chain reaction (RT-PCR) conducted on these cell lines revealed the predicted cryptic exon that appeared as an additional 117 bps larger band which was only present in samples from both children and the father but not in the mother and unrelated WT samples (Figure 3F).

Since both parents are healthy, this *LZTR1* variant displays a rare autosomal recessive form of NS, which is transmitted in an autosomal dominant manner in most cases. The paternal mutation in intron 16 of *LZTR1* was also described in 4 additional unrelated families (Johnston et al. 2018), where it was also shown to cause NS in an autosomal recessive form.

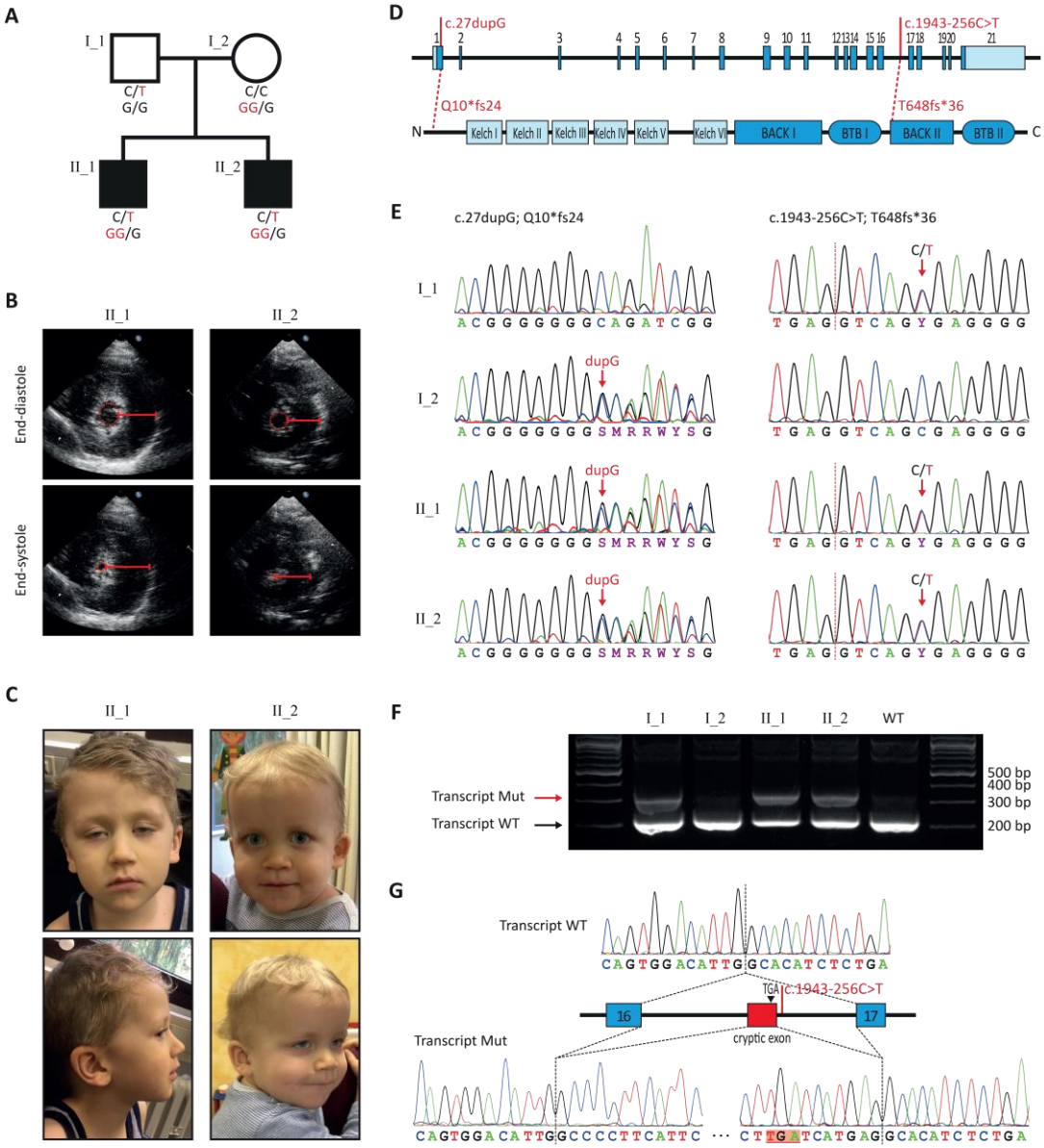

Figure 3: A rare form of autosomal recessive NS caused by biallelic *LZTR1* loss

A, Family pedigree showing the healthy parents (father I_1 and mother I_2) and the affected children (II_1 and II_2). **B,** Echocardiogram of both children at the age of 3.5 years (II_1) and 6 months (II_2), showing the hypertrophic left ventricle during systole and diastole (red lines) prior to septum myectomy. Shown in parasternal short-axis. **C**, Facial features of the affected brothers at 5 years (II_1) and 2 years (II_2) of age. Both show NS-associated facial dysmorphisms such as ptosis, low set ears and hypertelorism. **D**, Schematic depiction of *LZTR1* on genomic (above) and on protein level (below). Positions of the maternal (c.27.dupG) and the paternal mutation (c.1943-256C>T) are highlighted in red. **E**, Sanger sequencing results from both parents and children showing the *LZTR1* variants in exon 1 and intron 16. **F**, RT-PCR reveals the presence of the cryptic exon between exon 16 and 17. Note that this additional band of 117 bp is not present in the mother and unrelated controls. **G**, Sanger sequencing of the paternal allele from the affected region between exon 16-17 confirmed the insertion of 117 bps which introduces a stop codon that leads to termination of protein synthesis. Reprinted with the permission of "*Circulation*" (Hanses et al. 2020).

2.2 Leucine-zipper-like transcriptional regulator 1 (*LZTR1*)

LZTR1 is a ubiquitously expressed gene and encodes a protein of the Broad-Complex, Tramtrack, and Bric-a-Brac (BTB)-Kelch superfamily (Nacak et al. 2006), which are generally involved in fundamental cellular processes such as migration, cell morphology and gene regulation (Adams et al. 2000). In particular, BTB-Kelch proteins often act as substrate adaptors for Cullin3 (CUL3)-based E3 ubiquitin ligases (Furukawa et al. 2003; Geyer et al. 2003). BTB-Kelch proteins typically consist of an N-terminal BTB domain followed by the Kelch domain. In contrast to that, LZTR1 carries an N-terminal Kelch domain followed by two BTB domains which is a unique structure compared to other BTB-Kelch proteins (Figure 4A-B). The function of LZTR1 was first predicted as a transcriptional regulator based on weak homology to members of the basic leucine zipper-like family which could not be confirmed in follow up studies. Before the exact function of the gene and its link to NS was discovered, *LZTR1* was described as a tumor suppressor gene and mutations were associated with other diseases, such as schwannomatosis (Piotrowski et al. 2014) and glioblastoma (Frattini et al. 2013). Increasing evidence that *LZTR1* mutations are involved in NS was delivered by whole-exome sequencing of NS patients that had no mutations in genes commonly linked to the disease. These first cases implied that variants of *LZTR1* are responsible for causing less than 3% of all NS cases in an autosomal dominant fashion exclusively (Yamamoto et al. 2015). Autosomal dominant mutations can occur *de novo* or be inherited by affected parents. Later, the existence of rare forms of NS that are inherited in an autosomal recessive manner were uncovered. These family studies showed clinically unaffected parents with heterozygous loss-of-function mutations in *LZTR1* while their children carried both affected alleles and displayed typical NS symptoms including HCM (Johnston et al. 2018). Due to the strong connection between NS and over-activating mutations in genes coding for proteins that are part of the RAS-MAPK signaling pathway, a related role for LZTR1 was predicted but not revealed until 2018. It was then proposed in several publications that LZTR1 mediates ubiquitination and subsequent degradation of RAS proteins (Steklov et al. 2018; Bigenzahn et al. 2018; Castel et al. 2019). It was shown that RAS binds to the Kelch domain of dimerized LZTR1 proteins while the CUL3 binds to the first BTB I/BACK I domain and weakly with the Kelch domain of LZTR1 (Steklov et al. 2018; Abe et al. 2020)(Figure 4C). This interplay facilitates the ubiquitination and proteasomal degradation of RAS. Hence, loss-of-function mutations in *LZTR1* lead to accumulation of RAS and hyperactivation of the RAS-MAPK pathway. This is concordant with mutations of other genes which lead to elevated RAS-MAPK signaling that result in NS or related RASopathies. Although the consensus is now that LZTR1 regulates the activity of the

RAS-MAPK signaling pathway, there are controversies in the literature regarding which RAS isoforms are targeted. While Castel et al. showed the interaction of LZTR1 with RIT1 and MRAS but no other RAS isoforms (Castel et al. 2019), other results suggested that LZTR1 mediates ubiquitination and degradation of several RAS isoforms, including MRAS, HRAS, NRAS and KRAS (Abe et al. 2020). With these findings, *LZTR1* came into the focus of research during the last 2 years regarding its role as a key player in RAS-MAPK signaling and development of NS. Recent studies now further expand the pathogenic spectrum of *LZTR1*. Sewduth et al. reported that *LZTR1* dysfunctions cause bleeding complications in NS patients and might be involved in regulation of vesicular trafficking (Sewduth et al. 2020). However, most research was conducted in HEK293T or HeLa cell systems and studies in HCM related, physiological properties of patient specific *LZTR1*-deficient iPSC-CMs are still rare and underlying mechanism are not completely understood.

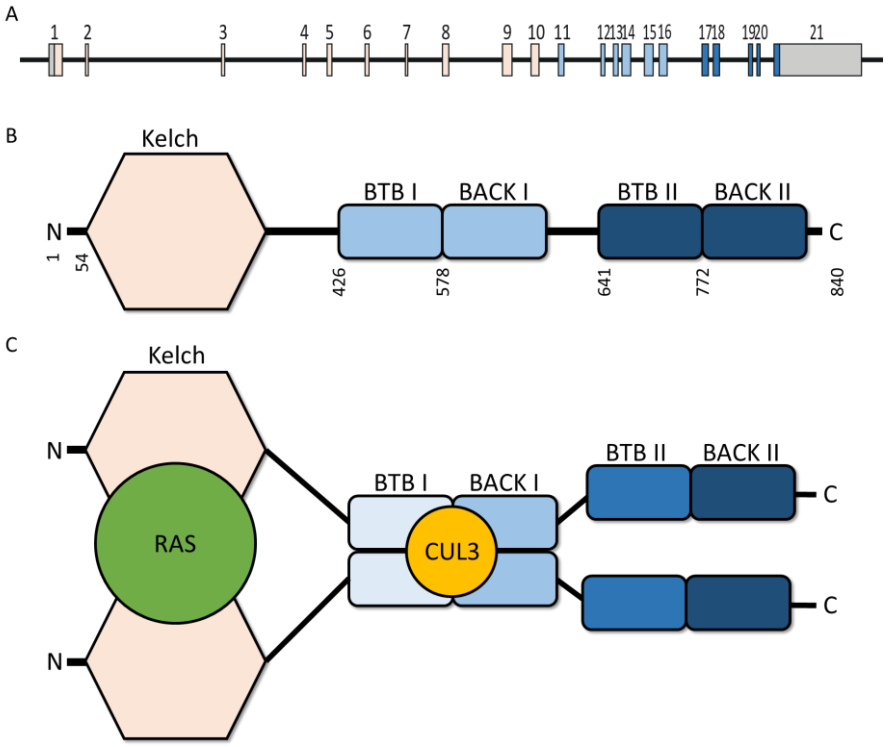

Figure 4: Genetic and protein features of LZTR1

A, Visualization of *LZTR1* consisting of 21 exons. Colors indicate which exon contributes to which domain. **B,** Schematic protein domains and structure of LZTR1 with the N-terminal kelch domain and the C-terminal BACK and BTB domains. **C,** Predicted dimerization of LZTR1 with the N-terminal Kelch domain binding to RAS and the dimerized BTB I-BACK I domains binding CUL3. The C-terminal BTB II and BACK II domains are presumably required for stabilization of the dimerized complex.

2.3 Induced pluripotent stem cells in disease modeling

In 2006, Takahashi and Yamanaka successfully demonstrated the first reprogramming of murine fibroblasts into iPSCs (Takahashi and Yamanaka 2006), marking the beginning of a new aera in disease modeling. Compared to the work with embryonic stem cells (ESCs), usage and production of iPSCs are not under ethical debate. The generation of iPSCs was achieved by retroviral transduction of the four transcription factors octamer-binding transcription factor (OCT3/4), sex determining region Y-box 2 (SOX2), C-MYC, and Krüppel-like factor 4 (KLF4) in murine fibroblasts. These cells possessed the ability to self-renew and to differentiate into cells from all three germ layers and showed expression of characteristic pluripotency genes (Takahashi and Yamanaka 2006). For this revolutionary finding, Yamanaka was awarded the Nobel prize in Physiology or Medicine in 2012. The procedure was later adjusted to facilitate the reprograming of human fibroblasts into iPSCs (Takahashi et al. 2007). Since then, reprograming methods have been constantly refined regarding the delivery of the so-called “Yamanaka factors” (Malik and Rao 2013) and improved for their use in other cell types which can be gathered in a less invasive manner, such as cells from peripheral blood (Staerk et al. 2010) or urine (Zhou et al. 2011).

Efficient protocols for directed differentiation of iPSCs into various cell types, such as iPSC derived cardiomyocytes (iPSC-CM),are readily available, (Kleinsorge and Cyganek 2020). Administration of small molecules that temporarily modulate the activity of the Wnt pathway has been shown to drive efficient differentiation of iPSCs into ventricular iPSC-CMs (Gonzalez et al. 2011; Lian et al. 2013). Inhibition of glycogen synthase kinase 3 (GSK3) with CHIR99021 enhances Wnt signaling activity and induces differentiation of iPSCs into early mesoderm cells (Lam et al. 2014). Subsequent treatment with inhibitor of Wnt production 2 (IWP-2), a selective inhibitor of Protein-serine O-palmitoleoyltransferase porcupine (PORCN), reduces Wnt activity and further directs the differentiation into iPSC-CMs. A high purity of iPSC-CMs is required to generate meaningful data from downstream applications and experiments. The ability of iPSC-CMs to process lactate can be used for metabolic selection to increase the purity of these cells. This process is based on glucose-depleted medium which is supplemented with lactate (Tohyama et al. 2013).

iPSC-CMs have been used for disease modeling extensively within the last years. They hold the potential to model cardiac specific diseases and recapitulate the phenotype of the patients. In-depth *in vitro* analysis of patient specific iPSC-CMs are conducted to uncover molecular mechanisms and translate the discoveries into novel therapeutic strategies that pave the way

for personalized medicine (Figure 5). The potential of this cell system to successfully model cardiac diseases was shown for long-QT syndrome (Moretti et al. 2010), catecholaminergic polymorphic ventricular tachycardia (Itzhaki et al. 2012; Kujala et al. 2012), and cardiomyopathies such as HCM (Lan et al. 2013) or dilated cardiomyopathy (Sun et al. 2012). For NS, 4 patient specific iPSC-CM models have been reported so far, one generated from our group. Interestingly, they are based on mutations in different genes, *MRAS* (Higgins et al. 2019), *RAF1* (Sakai et al. 2018; Jaffré et al. 2019) and *LZTR1* (Hanses et al. 2020). The ongoing development in recent years established iPSCs as a powerful tool for disease modeling, especially when combined with techniques for genome editing.

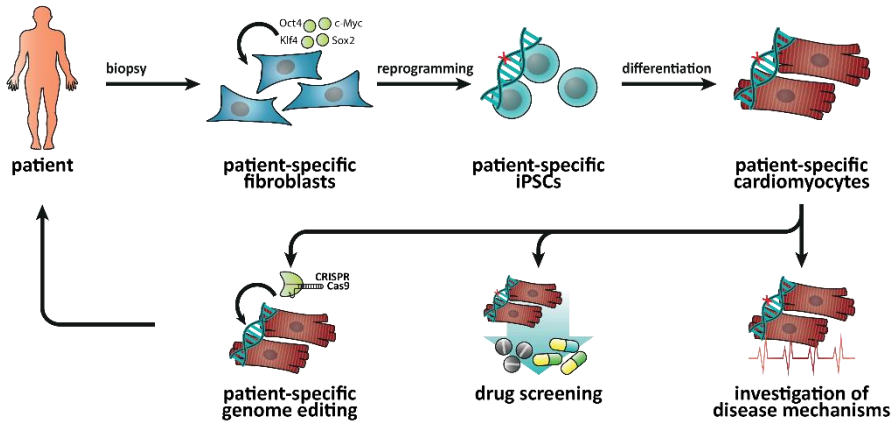

Figure 5: Generation and possible downstream applications for iPSC-CMs

Applications of iPSCs and schematic workflow for patient specific iPSC-CMs for downstream analysis. Cells obtained from patients are reprogrammed into iPSCs which are subsequently differentiated into functional iPSC-CMs which recapitulate the patient's phenotype. The patient specific cells are investigated in functional analyses, employed in drug screening for personalized medicine or evaluated for custom tailored genome editing. Figure adapted from Lukas Cyganek, unpublished.

2.4 CRISPR/Cas9 as a tool for genome editing in iPSCs

Modern strategies for reprogramming somatic cells to generate iPSCs and the possibility to efficiently differentiate these cells into various cell types set a new standard in the way human diseases can be modeled. This enabled a rapid growth of knowledge about pathophysiological mechanisms underlying cardiac diseases and quickly raised the need for new technologies to edit the genetic background of patient specific iPSCs, in order to introduce either pathophysiological relevant mutations in WT cell lines or to correct mutations in patient specific

iPSCs. Within the last years, CRISPR/Cas9 has emerged as the tool of choice for genome editing in various cell types and organisms with high efficiency and accuracy. The discovery of clustered regularly interspaced short palindromic repeats (CRISPR) (Mojica et al. 1993) and the clarification of the function of CRISPR associated 9 enzyme (Cas9) together with the protospacer adjacent motif (PAM) (Bolotin et al. 2005), were essential findings for the development of the revolutionary genome editing strategy. The crucial work that marked the beginning of CRISPR/Cas9 as a biotechnology tool was published by two independent groups in 2012 and was awarded with the Nobel Prize in Chemistry in 2020. It was shown that Cas9 enzymes can be utilized to target any desired DNA sequences in bacteria to introduce double strand breaks (Gasiunas et al. 2012; Jinek et al. 2012). These studies were quickly adapted for the use in eukaryotic cells (Le Cong et al. 2013; Mali et al. 2013) and later optimized for iPSCs (Hockemeyer and Jaenisch 2016).

CRISPR/Cas9 mediated double strand breaks are subjected to the cellular DNA repair mechanisms non-homologous end joining (NHEJ) (Moore and Haber 1996) or homology directed repair (HDR) to either introduce gene specific knock-outs (KOs) or knock-ins (KIs) of DNA fragments, making use of cell specific DNA repair mechanisms (Figure 6). NHEJ facilitates ligation of DNA breaks. As an error-prone mechanism, small insertion or deletions (indels) are introduced randomly, often leading to loss-of-function gene variants by frameshifts. HDR requires the presence of a DNA fragment with homology to the sequences flanking the double strand break region, which is used as a template for repair, thereby inserting the pre-designed sequences that can range from single nucleotide polymorphisms to several hundred base pairs long protein tags. With CRISPR/Cas9 it is possible to introduce disease causing mutations into wild type cell lines or correct mutations in patient specific iPSC lines. This enables the generation of meaningful, isogenic control cell lines that only differ from the parent cell line in the edited site and renders the possibility to focus only on the pathologies caused by a specific mutation, which allow valid conclusions to be drawn from comparisons. CRISPR/Cas9 has been used extensively in iPSCs in the last years for successful disease modeling for the investigation of cellular and molecular mechanisms underlying genetically inherited diseases in several fields, including metabolic, immunological, neurodegenerative as well as cardiac diseases (Ben Jehuda et al. 2018). In particular, the application of CRISPR/Cas9 in iPSC-CMs led to the generation of isogenic disease models for several forms of cardiomyopathies, such as dilated cardiomyopathy (McDermott-Roe et al. 2019), Barth syndrome (Wang et al. 2014), Long QT syndrome (Garg et al. 2018), Brugada syndrome (La Roche et al. 2019), and left ventricular non compaction (Kodo et al. 2016). Recently,

CRISPR/Cas9 based iPSC-CM models were shown to recapitulate the phenotype of NS (Higgins et al. 2019; Jaffré et al. 2019; Hanses et al. 2020).

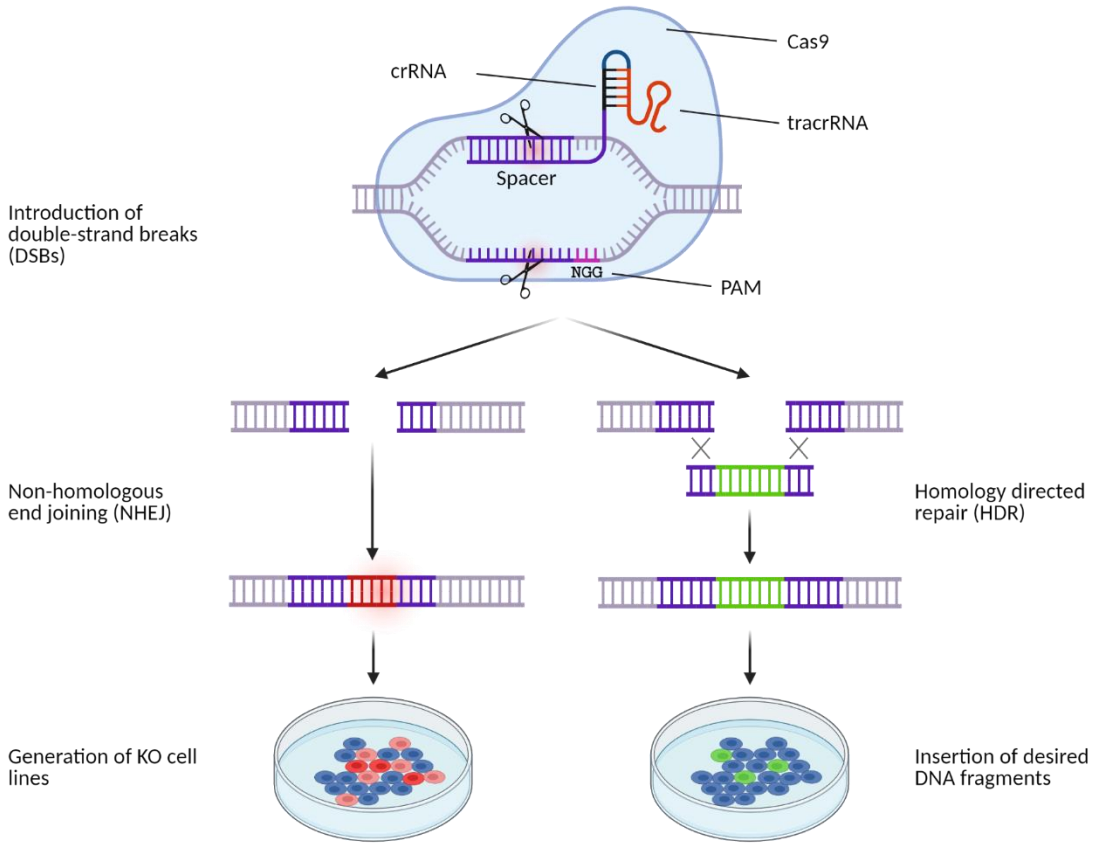

Figure 6: CRISPR/Cas9 overview

CRISPR/Cas9 mediated double strand breaks are utilized to either generate stable gene specific KO cell lines by introducing frameshifts or KIs of pre-designed DNA sequences. Image created with Biorender.

2.5 Aims of the study

When I started my Ph.D. project in 2017, *LZTR1* was discovered as a new NS causing gene. Although it was shown that mutations in this gene can cause NS in an autosomal dominant and autosomal recessive way, the role of this protein was completely uncharacterized, and the underlying molecular mechanisms remained incomprehensive. NS is the most prevalent RASopathy, and diseases of this class typically show an upregulation of RAS-MAPK signaling. Therefore, we suspected a role of *LZTR1* in this pathway. Therefore, my aim was to elucidate the functional role of LZTR1, detect possible interaction partners of LZTR1 and identify its intracellular localization using CRISPR/Cas9 based genome edited iPSC-CMs. As NS symptoms often include a severe form of HCM, the use of iPSC-CMs could help to answer questions that cannot be solved by using other cell systems or murine models.

Specific aims are summarized below:

- *CRISPR/Cas9 based tagging of endogenous LZTR1*
  The subcellular localization of LZTR1 was controversial in previous reports and was never investigated in cardiac cells. Therefore, I aim to use CRISPR/Cas9 to generate an iPSC line with stable expression of tagged *LZTR1* to identify its intracellular localization in iPSC-CMs.
- *Analyze the effects of LZTR1 overexpression in HEK293T cells*
  Full-length and truncated *LZTR1*, mimicking the paternal allele will be transiently overexpressed in HEK293T cells together with different RAS isoforms and CUL3 to analyze possible degradative effects via western blots.
- *Generation of homo- and heterozygous LZTR1-KO iPSC lines*
  To investigate the effects of *LZTR1* loss, I will generate four different *LZTR1* +/- and -/- iPSC lines. Exon 1 and exon 17 will be targeted using CRISPR/Cas9 to mimic the maternal and paternal mutations of the familial autosomal recessive NS case. The underlying WT cell line will serve as an isogenic control.
- *Investigate if LZTR1 loss causes disturbances of RAS-MAPK signaling*
  NS can be caused by mutations in several genes, all resulting in enhanced RAS-MAPK activity. *LZTR1* has not previously been described as part of this signaling cascade. To elucidate whether this protein interferes with RAS-MAPK in alternative ways, pathway activity will be analyzed in CRISPR/Cas9 based *LZTR1*-deficient iPSC-CMs.
- *Functional analyses of LZTR1-deficient iPSC-CMs*

The generated *LZTR1*-deficient iPSCs will be differentiated into iPSC-CMs for subsequent functional analysis to assess possible disturbances of electrophysiological parameters or hypertrophic cell sizes.

3 Materials and Methods

3.1 Cell lines

Table 1: Wild type cell lines

Name	hPSCreg ID	origin	Reprogramming system	publication
isWT1.14 (WT1)	UMGi014-C clone 14	Dermal fibroblast	CytoTune™-iPS Sendai Reprogramming Kit, feeder-free culture conditions	(Rössler et al. 2021)
ipWT1.3 (WT2)	UMGi014-B clone 3	Dermal fibroblast	4-in-1 CoMiP Reprogramming plasmid, feeder-free culture conditions	(El-Battrawy et al. 2018)
HEK293T	-	human embryonic kidney	-	(DuBridge et al. 1987)

Table 2: CRISPR/Cas9 based genome edited cell lines

Name	hPSCreg ID	Parent cell line	Target	Genome editing type	details
LZTR1-Exon 1 -/-	UMGi014-C-15 clone 3	isWT1.14 (WT1)	*LZTR1*, Exon 1	Compound heterozygous KO	c.135 dupT/A
LZTR1-Exon 1 +/-	UMGi014-C-15 clone 41	isWT1.14 (WT1)	*LZTR1*, Exon 1	Heterozygous KO	c.135 dupT
LZTR1-Exon 17 +/-	UMGi014-C-16 clone 1	isWT1.14 (WT1)	*LZTR1*, Exon 17	Heterozygous KO	c.13493 -5bp
LZTR1-Exon 17 -/-	UMGi014-C-16 clone 7	isWT1.14	*LZTR1*, Exon 17	Compound heterozygous KO	c.13493 -5bp c.13494 -5bp
LZTR1-Exon 1 -/- B	UMGi014-B-1 clone 1	ipWT1.3 (WT2)	*LZTR1*, Exon 1	Compound heterozygous KO	c.123 -13bp c.133 -154bp

LZTR1-Exon 1 -/- C	UMGi014-B-1 clone 38	ipWT1.3 (WT2)	*LZTR1*, Exon 1	Compound heterozygous KO	c.133 -2bp c.127 -8bp
LZTR1-V5 C-term	UMGi014-B-2 clone 19	ipWT1.3	*LZTR1*, Exon 21	Heterozygous KI	+42 bp V5 sequence at C-terminus
LZTR1-V5 N-term	UMGi014-C-1 clone 6	isWT1.14	*LZTR1*, Exon 1	Heterozygous KI	+42 bp V5 sequence at N-terminus

3.2 Cell culture media and solutions

Table 3: Media, supplements, and solutions for cell culture

Product	Manufacturer	Catalogue number
B-27 Supplement (50x)	Thermo Fisher Scientific	17504044
CHIR99021	Millipore	361571
Dimethyl sulfoxide (DMSO)	Sigma Aldrich	D2650
DMEM, high glucose, no glutamine	Thermo Fisher Scientific	11960044
Dulbecco's phosphate-buffered saline (DPBS)	Thermo Fisher Scientific	14190094
Fetal Bovine Serum (FBS)	Thermo Fisher Scientific	10270106
HEPES solution	Sigma Aldrich	H0887
Human recombinant Albumin	Sigma Aldrich	A9731
Wnt Antagonist II, IWP-2	Millipore	681671
L-ascorbic acid 2-phosphate	Sigma Aldrich	A8960
L-Glutamine (200 mM)	Thermo Fisher Scientific	25030024
Matrigel	Corning	7611631
MEM Non-Essential Amino Acids Solution (NEAA)	Thermo Fisher Scientific	11140035
Opti-MEM I Reduced Serum Medium	Thermo Fisher Scientific	31985062
Penicillin-Streptomycin solution	Merck	P4333

RPMI 1640 Medium, GlutaMAX Supplement, HEPES	Thermo Fisher Scientific	72400021
RPMI 1640 Medium, no glucose	Thermo Fisher Scientific	11879020
Sodium DL-lactate solution	Sigma Aldrich	L4263
StemFlex Medium	Thermo Fisher Scientific	A3349401
StemMACS iPS-Brew XF	Miltenyi	
Thiazovivin (TZV)	Sigma Aldrich	420220-M
Trypsin-EDTA (0.25%)	Thermo Fisher Scientific	25200056
Versene solution	Thermo Fisher Scientific	15040066

Table 4: Human cell culture medium and solution components

Medium / solution	Components
Cardio Cryopreservation medium	90% FBS 10% DMSO 2 µM TZV
Cardio Culture medium	500 ml RPMI 1640 Medium, GlutaMAX Supplement, HEPES 10 ml B27 supplement
Cardio Differentiation medium	500 ml RPMI 1640 Medium, GlutaMAX Supplement, HEPES 250 mg human recombinant albumin 100 mg L-ascorbic acid 2-phosohate
Cardio Digestion medium	80 ml Cardio Culture Medium 20 ml FBS (heat-inactivated) 1000 µl Penicillin – Streptomycin 100 µl TZV
Cardio Selection medium	500 ml RPMI 1640 without Glucose and HEPES 2 ml Lactate / HEPES (1M Stock solution) 250 mg human albumin 100 mg L-Ascorbic Acid 2-Phosphate
CHIR (4 mM)	5 mg CHIR99021 dissolved in 894 µl DMSO

HEK medium	450 ml DMEM 50 ml FBS (heat-inactivated) 5 ml NEAA 5 ml L-Glutamin
IWP2 (5 mM)	10 mg dissolved in 4,28 mg DMSO and incubated for 10 min at 37 °C
Lactate / HEPES (1 M)	3 ml sodium DL-lactate dissolved in 18ml 1M HEPES solution
Matrigel (1:60 dilution)	500 µl Matrigel 29,5 µl PBS
TZV (2 mM)	10 mg TZV dissolved in 16,05 ml DMSO

3.3 Chemicals

Table 5: Chemicals

Product	Manufacturer	Catalogue number
10x TGS Running Buffer	Bio-Rad	161-0732
4-(2-hydroxyethyl)-1-piperazineethanesulfonic acid (HEPES)	Roth	HN77.1
4x Laemmli Sample Buffer	Bio-Rad	1610747
Accutase	Thermo Fisher Scientific	A1110501
Alt-R S.p. HiFi Cas9 Nuclease 3NLS	IDT DNA Technologies	1081061
Alt-R CRISPR-Cas9 tracrRNA	IDT DNA Technologies	1072534
Alt-R® HDR Enhancer	IDT DNA Technologies	1081073
Ampicillin	Roth	1025642
Beta-Mercaptoethanol	Promega	Z559A
Boric Acid	Th. Geyer	15663
Bovine Serum Albumin (BSA)	Sigma Aldrich	A9647
Calcium Chloride solution ($CaCl_2$)	Sigma Aldrich	21115
DNA Gel Loading Dye (6X)	Thermo Fisher Scientific	R0611

DNase I	Promega	Z358A
dNTP Mix	Bioline	BIO-39029
Ethanol	Merck	1009831000
Ethylenediaminetetraacetic acid (EDTA)	Roth	8040.3
Fluo-4, AM	Thermo Fisher Scientific	F14201
Fluoromount-G	Thermo Fisher Scientific	00-4958-02
Gene Ruler 100bp plus DNA Ladder	Thermo Fisher Scientific	SM0322
Glucose	Roth	HN06.2
Glycin	Roth	3908.3
GlycoBlue	Thermo Fisher Scientific	AM9515
GoTaq DNA Polymerase	Promega	M3001
Hydrochloric acid (HCl)	Roth	K025.1
Isoprenaline	Sigma Aldrich	15627
Isopropanol	Th. Geyer	1.09634.1000
Kanamycin	Roth	T832.1
Magnesium chloride ($MgCl_2$)	Roth	KK36.2
MG-132	InvivoGen	tlrl-mg132
Midori Green	Biozym	617004
Milk powder	Roth	T145.2
Oligo(dT)20 Primer	Thermo Fisher Scientific	18418020
peqGold Universal Agarose	VWR	35-1020
Phusion High-Fidelity DNA Polymerase	Thermo Fisher Scientific	F530S
Protease and Phosphatase Inhibitor Mini Tablets	Thermo Fisher Scientific	A32961
Pluronic F-127	Thermo Fisher Scientific	P3000MP
Potassium Chloride (KCl)	Roth	HN02.1
PageRuler Plus Prestained Protein Ladder	Thermo Fisher Scientific	26619
Pierce IP Lysis Buffer	Thermo Fisher Scientific	87787
Proteinase K	VWR	732-3276

RIPA Lysis and Extraction Buffer	Thermo Fisher Scientific	89900
Roti-Histofix	Roth	P087.4
ROX reference dye	Thermo Fisher Scientific	12223012
iQ™ SYBR® Green Supermix	Bio-Rad	1708882
Sodium Chloride (NaCl)	Roth	3957.1
Sodium hydroxide solution (NaOH)	Roth	K021.1
Superscript IV reverse transcriptase	Thermo Fisher Scientific	18090010
Tris(hydroxymethyl)-aminomethane (TRIS)	Roth	5429.3
Triton X-100	Roth	3051.4
TRIzol Reagent	Thermo Fisher Scientific	15596-026
TrypLE™ Select Enzyme (10X)	Thermo Fisher Scientific	A1217701
Trypsin (2,5%)	Thermo Fisher Scientific	15090046
Tween-20	Roth	9127.1
Verapamil-hydrochlorid	Sigma-Aldrich	V4629-1G

3.4 Buffers and solutions

Table 6: Buffers and solutions

Buffer/solution	Ingredients
Gel electrophoresis	
TBE (5x Stock)	54 g Tris 27,5 g boric acid 3,72 g EDTA Fill to 1 l with ddH_2O
Immunofluorescence	
Blocking buffer	1% BSA in PBS
Staining buffer	1% BSA in PBS
Cell permeabilization buffer	0,1% Triton-X 100 in 1% BSA in PBS

Western Blot	
10x TBS	80 g NaCl 24 g Tris Fill to 1 l with ddH_2O Adjust to pH 7.6 (HCl)
1x TBS-T	900 ml ddH_2O 100 ml 10x TBS 1 ml Tween-20
1x Running buffer	100 mL 10 x TGS buffer 900 mL ddH_2O
Blocking buffer	5% milk or 5% BSA in 1x TBS-T
Pierce IP Lysis Buffer	10 ml Pierce IP Lysis Buffer 1 Pierce Protease and Phosphatase Inhibitor Mini Tablet
RIPA buffer	10 ml RIPA Lysis and Extraction buffer 1 Pierce Protease and Phosphatase Inhibitor Mini Tablet
Confocal calcium Imaging	
Tyrode's solution (10x stock)	140 mM NaCl 5,4 mM KCl 1 mM $MgCl_2$ 10 mM HEPES Dissolved in 100 ml ddH_2O, pH 7.4
Tyrode's solution (1x)	44,9 ml ddH_2O 5 ml 10x Tyrode's solution 90 mg Glucose 90 µl $CaCl_2$ pH 7.4
Fluo-4 AM stock solution	50 µg Fluo-4 AM 44 µl DMSO
Fluo-4 AM staining solution	4 µl Fluo-4 AM stock solution 1 µl Pluoronic 800 µl Tyrode's solution (1x)
Isoprenaline (1 mM stock)	25 g Isoprenaline dissolved in 1 ml ddH_2O and diluted 1:100 in ddH_2O

Verapamil (50 mM stock)	25 mg verapamil 1000 µl DMSO
RNA isolation	
RNA lysis buffer	10 ml RNA lysis buffer 200 µl β-Mercaptoethanol
DNase I	1 vial of lyophylized stock DNase 275 µl ddH_2O
DNase incubation mix	40 µl Yellow core buffer 5 µl 0,09 M MnCl2 5 µl DNase I

3.5 Kits

Table 7: Kits

Product	Manufacturer	Catalogue number
Lipofectamine 3000 Transfection Reagent	Thermo Fisher Scientific	L3000001
Lipofectamine Stem Transfection Reagent	Thermo Fisher Scientific	STEM00015
NucleoBond Xtra Midi Kit	Macherey Nagel	740410.50
P3 Primary Cell 4D-Nucleofector X	Lonza	V4XP-3024
Pierce BCA Protein Assay Kit	Thermo Fisher Scientific	23227
QIAamp DNA Mini Kit	Qiagen	51306
QIAquick Gel Extraction Kit	Qiagen	28706
SuperScript IV Reverse Transcriptase	Thermo Fisher Scientific	18090010
SuperSignal West Femto Maximum Sensitivity Substrate	Thermo Fisher Scientific	34094
SV Total RNA Isolation System	Promega	Z3105
Mini-PROTEAN TGX Stain-Free Gels	Bio-Rad	4568086

Trans-Blot Turbo RTA Mini Nitrocellulose Transfer Kit	Bio-Rad	1704270

3.6 Antibodies

Table 8: Primary antibodies

Antibody	Manufacturer	Catalogue number
Akt polyclonal rabbit IgG	Cell Signaling Technology	Cat# 9272, RRID:AB_329827
Phospho-Akt (Ser473) monoclonal rabbit IgG	Cell Signaling Technology	Cat# 4060, RRID:AB_2315049
α-actinin monoclonal mouse IgG1	Sigma-Aldrich	Cat# A7811, RRID:AB_476766
β-actin monoclonal mouse IgG2a	Sigma-Aldrich	Cat# A2228, RRID:AB_476697
Flag Tag monoclonal mouse IgG1 HRP conjugate	Sigma-Aldrich	Cat# A8592
Flag Tag monoclonal mouse IgG	Sigma-Aldrich	Cat# F1804
HA Tag monoclonal mouse IgG1	Thermo Fisher Scientific	Cat# 26183
HA Tag monoclonal mouse IgG1 HRP conjugate	Cell Signaling Technology	Cat# 2999
HA Tag monoclonal rabbit IgG	Thermo Fisher Scientific	Cat# MA5-27914
LAMP1 polyclonal rabbit IgG	Abcam	Cat# ab24170
LIN28 polyclonal goat IgG	R and D Systems	Cat# AF3757, RRID:AB_2234537
LZTR1 monoclonal mouse IgG1 *	Santa Cruz Biotechnology	Cat# sc-390166, RRID: -
LZTR1 polyclonal rabbit IgG *	Sigma-Aldrich	Cat# HPA071248, RRID:AB_2686372
LZTR1 polyclonal rabbit IgG *	Thermo Fisher Scientific	Cat# PA5-20902, RRID:AB_11153342
LZTR1 polyclonal rabbit IgG *	Synaptic Systems	Custom-made
LZTR1 polyclonal rabbit *	Custom made	Not published,

		Gift from Pau Castel
p44/p42 MAPK polyclonal rabbit IgG	Santa Cruz Biotechnology	Cat# sc-94, RRID:AB_2140110
PEX14 polyclonal rabbit IgG	Proteintech	Cat# 10594-1-AP
Phospho-p44/42 MAPK (Thr202/Tyr204) polyclonal rabbit IgG	Cell Signaling Technology	Cat# 9101, RRID:AB_331646
MLC2V polyclonal rabbit IgG	Proteintech	Cat# 10906-1-AP, RRID:AB_2147453
Myc Tag monoclonal mouse IgG2a	Cell Signaling Technology	Cat# 2276
NANOG polyclonal rabbit IgG	Thermo Fisher Scientific	Cat# PA1-097, RRID:AB_2539867
OCT3/4 polyclonal goat IgG	R and D Systems	Cat# AF1759, RRID:AB_354975
OCT3/4 conjugated Alexa Fluor 647 monoclonal mouse IgG1	BD Biosciences	Cat# 560329, RRID:AB_1645318
pan-RAS monoclonal mouse IgG2a	Merck Millipore	Cat# 05-516, RRID:AB_2121151
SOX2 monoclonal mouse IgG1	Thermo Fisher Scientific	Cat# MA1-014, RRID:AB_2536667
TRA-1-60 monoclonal mouse IgM	Abcam	Cat# ab16288, RRID:AB_778563
TRA-1-60 conjugated Alexa Fluor 488 monoclonal mouse IgM	BD Biosciences	Cat# 560173, RRID:AB_1645379
V5 Tag Monoclonal mouse igG2a	Thermo Fisher Scientific	Cat# R960-25
Vinculin monoclonal mouse IgG1	Sigma-Aldrich	Cat# V9131

*not functional in detecting endogenous LZTR1 protein in our cell model

Table 9: Secondary antibodies and dyes

Antibody	Origin	Dilution	Manufacturer	Catalogue number
Anti-rabbit HRP	Donkey	1:10000	Cytiva	NA934V
Anti-mouse HRP	Sheep	1:10000	Cytiva	NA931V
anti-mouse 555	Donkey	1:500	Abcam	ab150114
anti-rabbit 488	Donkey	1:500	Thermo Fisher Scientific	A11008
Hoechst33342	-	1:2000	Thermo Fisher Scientific	H3570

3.7 Primers

Table 10: Primers used for PCR

Gene (PCR)	Primer for / rev	Length
GAPDH	AGAGGCAGGGATGATGTTCT TCTGCTGATGCCCCCATGTT	258 bp
LZTR1_gDNA-Ex1	GGTAGGCTTGTCGGGAAGAG ATGAAGCCCACCGTACCG	377 bp
LZTR1-trunc-F1/R1	CAACATGGGCAGATATGCAG ACACAAAGCAATGACCCAC	724 bp
qLZTR1-HEK-F3/R3	GAGCCAACTCAAGGAGCACT CAATGTCCACTGGCTGGTCC	170 bp

3.8 Bacteria culture material and medium

Table 11: Bacteria culture material and medium

Product	Manufacturer	Catalogue number
LB-Agar (Lennox)	Roth	X965.1
LB-Medium (Luria/Miller)	Roth	X968.1

SOC Outgrow Medium	NEB	B9020S

3.9 Bacterial strains

Table 12: Bacterial strains

Strain	Manufacturer	Usage
NEB 10-beta competent E. coli	NEB	Plasmid amplification

3.10 Plasmids

Table 13: List of Plasmids

Plasmid	Features	Producer
pcDNA3-HA-LZTR1-WT	CMV promoter, HA-tag, full-length LZTR1, AMP resistance	Genewiz
pcDNA3-HA-LZTR1-mut	CMV promoter, HA-tag, truncated LZTR1, Ampicilin resistance	Genewiz
pcDNA3-myc-CUL3	CMV promoter, myc-tag, full-length CUL3, Ampicilin resistance	Genewiz
pPM-GFP-HIS	CMV promoter, EGFP, Kanamycin resistance	Gift from AG Hasenfuß/ Vanessa Hindmarsh
pCMV-MRAS-myc-FLAG	CMV promoter, full-length MRAS, Kanamycin resistance	Origene
pCMV-NRAS-myc-FLAG	CMV promoter, full-length NRAS, Kanamycin resistance	Origene
pCMV-HRAS-myc-FLAG	CMV promoter, full-length HRAS, Kanamycin resistance	Origene

3.11 Devices

Table 14: Devices

Application	Device	Manufacturer
Cell counting	Countess II FL Automated Cell Counter CASY Model TT	Thermo Fisher Scientific Innovatis
Cell culture incubator	BBD 6220	Thermo Fisher Scientific
Cell Freezing	Mr. Frosty	Nalgene
Centrifugation	Centrifuge 5418R Heraeus Pico 21 Heraeus Fresco 21 Multifuge X1R Mini-Centrifuge Sprout	Eppendorf Thermo Fisher Scientific Thermo Fisher Scientific Thermo Fisher Scientific Heathrow Scientific
Electrophoresis	OWL A2-BP Sub-Cell GT	Thermo Fisher Scientific Bio-Rad
Cell stimulator	MyoPacer cell stimulator	IonOptix
Controlled rate freezer	KRYO 560-16	Planer
Transfection unit	Amaxa Nucleofector II device 4D-Nucleofector Core Unit	Lonza
Heating block	Thermomixer compact ThermoMixer F1.5	Eppendorf Eppendorf
Immunoblotting	Trans-Blot Turbo Transfer System	Bio-Rad
Imager Gels/ Membranes	ChemiDoc XRS+	Bio-Rad
Low temperature freezers	Forma 88000 CryoPlus 2	Thermo Fisher Scientific Thermo Fisher Scientific
Magnetic stirrer	MR Hei-Standard	Heidolph
Microscopes	LSM 710 PrimoVert Incucyte	Zeiss Zeiss Sartorius
Microelectrode array system	Maestro Pro	Axion BioSystems
PCR Cycler	Mastercycler nexus X2 Eco	Eppendorf

Pipettes	Research plus 1000 µl Research plus 100 µl Research plus 10 µl Research plus 2,5 µl Accu-jet pro	Eppendorf Eppendorf Eppendorf Eppendorf Brand
Spectrophotometer	NanoPhotometer N60	Thermo Fisher Scientific
Tissue Lyser	TissueLyser LT	Qiagen
Tube Rotator	Mini Tube Rotator 15534080	Thermo Fisher Scientific
Water bath	Waterbath WNB7	Memmert
pH Measurement	inoLab pH 7110	WTW
Power supply	PowerPac 300	Bio-Rad
Real Time PCR Cycler	7900HT Fast Real-Time PCR System	Applied Biosystems
Sterile working bench	Safe 2020	Thermo Fisher Scientific
Vortexer	Vortex Genie 2	Thermo Fisher Scientific
Balances	CPA225D ED523S-P0CE	Sartorius Sartorius

3.12 Software

Table 15: Software

Product	Version	Manufacturer
ABI 7900 HT SDS	2.4	Applied Biosystems
Adobe Illustrator 2019	23.0.3	Adobe Systems
Adobe Photoshop	13.01	Adobe Systems
AxIS Navigator	2.0.3	Axion BioSystems
Cardiac Analysis Tool	2.2.7	Axion BioSystems
Citavi	6.8	Swiss Academic Software
Chromas	2.6.4	Technelysium Pty Ltd
DNADynamo	1.46	Blue Tractor Software
Excel	2013/ 365	Microsoft
Flowing	2.5.1	Perttu Terho

GraphPad Prism 8	8.4.2	GraphPad Software
ImageJ	1.49t	National Institutes of Health
ImageLab	6.0	Bio-Rad
IncuCyte	S3 2019 A	Sartorius
LabChart Pro	V8.0.5	ADInstruments
Power Point	2013/ 365	Microsoft
Serial Cloner	2.5	SerialBasics
STARLIMS10.Prod	STARLIMS v11	Abbott
Word	2013/ 365	Microsoft
Zen	2.3	Carl Zeiss

3.13 Statistical analysis

All data were analyzed using GraphPad Prism 8

3.14 Cell biological methods

3.14.1 Transformation of bacteria

One vial of NEB 10-beta competent *E. coli* cells was thawed on ice for 10 min before 50 ng plasmid diluted in 5 µl ddH_2O was added to the cells. Samples were carefully stirred with the pipette tip and incubated for 30 min on ice followed by a heat shock at 42 °C for 30 sec. The tube was incubated on ice for 5 min before 250 µl SOC medium was added. The sample was incubated at 37 °C for 60 min while rotating at 850 rpm. Following incubation, 10 µl and 100 µl cell suspension were spread onto separate LB agar plates containing adequate antibiotics (1 µg/ml). Plates were incubated overnight at 37 °C.

3.14.2 Cultivation and maintenance of iPSCs

For coating, 1 ml diluted Matrigel was added per well of a 6-well dish and incubated for 45 min at 37 °C or overnight at 4 °C prior to seeding cells.

Glass cover slips were first incubated in 0.1% HCl overnight and subsequently incubated in 70% ethanol overnight. Cover slips were cleaned with lint-free tissues and sterilized at 200 °C

for 2 h. Glass cover slips were coated with 500 µl diluted Matrigel and incubated for 45 min at 37 °C or overnight at 4 °C before seeding cells.

iPSCs were passaged to new Matrigel coated plates twice per week or when reaching a confluency of 80-90%. Cells were washed twice and incubated with prewarmed Versene solution for 3 min. Versene solution was removed and cells were carefully flushed off the plate with 1 ml StemMACS iPS-Brew XF or StemFlex medium supplemented with 2 µM TZV. Depending on desired densities, 50-125 µl cell suspension was transferred to a new Matrigel-pretreated 6-well dish containing 2 ml per well of StemMACS iPS-Brew XF or StemFlex medium supplemented with 2 µM TZV. After 24 hours of incubation at 37 °C and 5% CO_2, medium was aspired and replaced by 2 ml StemMACS iPS-Brew XF or StemFlex without TZV. Medium was changed every day. For cardiac differentiation, iPSC passages 15-50 were used.

3.14.3 Direct differentiation of iPSCs into iPSC-CMs

iPSCs were cultured in StemMACS iPS-Brew XF Medium on Matrigel (diluted 1:60-1:120) coated plates. Differentiation into CMs was started with a confluence of 70-90%. Cells were treated with Cardio Differentiation medium supplemented with 6 µM CHIR99021 for 48 h. Afterwards, medium was changed to Cardio Differentiation medium supplemented with 5 µM IWP2 for 48 h. Medium was changed to Cardio Culture on day 7 and renewed every other day. Cells were digested and replated to obtain lower cell densities between day 12 and 15. Following digestion, metabolic selection was started on day 14-17 with Cardio Selection medium for 7 days with medium change every other day. Subsequently, medium was changed back to Cardio Culture Medium for further cultivation. Differentiation efficiency was analyzed by FACS analysis and visual observation of the contracting cells.

3.14.4 Digestion and selection of iPSC-CMs

To achieve lower cell densities and obtain a purified cardiomyocyte population, iPSC-CMs were digested followed by metabolic selection. For this, iPSC-CMs on day 14-18 were washed once with PBS and incubated with TrypLE select Enzyme (10X) for 10 min at 37 °C and 5% CO_2. Detached cells were transferred to a 15 ml tube containing 1 ml fetal bovine serum (FBS). Cells were centrifuged at 100x g for 10 min and the supernatant was aspired. Cells were resuspended in Cardio Digestion medium, counted with the Casy CASY cell counting system and $1x10^6$ – $2x10^6$ cells were seeded onto Matrigel coated 6-well dishes containing 2 ml Cardio

Digest medium. Medium was changed to Cardio Selection medium after 2 days and changed every 2-3 day for a total of 1 week. Subsequently, cells were maintained in Cardio Culture medium.

3.14.5 Freezing and thawing of iPSCs

For cryopreservation of iPSCs, cells were washed once with PBS and incubated for 3 min with Versene solution. The solution was aspired, and cells were flushed off the plate with 500 µl StemMACS iPS-Brew or StemFlex medium and transferred to cryopreservation tubes containing 500 µl of the respective medium containing 4 µM TZV and 20% DMSO. Tubes were placed in a Mr. Frosty cell freezing container and stored at -80 °C for a minimum of 2 h before transferring them into a liquid nitrogen freezer for long term storage at -150 °C.

For recovery of iPSCs, cryopreservation tubes were thawed in a 37 °C water bath and transferred into a 15 ml tube containing 10 ml of appropriate medium (either StemMACS iPS-Brew or StemFlex depending on the medium used for freezing) supplemented with 2 µM TZV. iPSCs were centrifuged at 200x g for 5 min. The supernatant was aspired, and cells were resuspended in 2 ml StemMACS iPS-Brew or StemFlex supplemented with 2 µM TZV. Cells were seeded onto Matrigel-precoated 6-well dishes containing 2 µl medium with 2 µM TZV and incubated at 37 °C and 5% CO_2. Medium was aspired and replaced with fresh medium without TZV on the next day, followed by daily medium change.

3.14.6 Freezing and thawing of iPSC-CMs

For cryopreservation of iPSC-CMs, cells were washed once with PBS and incubated with 1 ml 0.25% Trypsin-EDTA for 10 min at 37 °C. Subsequently, the cell solution was transferred into a 15 ml tube containing 1 ml Cardio Cryopreservation medium and centrifuged at 100x g for 10 min. The medium was aspired, and cells were resuspended in 1-5 ml of Cardio Cryopreservation medium, depending on pellet size. Cells were counted using the CASY cell count system. 5 million cells were transferred into a cryopreservation tube and total volume was adjusted to 1.5 ml with Cryopreservation medium. The freezing process was performed with a controlled rate freezer, allowing controlled freezing of -1 °C per min up to -90 °C. Cardiomyocytes were long term stored at -150 °C.

For recovery of iPSC-CMs, cryopreservation tubes were thawed in a 37 °C water bath and cells were transferred into a 15 ml tube containing 10 ml Cardio Digestion medium. Cells were centrifuged at 100x g for 10 min. The supernatant was discarded, and cells were resuspended in Cardio Digestion medium. iPSC-CMs were seeded onto Matrigel precoated 6-well culture dishes containing 2 ml of Cardio Digestion medium and incubated at 37 °C and 5% CO_2. After 1-2 days, the medium was changed to Cardio Culture medium.

3.14.7 Lipofectamine based transfection of iPSC-CMs

Lipofectamine based plasmid transfection in iPSC-CMs was performed using the Lipofectamine Stem Transfection Reagent Kit according to the manufacturer's instructions. Cells were seeded on 4-well chamber slides 5-7 days prior to transfection (40.000 CMs/well). For each well, 1 µl Lipofectamine Stem Reagent and 500 ng per plasmid were diluted in 50 µl Opti-MEM medium and incubated for 10 min at RT. During the incubation step, the medium of the iPSC-CMs was replaced by 500 µl Opti-MEM medium. Subsequently, the DNA-lipid complex was added to the cells. A separate well of iPSC-CMs was transfected with a plasmid carrying an eGFP, serving as a positive control. Transfected cells were incubated at 37°C and 5% CO_2 for 3 h before 1 ml fresh Cardio Culture was added in each well. After 24 h total incubation time, cells were fixed for immunostaining.

3.14.8 CRISPR/Cas9 mediated genome editing

LZTR1-KO iPSC lines were generated via CRISPR/Cas9. Mutations were introduced into wildtype iPSC lines WT1 and WT2. Exon 1 or exon 17 of *LZTR1*, mimicking the maternal or paternal mutation respectively, were chosen as targets for the guide RNAs. For exon 1, two guide RNAs were used while only one guide RNA was used for targeting exon 17. All steps were performed under sterile conditions. Early iPSCs passages (<20) were chosen for genome editing.

Alt-R CRISPR-Cas9 crRNA (100 µM) and Alt-R CRISPR-Cas9 tracrRNA (100 µM) were mixed in a 0.5 ml tube and incubated at 95 °C for 5 min. The mixture was allowed to cool down to RT. 6 µl of that mixture and 2 µl of Cas9 nuclease were mixed and incubated at RT for 20 min. Subsequently, 82 µl Nucleofector solution, 18 µl Nucleofector supplement were added to the tube. For transfections without DNA repair template, 1 µl of Electroporation Enhancer (100 µM)

was added. For HDR based approaches, 6-12 µg of the DNA donor template was added instead of the Electroporation enhancer.

Prior to transfection, iPSCs at a confluence of 70-80% were treated with 2 µM TZV for 1 h. Medium was aspired, and cells were incubated with Versene for 5 min at RT. Versene was aspired and cells were flushed off the plate with StemFlex medium. The cells were counted with the Casy cell counter system, $2x10^6$ cells were transferred into a 15 ml tube and centrifuged for 3 min at 200x g. iPSCs were resuspended in the nucleofection solution, transferred to a nucleofector cuvette and immediately electroporated with the 4D-Nucleofector system using program CA-137. Following transfection, cells were diluted in 300 µl StemFlex medium and seeded in two wells of a 6-well dish containing StemFlex medium, 2 µM TZV and 1x Pen/Strep. For transfections that aimed at insertion of a template DNA fragment via HDR, 20 µM HDR-enhancer was added immediately after transfection and seeding. After 20 h, medium was replaced with fresh StemFlex medium. For singularization of clones, single cells were picked with the automated CellenOne system and replated in a 96 well dish with one cell per well. Alternatively, single colonies were picked manually. Expanded colonies were analyzed by Sanger sequencing and positive clones were selected for differentiation and analysis.

Table 16: Components for the CRISPR-RNA mix

Component	Amount (µl)
Alt-R CRISPR-Cas9 crRNA (100 µM)	5
Alt-R CRISPR-Cas9 tracrRNA (100 µM)	5

Table 17: Components for the CRISPR-RNP complex

Component	Amount (µl)
Cas9 nuclease (10 µg/µl, 61 µM)	2
CRISPR-RNA mix (Table 16)	6

Table 18: Components for the final nuclecofector mix

Component	Amount (µl)
Nucleofector solution	82
Nucleofector supplement	18
CRISPR-RNP complex	8
(optional) DNA donor template (100 µM)	2-4 µl (6-12 µg)
(optional) Electroporation Enhancer (100 µM)	1

Table 19: Guide RNAs used for CRISPR/Cas9 based genome editing

Component	Amount (µl)
LZTR1_Ex1_CR1	5'-AGCACGGGGGGGCAGATCG GGG-3'
LZTR1_Ex1_CR2	5'-GCACCCACGAACTCGTCGC AGG-3'
LZTR1_Ex17_CR1	5'-CCAGGTATGCCTTCATGTCC TGG-3'
LZTR1_C-Term_CR1	5'-GAGCTGGGCGCCGACATCTG AGG-3'
LZTR1_N-Term_CR3	5'-CTGCCCGGTCCAGCCATCCC GGG-3'

A

```
  1 ATAGACTCCC TGGCCTCCCA CATCTCAGAC AAGCAGTGCG CAGAGCTGGG
 51 CGCCGACATC GGTAAGCCTA TCCCTAACCC TCTCCTCGGT CTCGATTCTA
101 CGTGAGGCCC TGTGGCGCCT GCCCATTGTG AAGAATCGCC GTGCCTGCCT
151 GCCCTGCCTA TG
```

B

```
  1 CCGGGGCGGT GGCCGCAAGT TGGGCTTACA GCGCGGCCGA TCCGGCGTGG
 51 ACCCGGGATG GGTAAGCCTA TCCCTAACCC TCTCCTCGGT CTCGATTCTA
101 CGGCTGGACC GGGCAGCACG GGGGGGCAGA TCGGGGCTGC GGCCCTGGCA
151 GCCGCCGCGC GG
```

Figure 7: ssDNA templates used for V5 insertion

ssDNA templates used for insertion of the V5 sequence in the **A,** C-terminal or **B,** N-terminal region of *LZTR1*. The 42 bp V5 sequence is labeled in green, stop codon in red, start codon in yellow. The V5 sequence is framed by 60 bp homology arms at each site.

3.14.9 Harvesting of iPSCs and iPSC-CMs

For each well of a 6-well dish, medium was aspired, and cells were washed once with 1 ml PBS. After renewing PBS, cells were gently detached with a cell scraper and transferred into a 1.5 ml tube. Cells were pelleted at 5000x g for 1 min. The supernatant was aspired, tubes were snap frozen in liquid nitrogen and kept at -80°C.

3.14.10 Cultivation of HEK293T cells

HEK293T cells were cultivated in 6-well dishes with 2 ml HEK medium per well. Cells were kept at 37 °C with 5% CO_2. For experiments, low passage HEK293T cells (<20) were used. Medium was changed daily, and cells were passaged when a confluency of 80% - 90% was reached. For passaging, medium was aspired, and cells were flushed off the plate with 1 ml fresh HEK medium per 6-well dish. 50 µl – 100 µl of the cell suspension was transferred to an uncoated new well of a 6-well dish containing 2 ml of fresh HEK medium.

For cryopreservation of HEK293T cells, wells with ~80% confluency were chosen. Medium was aspired, cells were rinsed carefully with 1 ml of PBS and flushed off the plate with 1 ml of fresh HEK medium. The cell suspension was transferred to a 15 ml tube containing 9 ml of HEK medium and centrifuged at 1000 rpm for 5 min. The supernatant was aspired, and cells were resuspended in 2.4 ml FBS. Dropwise, 300 µl DMSO was added. Cells were mixed gently, and 1 ml of suspension was transferred to cryotubes. Tubes were placed in a Mr. Frosty cell freezing container and stored at -80 °C.

For recovery of HEK293T cells, frozen tubes containing HEK293T cells were thawed in a 37 °C waterbath. The cell suspension was transferred into a 15 ml tube containing 10 ml HEK medium. After centrifugation for 5 min at 1000 rpm, the supernatant was removed, and cells were resuspended in 1 ml fresh HEK medium. 300 µl and 600 µl of cell suspension were transferred each into one well of a 6 well plate containing 2 ml of HEK medium. Cells were kept at 37 °C with 5% CO_2 and medium was changed daily.

3.14.11 Lipofectamine based transfection of HEK293T cells

Transfection of HEK293T cells was performed using the Lipofectamine 3000 Transfection Reagent Kit according to the manufacturer's instructions. Cells were seeded in 6 well plates 1-2 days prior to transfection. Transfection was performed at a confluence of 50%.

Per well, 7.5 µl Lipofectamine 3000 Reagent was mixed with 125 µl Opti-MEM Medium. In an additional tube, 125 µl Opti-MEM Medium was mixed with 1-5 µg Plasmid-DNA and 10 µl P3000 Reagent. 125 µl of each tube was mixed and incubated for 15 min at RT before adding to the HEK293T cells. Cells were incubated at 37 °C and 5% CO_2 for 48 h before analysis. A separate well of HEK293T cells was transfected with a plasmid carrying an eGFP, serving as a positive control.

3.14.12 Confocal calcium imaging

In this thesis, cytosolic calcium levels were measured with the fluorescent calcium indicator Fluo-4 AM (acetoxymethyl ester of Fluo-4), a membrane permeable dye. In presence of cytosolic calcium, Fluo-4 emits fluorescent signals when exited at 488 nm (Guatimosim et al. 2011).

For cytosolic calcium recordings of live iPSC-CMs, 80,000 cells with a minimum age of 53 days were replated on a 25 mm glass coverslip precoated with Matrigel (dilution 1:60). Prepared iPSC-CMs were cultured for a minimum of 7 days before the experiment was performed. The cells were stained with 5 µM Fluo-4 AM and 0.02% Pluronic F-127 for 20 min at RT. Following incubation, the staining solution was discarded, cells were washed once with Tyrode´s solution and kept in fresh Tyrode´s solution throughout the measurement. For recordings, iPSC-CMs were paced with 0.25 Hz at 18 V and 3 ms stimulus duration. Calcium recordings were performed with the line scan mode using the LSM 710 confocal microscopy system and the 63x oil objective with the following settings: 1057.7 Hz; 20,000 cycles; pinhole 6 AU; 512x512 pixels; 45 µm scanning width. iPSC-CMs were used for recordings between day 68-89. Cells were measured at basal conditions or after treatment with the L-type calcium channel inhibitor verapamil. For recordings under drug conditions, Tyrode´s solution of iPSC-CMs was supplemented with 100 nm verapamil and cells were incubated at RT for 20 min before measurement. Calcium sparks were analyzed with the SparkMaster plugin for imageJ with the following settings: scanning speed 1057.7 lps; pixel size 0.088 µm; background 0 Fl. U.; criteria 3.3; number of intervals 3. The diastolic region (1 s, 40 µm) of the last recorded calcium transient (CaT) per cell was screened for calcium sparks. Sparks that were recognized by the SparkMaster plugin but did not exceed 0.1 ΔF/F0, full width of 1 µm and full duration of 5 ms were excluded from the analysis. The overall SR calcium leak for each recorded cell was defined as the sum of all detected spark sizes, whereas the spark size was calculated as the product of amplitude, full width and full duration.

Four CaTs were recorded for each cell. Raw data were subjected to polynomial smoothing (20 neighbors) (Savitzky and Golay 1964). Smoothed CaTs were analyzed with LabChart Pro 8, using the Peak Analysis Tool with the following settings: automatic recognition of resting membrane potential, TStart 15% of height away from resting membrane potential. TRise and TFall were defined as between 0% and 100% of the peak height. CaT rise time is defined as the time from the start to the peak of the CaT. CaT decay 50% is defined as the time from the peak of the CaT to 50% signal decay.

3.14.13 Cell size measurements of iPSC-CMs

For determining the cell areas of adherent iPSC-CMs, desired cell lines with a minimum age of 50 days were replated in 12-well format with densities of 25,000 CMs/well (6580 CMs/cm²). After 10 days of recovery, cells were imaged with the Incucyte system. Cell were encircled manually, and total cell area was calculated with imageJ.

Cell diameter in suspension was assessed after taking images with the Incucyte imaging system for calculation of the cell areas. Medium was aspired and iPSC-CMs were washed once with 1 ml PBS. PBS was removed and cells were covered with 500 µl accutase containing 0.025% trypsin per well and incubated for 15 min at 37 °C and 5% CO_2. Subsequently, detached cells were transferred into 1.5 ml tubes containing 500 µl FBS and centrifuged for 10 min at 100x g. The supernatant was aspired, and the pellet was resuspended in 125 µl FBS and 125 µl Cardio Culture medium. The suspension was transferred to a CASY tube containing 10 ml CASY-TON buffer. Measurements were performed with the CASY system and saved for analysis.

3.14.14 Calculation of co-localization

Co-localization was assessed with ImageJ. Channels to analyze were split and set to 8-bit mode. Per cell, 2-3 cytosolic areas were encircled with the polygon selection tool, not crossing cell borders or the nucleus before running the “Coloc 2” tool, using the standard presetting with adjusted ROIs for analysis. Calculated values for “Pearson's R value (no threshold)” were used for export.

3.14.15 Multielectrode arrays (MEA)

For electrophysiological analysis of iPSC-CMs recorded from whole wells, the Maestro PRO MEA platform was used. iPSC-CMs between day 65-82 were replated onto the electrode area of the Cytoview MEA 96-well plates with 100,000 cell per well. After seeding, cells were cultured in Cardio Culture medium for a minimum of 10 days before measurement. Recordings were acquired at 37 °C and 5% CO_2. Per cell line, 3 independent differentiations were used with 6 technical replicates per differentiation. For recordings, intervals of 5 min were recorded on 3 different days and results were averaged. The raw data was processed with AxIS Navigator 2.0.3 software and the Cardiac Analysis Tool 2.2.7. Contractility data was acquired with the following settings: minimum beat period 200 ms, maximum beat period 60 s, minimum active electrodes ≥1. Raw data were automatically screened for the region of 30 beats with the most stable beat period.

Field potential data was acquired using the following settings: detection threshold 200 µV, minimum beat period 200 ms, maximum beat period 60 s, post spike detection hold-off 90 ms, minimum active electrodes ≥1. Raw data were automatically screened for the region of 30 beats with the most stable beat period. Fridericia correction was applied to normalize FPD data to beat rate (FPDc). Beat-to-beat variability was defined as the standard deviation of individual beat periods from the mean beat period in percent.

3.15 Molecular analysis

3.15.1 gDNA isolation from cells

For isolation of genomic DNA of iPSC or iPSC-CMs the QIAamp DNA Mini kit (Qiagen) was used. Cell pellets were resuspended in 200 µl PBS. 20 µl Proteinase K and 200 µl Buffer AL was added and samples were vortexed briefly. Samples were incubated at 56 °C for 10 min while shaking with 800 rpm. Subsequently, 200 µl 100% ethanol was added and samples were vortexed briefly. The mixture was loaded onto a spin column and centrifuged for 1 min at 8000x g. 500 µl Buffer AW1 was loaded onto the column and the sample was centrifuged for 1 min at 8000x g. 500 µl Buffer AW2 was loaded onto the column followed by centrifugation for 3 min at 17900x g. Columns were transferred into a fresh 1.5 ml tube and 50 µl nuclease-free water was added directly onto the silica membrane. Samples were incubated at RT for 1 min before DNA was eluted by centrifugation for 1 min at 8000x g. DNA concentration was determined using NanoPhotometer N60. Samples were stored at -20 °C.

3.15.2 RNA isolation from cells

RNA from cells was isolated using the SV Total RNA Isolation System kit (Promega). All centrifugation steps were performed at 13000x g. Cell pellets were resuspended in 400 µl RNA lysis buffer. 400 µl of 95% ethanol was added and mixed gently. The mixture was transferred to a spin column assembly and centrifuged for 1 min. The column was washed with 600 µl RNA wash solution and centrifuged again for 1 min. 50 µl DNase mix was pipetted directly onto the silica membrane and the sample was incubated at RT for 15 min. Subsequently, the spin column was centrifuged for 1 min. 200 µl DNase stop solution was loaded onto the membrane and centrifuged for 1 min. The column was first washed with 600 µl RNA wash solution and centrifuged for 1 min followed by a second wash step with 250 µl RNA wash solution and centrifugation for 2 min. Finally, the column was transferred to a new 1.5 ml tube and the RNA was eluted with 50 µl nuclease-free H_2O by centrifugation for 1 min. RNA concentration was determined using NanoPhotometer N60. Isolated RNA was stored at -80°C.

3.15.3 cDNA synthesis

To obtain cDNA, isolated RNA was reverse transcribed using the SuperScript IV Reverse Transcriptase Kit (Thermo Fisher Scientific). Master mix 1 was prepared in a PCR reaction tube according to Table 20 and 500 ng RNA diluted in 4 µl nuclease-free H_2O was added. The mixture was placed into a thermo cycler and the program according to table 21 was initiated. In the 5 min interval at 25 °C, 6 µl of master mix 2 was transferred into the reaction tube. The cDNA was stored at -20°C.

Table 20: Reagents for cDNA synthesis

Reagents for RT	Master mix 1	Master mix 2
Nuclease-free H_2O	8 µl	
Oligo (dT)16 primer (50 µM)	1 µl	
dNTP mix (10 mM)	1µl	
5x SSIV Buffer		4 µl
DTT (0.1 M)		1 µl
RNaseOUT RNase Inhibitor (40 U/µl)		0.5 µl
SuperScript IV Reverse Transcriptase (200 U/µl)		0.5 µl

Table 21: Cycler settings for cDNA synthesis

Temperature	Time
65°C	5 min
4°C	2 min
25°C	5 min
52°C	10 min
80°C	10 min
4°C	hold

3.15.4 Isolation of plasmid DNA from bacteria

Plasmid DNA from bacteria was isolated using the NucleoBond Xtra Midi Kit (Machery Nagel). A 2 ml starter culture of LB medium containing adequate antibiotics was inoculated with single bacterial colonies picked from an LB agar plate. The culture was incubated at 37 °C for 6 h at 150 rpm. 100 µl of the starter culture was added to 100 ml LB-medium containing adequate antibiotics and incubated overnight at 37 °C and 150 rpm (not exceeding 16 h). Following incubation, the bacterial culture was centrifuged at 4500x g for 15 min at 4 °C. The supernatant was discarded, and the pellet was resuspended in 8 ml resuspension buffer RES. 8 ml of lysis buffer LYS was added to the suspension, inverted and incubated for 5 min at RT. Meanwhile, columns and filters were assembled and equilibrated with 15 ml buffer EQU. 8 ml neutralization buffer NEU was added to the suspension, carefully inverted until becoming colorless and decanted in the prepared columns with filter. 5 ml buffer FIL-EF was used for washing the filter. A second washing step using 8 ml buffer WASH was performed. Plasmid DNA was then eluted into a 15 ml tube using 5 ml buffer ELU. The DNA was precipitated by adding 3.5 ml isopropanol to the eluate and loaded into a 30 ml syringe with a nucleobond finalizer attached to the outlet. The mixture was pressed slowly through the finalizer using minimal force. The flow-through was discarded and the syringe loaded with 2 ml of 70% ethanol pressed slowly through the finalizer. The finalizer was dried in the following step by pressing air through the filter repeatedly until no more ethanol leaked out. The finalizer was assembled to a 1 ml syringe filled with 200 µl endotoxin-free H_2O. DNA was eluted very slowly, drop by drop by inserting the plunger. The eluate was re-loaded into the syringe for a second elution step. Finally, air was pressed through the finalizer to force out as much eluate as possible. DNA concentration was measured using NanoPhotometer N60. Samples were stored at -20 °C.

3.15.5 Polymerase chain reaction (PCR)

To amplify desired DNA fragments, PCR reactions were performed. Depending on template length, either GoTaq- or Phusion DNA-Polymerase was used. The standard volume of a single reaction tube was 20 µl for Phusion and 25 µl for GoTaq. The program used on the thermocycler was dependent on the melting temperature of the primers and the length of the PCR product.

Table 22: Reagents used for a GoTaq polymerase PCR reaction, pipetted in the following order:

Reagent	Volume
Nuclease free H_2O	Up to 25 µl
5x Green GoTaq reaction buffer	5 µl
10 mM dNTPs	1.6 µl
10 µM Forward Primer	1 µl
10 µM Reverse Primer	1 µl
Template DNA	100 ng
GoTaq DNA-Polymerase	0.2 µl

Table 23: PCR standard program for Taq DNA Polymerase

Step	Temperature	Time
Initial Denaturation	95°C	2 min
30-38 Cycles	94°C	30 sec
	56-61°C	40 sec
	68°C	1 min per kb
Final Extension	68°C	5 min
Hold	4°C	∞

Table 24: Reagents used for a Phusion DNA-polymerase PCR reaction, pipetted in the following order:

Reagent	Volume
Nuclease free H_2O	Up to 25 µl

5x Phusion Green HF Buffer	5 µl
10 mM dNTPs	1.6 µl
10 µM Forward Primer	1 µl
10 µM Reverse Primer	1 µl
Template DNA	100 ng
Phusion DNA-polymerase	0.2 µl

Table 25: PCR standard program for Phusion DNA-polymerase

Step	Temperature	Time
Initial Denaturation	98°C	30 sec
30-38 cycles	98°C	5 sec
	58-72°C	30 sec
	72°C	15-30 sec per kb
Final Extension	72°C	5 min
Hold	4°C	∞

3.15.6 Quantitative real time PCR

The cDNA obtained from cDNA synthesis was used for the RT-qPCR in a 1:10 dilution. *GAPDH* was used as a reference gene. A 384-well plate was used for the reaction mixes listed in. The filled plate was sealed and transferred to the 7900HT Fast Real Time and the RT-qPCR was performed following the program listed in table 27. Melt curve analysis was performed and results were analyzed with the C_T ($\Delta\Delta C_T$) method (Livak and Schmittgen 2001) using the SDS 2.4 software and excel. All reactions were performed as triplicates.

Table 26: Reagents needed for RT-qPCR reaction (10 µl)

Reagent	Volume
Nuclease free H_2O	5 µl
SYBR Green master mix	3 µl
ROX passive dye	0.2 µl
10 µM Forward Primer	0.4 µl

10 µM Reverse Primer	0.4 µl
Template cDNA	1 µl

Table 27: Program for RT-qPCR

Step	Temperature	Time
Initial Denaturation	98 °C	180 sec
40 cycles	95 °C	10 sec
	95 °C	10 sec
	60 °C	30 sec
Melt curve up to 95 °C	+ 0.5 °C/cycle	6 sec /cycle
Hold	4 °C	∞

3.15.7 Agarose gel electrophoresis

Appropriate amounts of 1x TBE buffer were mixed with Agarose, stirred, and heated in the microwave until all agarose dissolved. After cooling down to 60 °C, Midori Green was added, and the mixture was slowly poured onto a horizontal gel chamber. The PCR reaction was mixed with 6x loading dye and loaded onto an agarose gel. An electric field (120 V; 200 mA) applied to the 1x TBE filled gel chamber causes the negatively charged DNA to migrate towards the positively charged anode. The size of the DNA fragments in the agarose gels was determined using GeneRuler 100 bp plus DNA ladder. Images were acquired using the ChemiDoc XRS+ system and ImageLab software.

Table 28: Reagents for a 1.5% agarose gel

Reagent	Amount
Agarose	0.75 g
1x TBE Buffer	50 ml
Midori Green	3 µl

3.15.8 DNA extraction from agarose gels

For extraction of DNA from agarose gels, the QIAquick Gel Extraction Kit (QIAGEN) was used. All centrifugation steps were performed at 17,900x g for 1 min at RT. DNA fragments were visualized via Midori Green and UV light, excised from the gel with a scalpel and dissolved completely in 200 µl buffer QG at 50 °C while shaking with 1000 rpm for 10 min. 60 µl isopropanol was added and the mixture loaded onto a spin column. The samples were centrifuged and the flow-through was discarded. 500 µl of Buffer GQ was loaded onto the column and the sample was centrifuged again. The flow-through was discarded and 650 µl Buffer PE was added onto the column. After 5 min incubation, the sample was centrifuged. Subsequently, the sample was centrifuged again without any liquid for removing buffer residues completely. The column was placed onto a 1.5 ml collection tube, 50 µl nuclease-free water was pipetted directly onto the silica membrane and the mixture was incubated for 4 min at RT. In a final centrifugation step, the DNA was eluted, and concentration was determined with NanoPhotometer N60. Samples were stored at -20 °C.

3.16 Protein chemistry

3.16.1 Total protein extraction

Protein was isolated from cell pellets for immunoblotting. Depending on size, the cell pellet was resuspended in ice cold 50-200 µl RIPA lysis buffer and incubated for 15 min on ice. Cells were centrifuged at 4 °C for 15 min at 14000x g. The supernatant was transferred into a new tube and was used for analysis. Protein concentration was determined using the Pierce BCA Protein Assay Kit according to the manufacturer's instructions. Protein samples were stored at -80°C.

3.16.2 Immunoblotting

Depending on the experiment, 5-50 µg protein was mixed with ddH_2O and 4x Laemmli Sample Buffer supplemented with 10% Beta-Mercaptoethanol to reach desired protein concentrations and volumes. Samples were incubated for 5 min in a thermoblock at 95°C and subsequently loaded onto a TGX stain-free cast gel (max. 15 µl sample per lane) in an electrophoresis chamber filed with 1x Running buffer. Gel was run for 30-45 min at 200 V and 20 mA. The gel was extracted from the plastic chamber and activated with UV light using the ChemiDoc XRS+. Proteins were transferred to a nitrocellulose membrane with the TransBlot Turbo system for 7

min at 1.3 A and 25 V. The membrane was then blocked with blocking buffer for 1 h at RT while rotating. Primary antibodies were diluted according to manufacturer's instructions and incubated in 5% milk in TBS-T over night at 4 °C.

On the following day, the membrane was washed 3x for 5 min with TBS-T before adding the appropriate secondary HRP antibody diluted 1:10,000 in 5% milk in TBS-T for 1 h at RT while rotating. The membrane was washed again 3x for 5 min with TBS-T. Subsequently, membranes were transferred into 50 ml tubes and incubated with 1 ml of SuperSignal West Femto Maximum Sensitivity Substrate for 3 min before protein bands were visualized using the ChemiDoc XRS+ system and ImageLab software.

3.17 Immunocytochemical analyses

Cells were seeded in low, monolayer forming densities on matrigel-coated 20 mm glass cover slips or in Matrigel coated chamber slides. For iPSCs, 25,000 or 15,000 cells were seeded, and allowed to form iPSC-typical colonies for 3-4 days before fixation. For iPSC-CMs, 60,000 or 40,000 cells were seeded, and allowed to settle to regain normal morphology for 7 days before fixation.

For fixation, cells were washed 3x with PBS and incubated with Roti-Histofix for 20 min. After three additional washing steps, cells were incubated in staining buffer at 4 °C until staining. The primary antibody was diluted in 150 µl cell permeabilization buffer and incubated overnight at 4 °C. On the next day, cells were washed again 3x with PBS and incubated with secondary antibody diluted in staining buffer for 1 h at RT. Cells were washed with PBS once and incubated with Hoechst33342 diluted 1:2000 in PBS for 10 min at RT. After three additional wash steps with PBS, cells were sealed. For this, glass cover slides with stained cells were mounted with Fluoromount-G and placed upside down on microscope slides. For cells stained in chamber slides, the plastic chamber was removed manually. Cells were covered in one drop of Fluoromount-G and the microscope slide was sealed with a cover slide.

4 Results

4.1 *LZTR1* overexpression in HEK293T cells

4.1.1 Overexpressed truncated LZTR1 shows altered subcellular localization and accumulates in cells

Biallelic *LZTR1* deficiency was previously shown to cause NS, a disorder which belongs to the class of RASopathies. Typically, RAS-MAPK signaling activity is upregulated in these class of diseases. To investigate whether LZTR1 interacts with various RAS isoforms and regulates RAS-MAPK signaling pathway activity, two different HA-tagged *LZTR1* variants were overexpressed in HEK293T cells via Lipofectamine for pathway analysis. The first construct codes for the full-length LZTR1 protein, while the second construct encodes a truncated variant which represents the NS-causing paternal allele from the previously presented Noonan family (Figure 3). Similar to the paternal mutation, this *LZTR1* variant leads to synthesis of a truncated protein of ~76 kDa, missing the second C-terminal BTB II and BACK II domains (Figure 8A). Additionally, a construct carrying a MYC-tagged CUL3 was co-overexpressed to avoid a potential bottleneck in RAS degradation mediated by the LZTR1-CUL3 complex. HEK293T cells transiently overexpressing these constructs were lysed 48h after transfection and immunoblotted with HA-antibody or LZTR1-specific antibody, showing both variants with their expected protein size. Notably, only the overexpressed LZTR1 could be recognized by the LZTR1-specific antibody, whereas endogenous LZTR1 levels could not be detected with this antibody (Figure 8B). In total, six different LZTR1 antibodies were tested in immunostaining and western blot in iPSCs and HEK293T cells, all failed to detect endogenous LZTR1. Both *LZTR1* variants were overexpressed in equimolar amounts, but the truncated variant resulted in much stronger bands in immunoblots. This finding was highly reproducible (>10 replicates). However, RT-qPCR revealed that the expression of both *LZTR1* variants was in comparable ranges and did not significantly differ from each other, indicating that the truncated protein accumulates in the cells. Markedly increased protein levels of a LZTR1 variant with a mutation in the BTB-BACK domain were also observed in another study (Frattini et al. 2013). These findings suggest that the protein degradation is impaired. Further, overexpression of HA-WT-LZTR1 or HA-mut-LZTR1 in HEK293T cells resulted in different subcellular localization. While the full-length LZTR1 showed a speckled pattern, the truncated LZTR1 variant was homogeneously distributed throughout the cytoplasm (Figure 8C). A comparable pattern was shown previously in HeLa- and HEK293T cells (Bigenzahn et al. 2018; Steklov et al. 2018). This was reproducible in our cell system and serves as prove of concept that this specific NS-

associated LZTR1 variant without the second BTB II and BACK II domains indeed alters the intracellular localization. Besides the altered localization, overexpression of HA-mut-LZTR1 resulted in an overall stronger immunofluorescence signal compared to the full-length construct, which is in line with the western blot results and supports the hypothesis that the truncated protein accumulates in the cells.

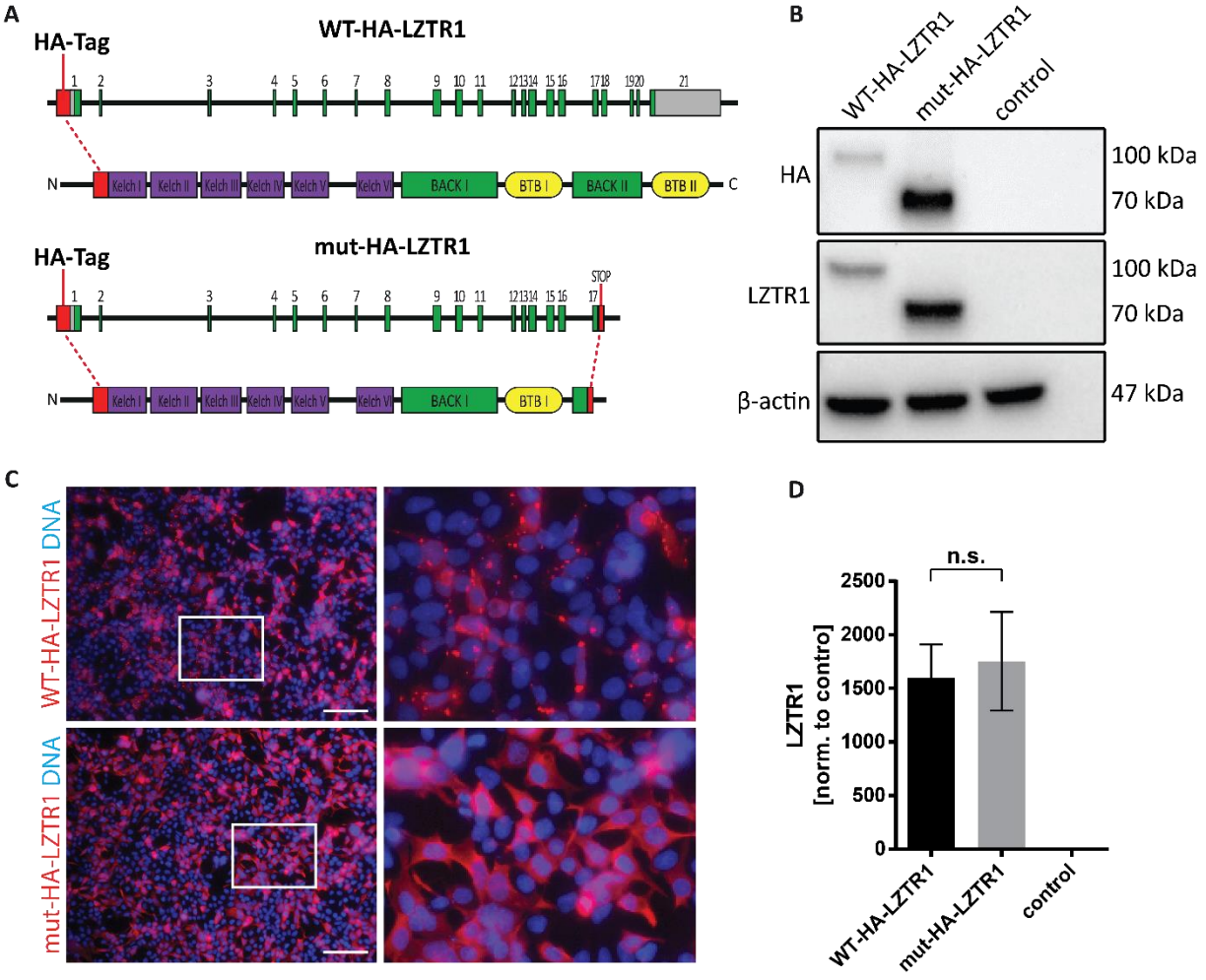

Figure 8: Truncated LZTR1 shows altered subcellular localization in HEK293T cells

A, Schematic illustration of WT and truncated LZTR1 overexpression constructs. Both variants carry an N-terminal HA protein tag. WT-HA-LZTR1 codes for the full length LZTR1 variant. mut-HA-LZTR1 introduces a stop codon in exon 17 and codes for a truncated variant, missing the second BACK and BTB domains. **B,** Lysates from HEK293T cells transiently overexpressing WT-HA-LZTR1 or mut-HA-LZTR1 were immunoblotted with HA or LZTR1 (sc-390166) antibody. Both overexpressed LZTR1 variants were detectable while endogenous levels are not detected by the LZTR1 antibody. **C,** HA-WT-LZTR1 overexpression HEK293T cells showed a speckled pattern, whereas mut-HA-LZTR1 was homogeneously distributed throughout the cytoplasm **D,** Validation of overexpression of the indicated constructs in HEK293T cells showed high expression levels of LZTR1 compared to non-transfected control, but no significant differences between WT-HA-LZTR1 and mut-HA-LZTR1. Three independent transfections for each sample were used for quantification, normalized to untransfected control and GAPDH. Scale bar= 100 µm. Data are presented as mean±SEM. n.s., not significant; P>0.05, determined by two-sided t.

4.1.2 The impact of LZTR1 on RAS levels

The interaction and affinity of LZTR1 to different RAS isoforms is still under debate and recent publications drew contradictory conclusions. In order to evaluate the degradative potential of LZTR1 for various RAS isoforms, WT-HA-LZTR1, mut-HA-LZTR1, CUL3-MYC and three different FLAG tagged RAS variants (MRAS-FLAG, NRAS-FLAG and HRAS-FLAG) were co-overexpressed in HEK293T cells (Figure 9D). Protein lysates were subjected to immunoblotting, revealing that MRAS-FLAG levels were reduced when co-overexpressed with WT-HA-LZTR1 but remained unchanged when co-overexpressed with mut-HA-LZTR1, compared to controls without overexpressed LZTR1 (Figure 9A). In contrast, protein levels of NRAS-FLAG (Figure 9B) and HRAS-FLAG (Figure 9C) were not affected and showed uniform expression in all samples.

To evaluate the effect of LZTR1 on endogenous RAS-MAPK signaling, WT-HA-LZTR1 or mut-HA-LZTR1 were overexpressed in HEK293T cells and lysates were immunoblotted for endogenous RAS levels. Interestingly, protein detected by pan-RAS antibody showed a light trend for lower abundance in combination with HA-LZTR1 overexpression but was not lowered significantly compared to mut-HA-LZTR1 samples (Figure 9F). Given the fact that the pan-RAS antibody detects KRAS, NRAS and HRAS but not MRAS (sup. Figure 40), this finding is concordant with the results from the RAS-isoform co-overexpression (Figure 9E) and also in line with a publication where LZTR1 was shown to interact with MRAS but not with KRAS, NRAS and HRAS (Castel et al. 2019). In contrast, Abe et. al showed that overexpression of *LZTR1* results in degradation of MRAS, NRAS, and HRAS in a dose dependent manner (Abe et al. 2020). Immunoblotting in HEK293T cells for endogenous MRAS produced unspecific bands probably due to its absence of expression, making this model system not optimal to investigate the possible interactions of LZTR1 with endogenous MRAS. Further, this raises the importance of a cell model with a natural expression of MRAS, which is highest expressed in muscle tissue, especially in the heart (Human Protein Atlas).

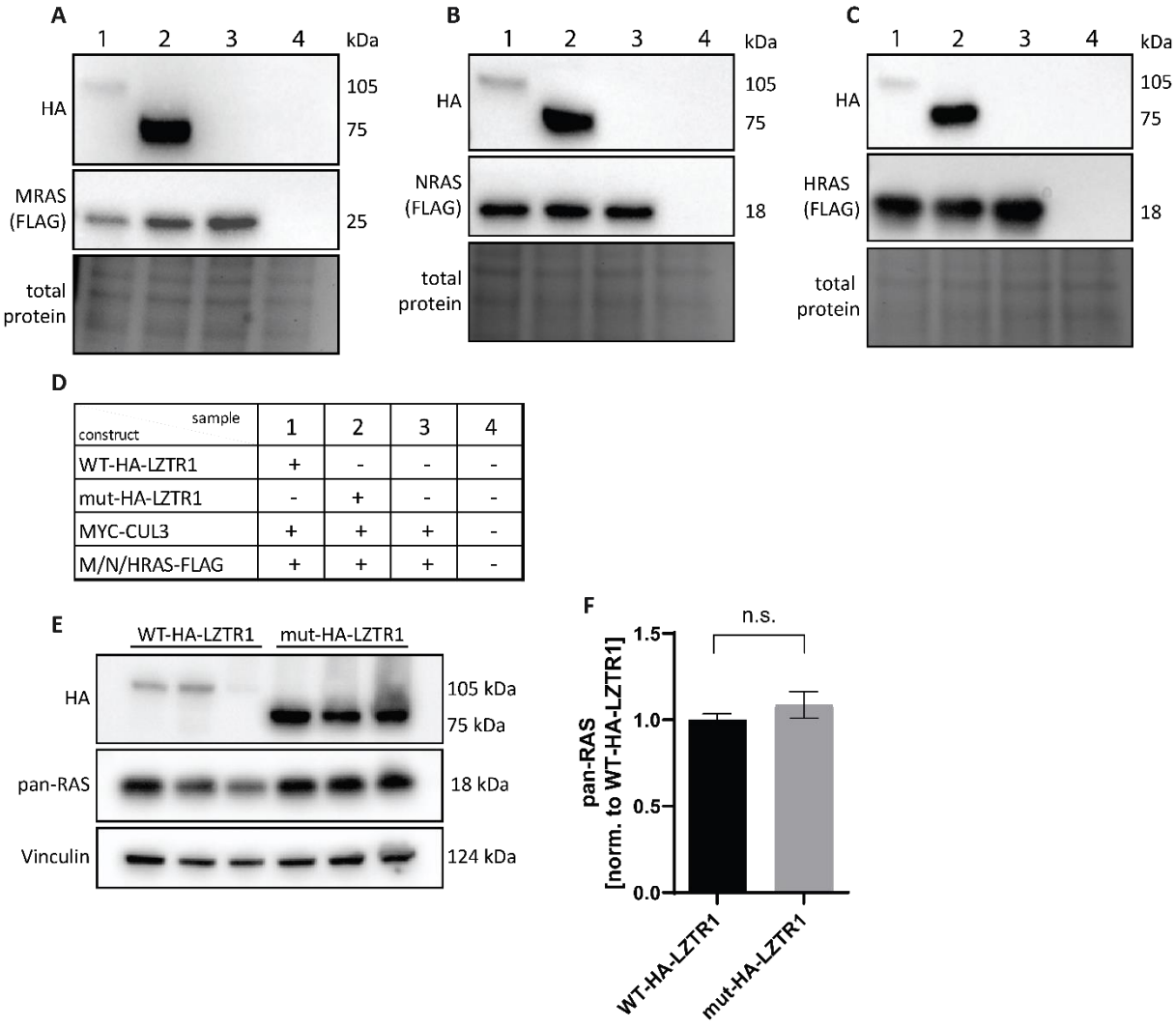

Figure 9: Full-length LZTR1 reduces MRAS protein levels in HEK293T cells

A-C, Lysates from HEK293T cells transiently co-overexpressing the indicated constructs were immunoblotted with HA and FLAG antibodies (n≥ 2 for each experiment), revealing that MRAS levels are reduced when WT-LZTR1 is co-overexpressed while NRAS and HRAS protein levels are not affected. **D,** Overview of co-overexpression combinations. **E,** Lysates from HEK293T cells transiently overexpressing either WT-HA-LZTR1 or mut-HA-LZTR1 were immunoblotted for HA-LZTR1 and endogenous pan-RAS. N=3 independent transfections for each sample. **F,** Quantification showed that endogenous RAS levels are not significantly changed. Data are presented as mean±SEM. n.s, not significant; P>0.05, determined by two-sided t-test.

4.2 CRISPR/Cas9 based tagging of *LZTR1* in iPSCs

The intracellular localization of LZTR1 was under debate within the last years. First described as golgi-associated protein (Nacak et al. 2006), it was later reported that LZTR1 might be located at recycling endosomes (Bigenzahn et al. 2018) and involved in vesicular trafficking

(Sewduth et al. 2020). However, these studies were mainly based on HEK293T and HeLa cell systems and the localization of LZTR1 was never investigated in iPSCs and iPSC-CMs before. In lack of antibodies that are capable to detect endogenous levels of LZTR1, we aimed to generate iPSC lines with a stable expression of a tagged LZTR1 variant. First, we tried a CRISPR/Cas9 mediated C-terminal insertion of a 711bp (233 amino acids) sequence, coding for mNeongreen, a fluorescent protein (Shaner et al. 2013; Hostettler et al. 2017). After several unsuccessful attempts (data not shown), we switched to the smaller V5 tag, a 42 bp (14 amino acids) sequence derived from the P and V proteins of the simian virus 5 family (Hanke et al. 1992). It is commonly used as protein tag for immuno-linked assays and was used as a tag for LZTR1 in overexpression constructs (Bigenzahn et al. 2018). Multiple lines were generated, carrying the V5 sequence either N-terminally immediately upstream of the start codon (LZTR1-V5-N), or C-terminally immediately before the stop codon (LZTR1-V5-C). Sanger sequencing confirmed heterozygous insertion of the complete V5 sequence (Figure 10A). The presence of the insert was also confirmed at transcriptional level in cDNA of tagged clones. Four and two final clones were generated for the C-terminal and N-terminal approach, respectively. However, LZTR1 could not be detected in western blots with a V5 specific antibody (R960-25) at the expected size of ~100 kDa (Figure 10B). Further, WT-iPSCs immunostained with V5 antibody showed a light background signal. The fluorescent signal from the V5-tagged iPSCs was not elevated above the background signal of the WT cells (Figure 10C). In contrast, a positive control (V5-Cav3) displayed robust expression, thereby excluding technical issues with the antibody specificity.

LZTR1 is only expressed in low levels (Hanses et al. 2020). Expression of this gene in iPSCs, HEK293T cells and human fibroblasts was confirmed via RT-qPCR, thereby showing that expression in HEK293T cells is higher compared to iPSCs and fibroblasts. To increase protein abundance, cell cultures were treated with MG132, an inhibitor of ubiquitin-dependent protein degradation (Lee and Goldberg 1996). After 6 or 24 hours of MG132 treatment, pellets were collected for protein isolation. Treatment with concentrations higher than 0.2 µM for 24 h caused cell death and could not be used for protein isolation (data not shown). The remaining samples were used for western blots with LZTR1 (sc-390166) and V5 antibodies. LZTR1 could not be detected, even after long-term exposure (Figure 10D). From these results, we conclude that the endogenous protein levels are too low for the used detection system.

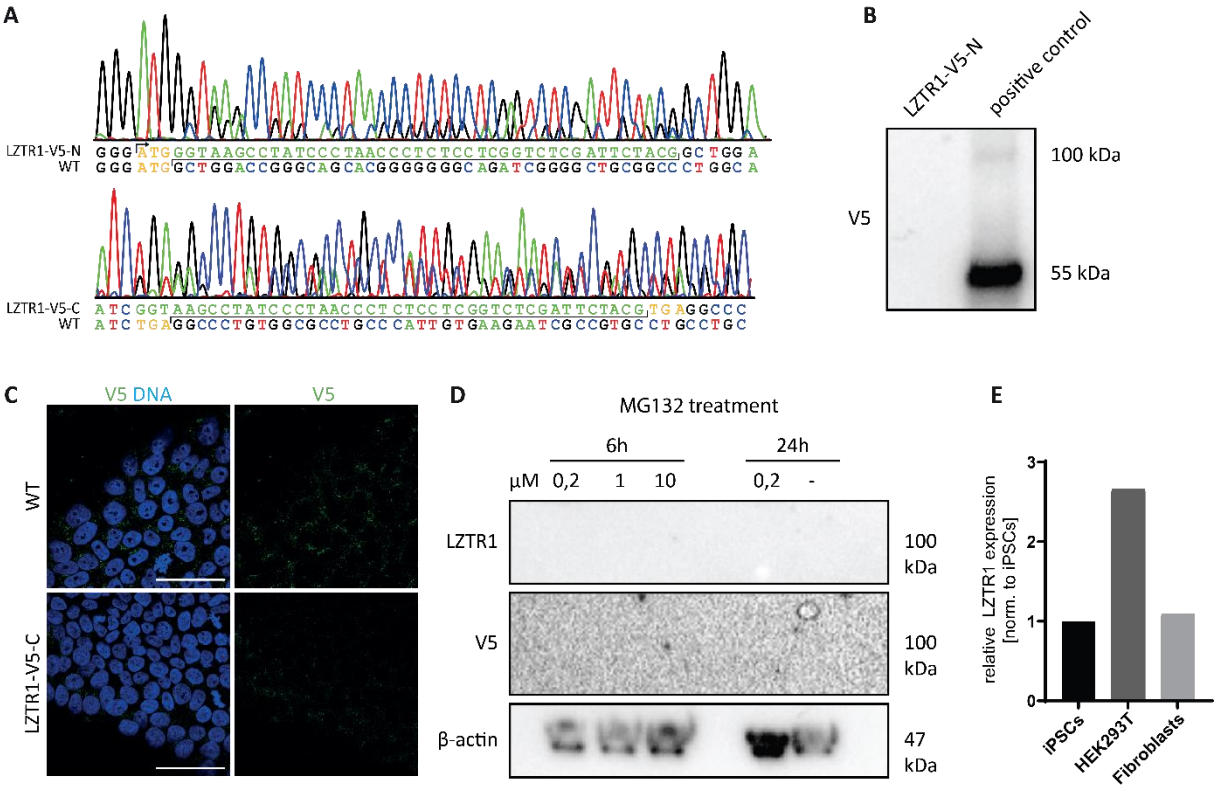

Figure 10: V5 tagging of *LZTR1* in iPSCs

A, Sanger sequencing results revealing successful heterozygous in-frame insertion of the V5 sequence. Inserted N-terminal directly following the ATG, or C-terminal, immediately before the stop codon. Shown are representative traces. **B,** LZTR1 is not detectable in western blots using V5-tagged LZTR1 iPSCs. **C,** Representative images of iPSCs with V5 C-terminally linked to LZTR1. No signal above background noise was detected. **D,** Western Blot analysis of MG132 treated V5-LZTR1 iPSCs showed no signal, even after long exposure. **E,** RT-qPCR confirming *LZTR1* expression in WT-iPSCs, HEK293T cells and human fibroblasts. Scale bar= 50 µm.

4.3 Generation of *LZTR1*-KO iPSC lines

Generation of proper controls is crucial in iPSC studies. In order to study the effects of mono- and biallelic *LZTR1* loss, frame-shifting mutations were introduced via CRISPR/Cas9 into well-established WT lines. The unedited WT lines served as isogenic controls in conducted experiments. By choosing exon 1 and exon 17 as targets for genome editing, the *LZTR1* mutations of the previously introduced case of the family with NS were remodeled (Figure 11A). Knockouts were introduced in two independent iPSC lines (WT1 and WT2).

For WT1, four *LZTR1*-KO lines were generated in total (Table 2). The first two cell lines carry mutations in exon 1 (one +/- and one -/- line). The remaining two cell lines carry mutations in

exon 17 (one +/- and one -/- line). Mimicking the maternal mutation, exon 1 was targeted in order to generate a frame shifting mutation with a premature stop codon. Two final cell lines were selected with mutations in exon 1. The first complete KO cell line (LZTR1 Exon 1 -/-) carries 1 bp insertions on both alleles each (c.135 dupT/A) while the second heterozygous cell line (LZTR1 Exon1 +/-) only has one allele edited (c.135 dupT) (Figure 11B). The paternal *LZTR1* mutation was remodeled by introducing frame shifting mutations in exon 17. In the homozygous LZTR1 Exon 17 -/- line, 5 bp were deleted on both alleles (c.13493 -5 bp; c.13494 -5 bp) while the heterozygous KO line (LZTR1 Exon 17 +/-) only carries a 5 bp deletion on one allele (c.13493 -5 bp) (Figure 11C).

For further validation and prove of reproducibility, two additional *LZTR1*-deficient iPSC lines were generated in the independent cell line WT2. In this approach, frameshifting mutations were introduced in exon 1 in a compound heterozygous manner for both cell lines (Table 2). In the first cell line (LZTR1 Exon 1 -/- B), 13 bp and 154 bp were deleted (c.123 -13bp; c.133 -154bp). In the second cell line (LZTR1 Exon 1 -/- C), 2 bp and 8 bp were deleted (c.133 - 2 bp; c.127 – 8 bp) (Figure 11D). As result of the frameshift mutations, no protein expression is expected. Indels resulting from the genome editing are limited to a few bp and result in a similar band size when compared to unedited controls as visualized in PCR gel images (Figure 11E). LZTR1 Exon 1 -/- B is an exception due to a deletion of 154 bp on one allele. This allowed isolation and sequencing of both alleles separately (Figure 11D, upper two sequences). A pedigree showing all generated cell lines and their respective WT line is depicted in Figure 11F.

After confirmation of successful genome editing of all selected clones by Sanger sequencing, pluripotency of all final clones was confirmed by immunostaining for the common pluripotency markers OCT4, NANOG and TRA1-60 (Figure 12a). The iPSCs further showed a normal morphology and formed iPSC-typical colonies (Figure 12B). Expression of pluripotency the markers OCT4 and TRA1-60 was also confirmed via flow cytometry in all genome edited cell lines, revealing between 94.81% and 98.92% double positive cells (Figure 12C). Digital karyotyping was performed for the *LZTR1*-KO cell lines based on WT1 and ensured integrity of all chromosomes (Figure 13A). A classical karyotyping was conducted for the generated cell lines based on WT2, LZTR1 Exon 1 -/- B and LZTR1 Exon1 -/- C, also confirming a normal set of chromosomes (Figure 13B).

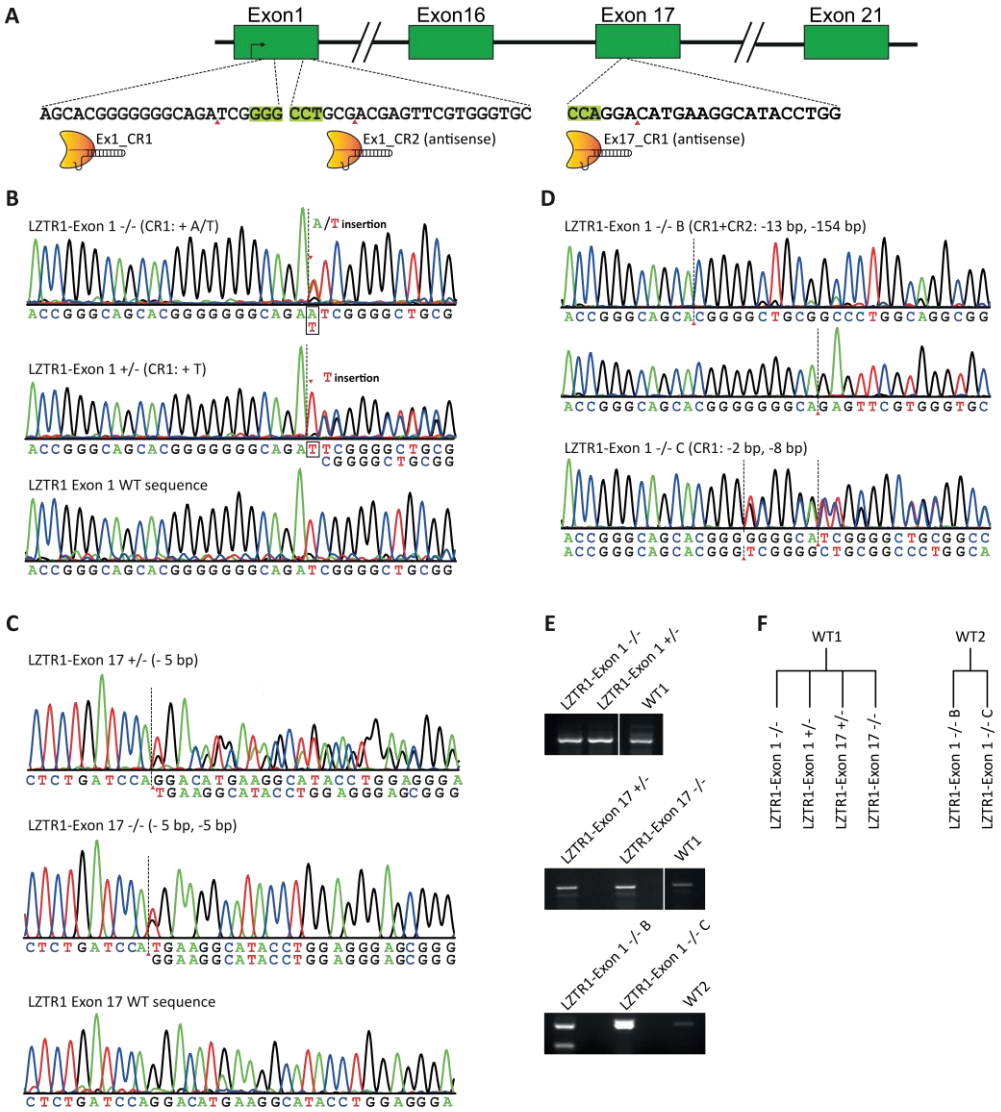

Figure 11: CRISPR/Cas9 based generation of *LZTR1*-KO iPSC lines

A, Schematic overview of gene editing strategy. Exon 1 was targeted by 2 guide RNAs while only 1 guide RNA was used for exon 17. **B-D,** Sanger sequencing results of the final clones confirming heterozygous and compound heterozygous KOs of *LZTR1*. **E,** PCR gel images of the final clones. Only the 154 bp monoallelic deletion of clone LZTR1-Exon 1 -/- B is clearly visualized while the small indels of the remaining clones were only detectable via sequencing. **F,** Pedigree of *LZTR1*-KO iPSC lines and their respective WT cell line.

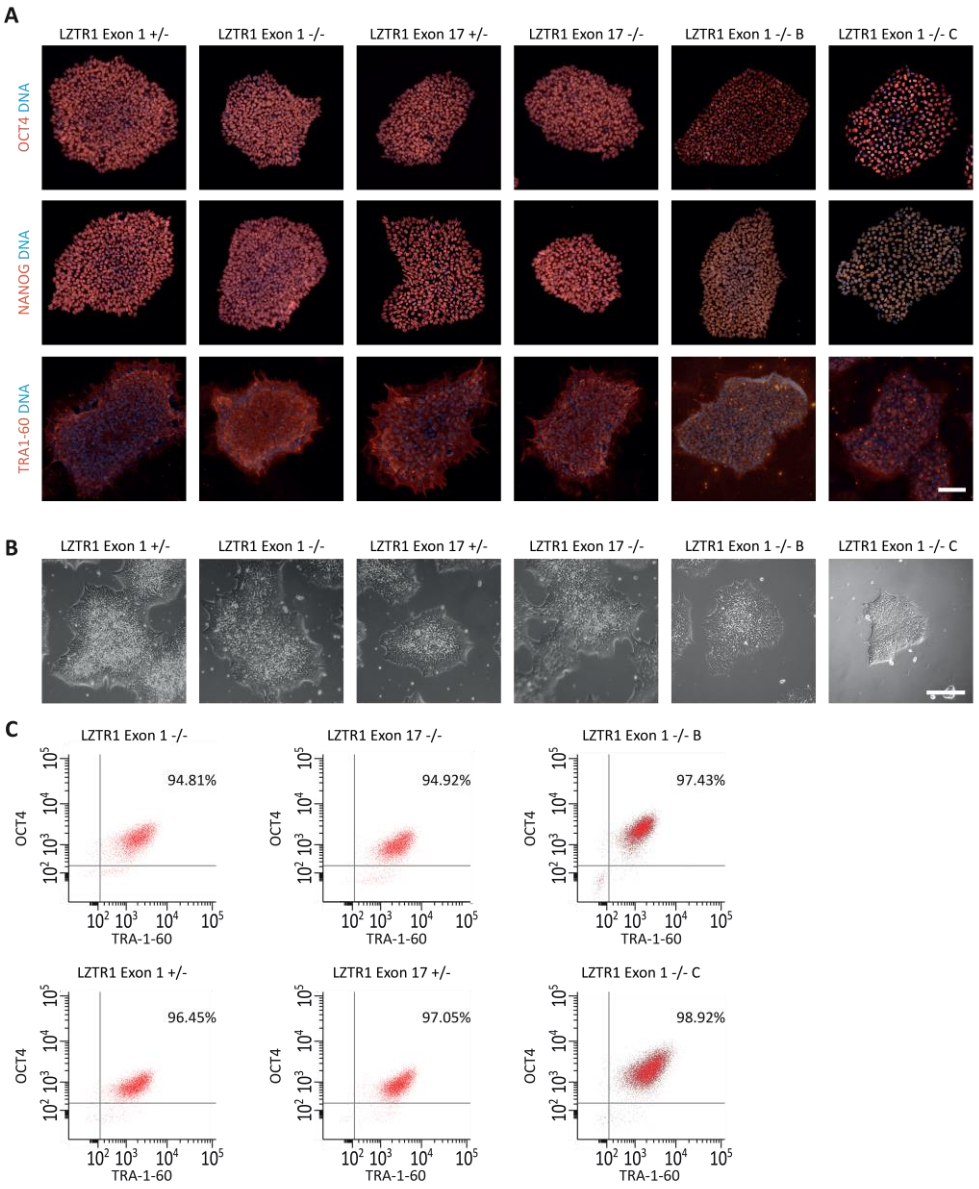

Figure 12: Confirmation of pluripotency of generated *LZTR1*-KO iPSC lines

Final *LZTR1*-KO iPSC clones were analyzed for expression of pluripotency markers and checked for normal morphology. **A**, Pluripotency of all final *LZTR1*-KO iPSC clones stained with antibodies pluripotency markers OCT4, NANOG and TRA1-60, scale bar= 100 µm. **B**, Representative images of living clones showing iPSC-typical morphology and formation of colonies, scale bar= 200 µm **C**, Flow cytometry further confirmed expression of pluripotency markers OCT4 and Tra1-60 in the *LZTR1*-KO iPSCs.

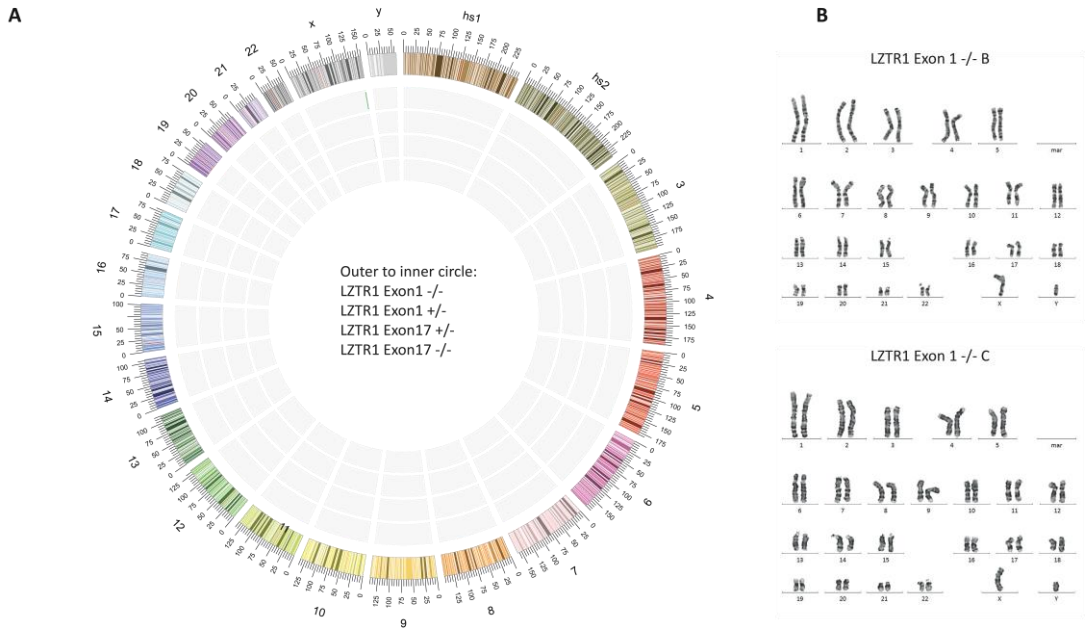

Figure 13: Karyotyping of CRISPR/Cas9 edited clones

A, Digital karyotyping of *LZTR1*-deficient iPSCs showed a small copy number variation (marked in green) in the X chromosome for cell line LZTR1 Exon 1 -/-. **B,** *LZTR1*-KO iPSCs (LZTR1 Exon 1 -/- B, LZTR1 Exon 1 -/- C) showed a normal karyotype.

4.4 *LZTR1*-KO iPSC-CMs show normal sarcomeric structure

Genome-edited iPSC lines with homo- or heterozygous loss of *LZTR1* and isogenic controls were directly differentiated into ventricular iPSC-CMs as described in a previous publication from our group (Kleinsorge and Cyganek 2020). First spontaneous contractions occurred approximately two weeks after the differentiation was initiated, confirming an already functional contractile system. All iPSC-CMs were cultured under standard conditions for a minimum of 60 days (d0= start of differentiation) before they were used for experiments, if not stated otherwise.

iPSC-CMs were immunostained for sarcomeric α-actinin to validate their successful differentiation. The cells displayed a round shaped or elongated morphology with a highly organized sarcomeric structure with a striated pattern (Figure 14). The formation of sarcomeric structures of *LZTR1*-deficient iPSC-CMs was not impaired compared to isogenic control iPSC-CMs.

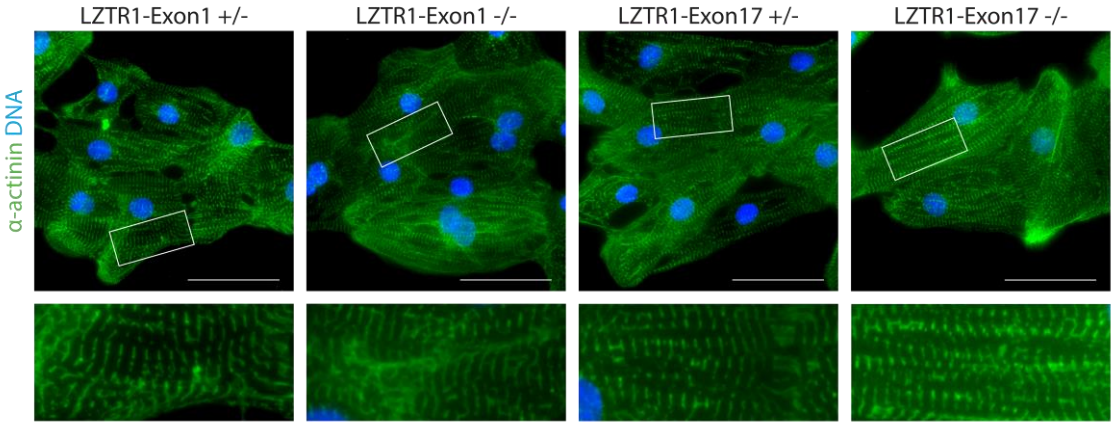

Figure 14: *LZTR1*-KO iPSC-CMs display a normal α-actinin striation

Representative images of ventricular differentiated iPSC-CMs immunostained for α-actinin (green) in *LZTR1*-KO iPSC CMs. All cells lines displayed a characteristic sarcomeric structure with a striated pattern. Nuclei were stained with Hoechst33342 (blue). Scale bar: 50 µm.

4.5 RAS-MAPK pathway activity analyses in *LZTR1*-KO iPSC-CMs

4.5.1 MRAS and Pan-RAS protein levels are not elevated in *LZTR1* +/- iPSC-CMs

NS is caused by mutations in genes that are involved in regulation of the RAS-MAPK pathway. Typically, these mutations result in enhanced pathway activity. To evaluate whether heterozygous loss of *LZTR1* is sufficient to trigger dysregulations of the RAS-MAPK pathway and to assess if the position of the mutation (exon 1 or exon 17) plays a role, heterozygous or compound heterozygous mutations were introduced in either exon 1 or exon 17 of *LZTR1*, resulting in four iPSC lines (Figure 11). Protein lysates of successfully differentiated iPSC-CMs of these new cell lines were analyzed via immunoblotting for RAS-MAPK pathway activity (Figure 15A). *LZTR1* -/- iPSC-CMs showed a trend for higher protein levels of MRAS and pan-RAS when compared to *LZTR1* +/- and WTs (Figure 15B-C). These results are in line with our previous study, where RAS protein levels detected by pan-RAS antibody were shown to be upregulated in iPSC-CMs derived from NS patients (Hanses et al. 2020). Although a trend for higher protein levels of pan-RAS and MRAS in samples with biallelic loss of *LZTR1* was observed, statistical tests did not result in significant findings due to only 4 differentiations per cell line. Unchanged protein levels of MRAS and pan-RAS in samples with heterozygous *LZTR1* loss indicate a preserved protein function, which is also in agreement with our patient data, where heterozygous *LZTR1* loss is not sufficient to cause NS (Hanses et al. 2020). No significant differences of MRAS and pan-RAS protein levels were detected between exon 1

and exon 17 KOs. For the first two WT lanes, especially the MRAS signal appears strong which is due to a higher total protein load (stronger vinculin bands) which was confirmed by quantification. Immunoblotting for the downstream signaling proteins p44/p42 MAPK (ERK1/2) within the RAS-MAPK pathway in *LZTR1*-deficient iPSC-CMs resulted in poor and unreliable western blot signals (data not shown).

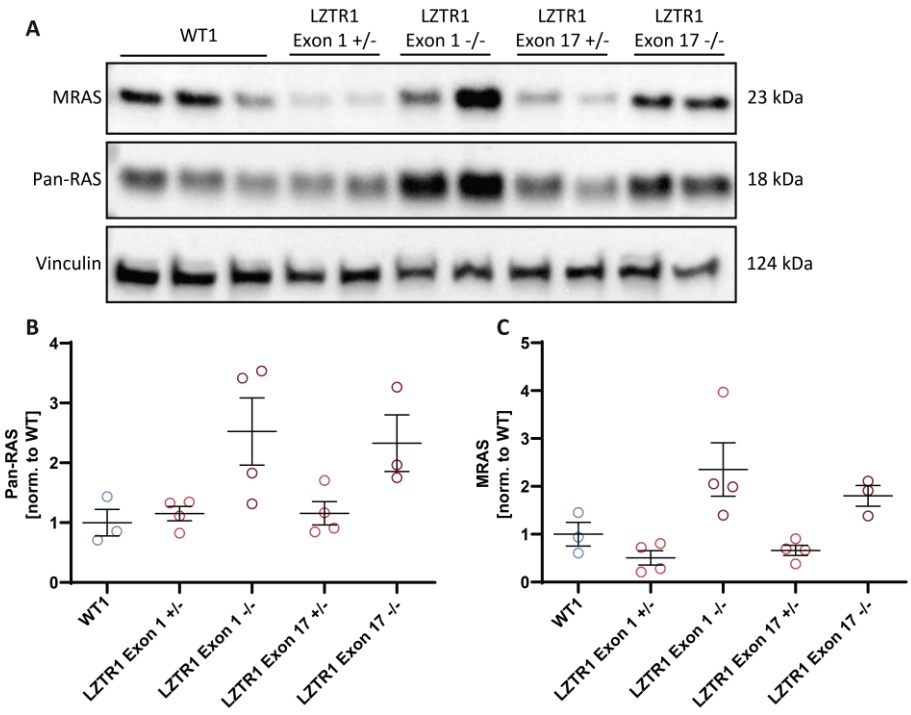

Figure 15: Heterozygous loss of *LZTR1* does not elevate RAS protein levels in iPSC-CMs

A, Representative images of western blot analysis of pan-RAS and MRAS protein levels in unstimulated WT and *LZTR1*-KO iPSC-CMs at day 60-79. 3 independent differentiations of WT1 and 4 independent differentiations of each *LZTR1*-KO iPSC-CMs were analyzed in total. Quantitative analysis of all assessed samples. Data suggests that **B,** Pan-RAS and **C,** MRAS are upregulated when compared to controls, although no significant differences could be determined due to variances of differentiations within the same cell lines. Data were normalized to vinculin expression and isogenic WT controls. Data are presented as mean±SEM. Determined by one-way ANOVA test.

Treatment of cell cultures with FGF for short periods of time enhances the RAS-MAPK signaling pathway and is a commonly used method to facilitate immunoblots for ERK and pERK. To enhance pathway activity, iPSC-CM cultures were treated with 10 ng/ml FGF for 10 min before lysis. Protein samples of these cells were immunoblotted for MRAS, pan-RAS as well as for ERK and pERK (Figure 16A).

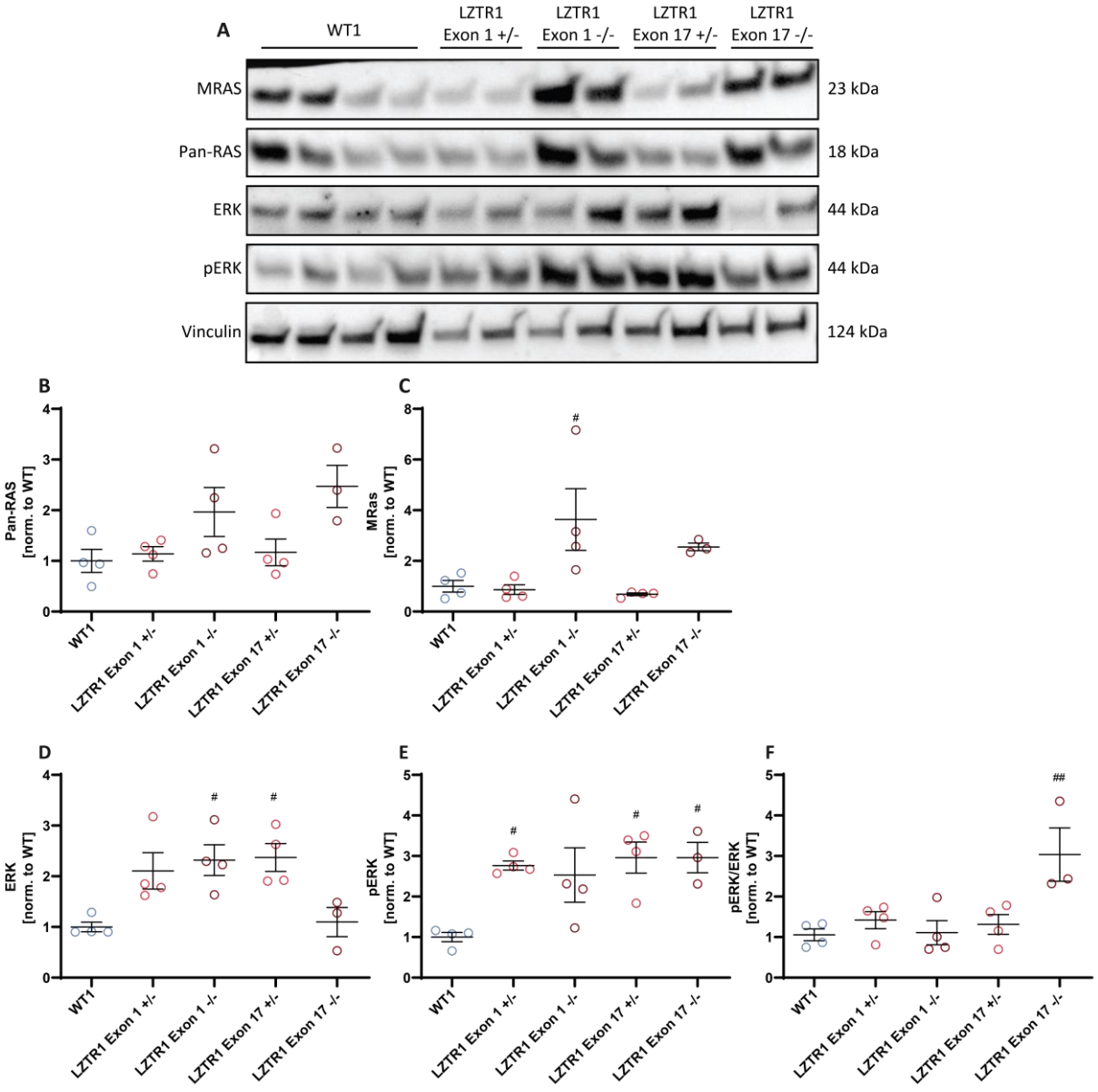

Figure 16: ERK and pERK protein levels are elevated in *LZTR1*-deficient iPSC-CMs after FGF stimulation

A, Analysis of RAS-MAPK signaling activity in FGF stimulated WT and indicated *LZTR1*-KO iPSC-CMs at day 60-79, assessed by western blot for pan-RAS, MRAS, phosphorylated MAPK (Thr202/Tyr204 of p44 MAPK and Thr185/Tyr187 of p42 MAPK), total MAPK and housekeeping protein vinculin. Shown are representative images. Four independent differentiations of WT iPSC-CMs and each *LZTR1*-KO iPSC-CMs were analyzed. **B-F:** Quantitative analysis of **B,** Pan-RAS, **C,** MRAS, **D,** total ERK, **E,** pERK and **F,** Overall ratio of phosphorylated to total ERK expression. Data were normalized to vinculin expression and WT. Data are presented as mean±SEM. #P<0.05, ##P<0.01, determined by one-way ANOVA test. # indicate significance to WT control.

Total ERK and pERK levels were elevated in all *LZTR1*-KO iPSC CM models (except for LZTR1 Exon 17 -/-). Although the pERK/ERK ratio was not significantly changed in all LZTR1-KO models, increased levels of both, total ERK and pERK suggest a higher RAS-MAPK pathway activity. This effect was also observed for both *LZTR1* +/- cultures, although protein levels of MRAS and pan-RAS were not elevated in these samples. The previously shown elevated protein levels of MRAS and pan-RAS in *LZTR1* -/- iPSC-CMs were reproducible in the FGF stimulated samples.

4.5.2 MRAS protein levels are elevated in *LZTR1*-KO iPSC-CMs

To further validate the results of elevated pan-RAS and MRAS protein levels in iPSC-CMs with biallelic *LZTR1* loss, we generated two additional iPSC lines with compound heterozygous KO in exon 1 (LZTR1-Exon1 -/- B; LZTR1-Exon1 -/- C) in an independent cell line (WT2). Protein lysates from iPSC-CMs generated of these cells were immunoblotted for endogenous pan-RAS and MRAS (Figure 17A). Quantification revealed that MRAS levels were significantly elevated in both KO lines compared to isogenic controls (Figure 17F). Results for pan-RAS also suggested a trend for higher protein levels in the KO lines, but no significant differences were determined due to fluctuations of differentiations within one cell line (Figure 17A). It is to note that the pan-RAS antibody does detect the NRAS, HRAS and KRAS isoform but not MRAS (sup. Figure 40), indicating that other RAS isoforms besides MRAS might be influenced by *LZTR1* loss.

Further, RAS-MAPK signaling is also known to be involved in cross-talk with other pathways such as PI3K-Akt signaling in cardiac hypertrophy (Mutlak and Kehat 2015). To investigate whether *LZTR1* loss leads to altered activity of this pathways, protein lysates were immunoblotted for endogenous key players of the PI3K-Akt pathway. It was shown before that AKT signaling activity is not significantly changed in iPSC-CMs derived from NS patients (II_1 and II_2) (Hanses et al. 2020). However, in the CRISPR/Cas9 mediated *LZTR1*-KO edited cell system total AKT levels were not significantly changed, while pAKT protein levels and the AKT/pAKT ratio were elevated in Exon1 -/- B but not in Exon1 -/- C when compared to isogenic controls.

For a higher statistical power, western blot results from comparable conditions (2 WT, 4 homozygous and 2 heterozygous *LZTR1*-deficient cell lines) were pooled for analysis (Figure 18). In iPSC-CMs with biallelic *LZTR1* loss, levels of pan-RAS (Figure 18A) and MRAS (Figure

18B) were significantly elevated, while iPSC-CMs with heterozygous *LZTR1* loss were not changed compared to isogenic controls.

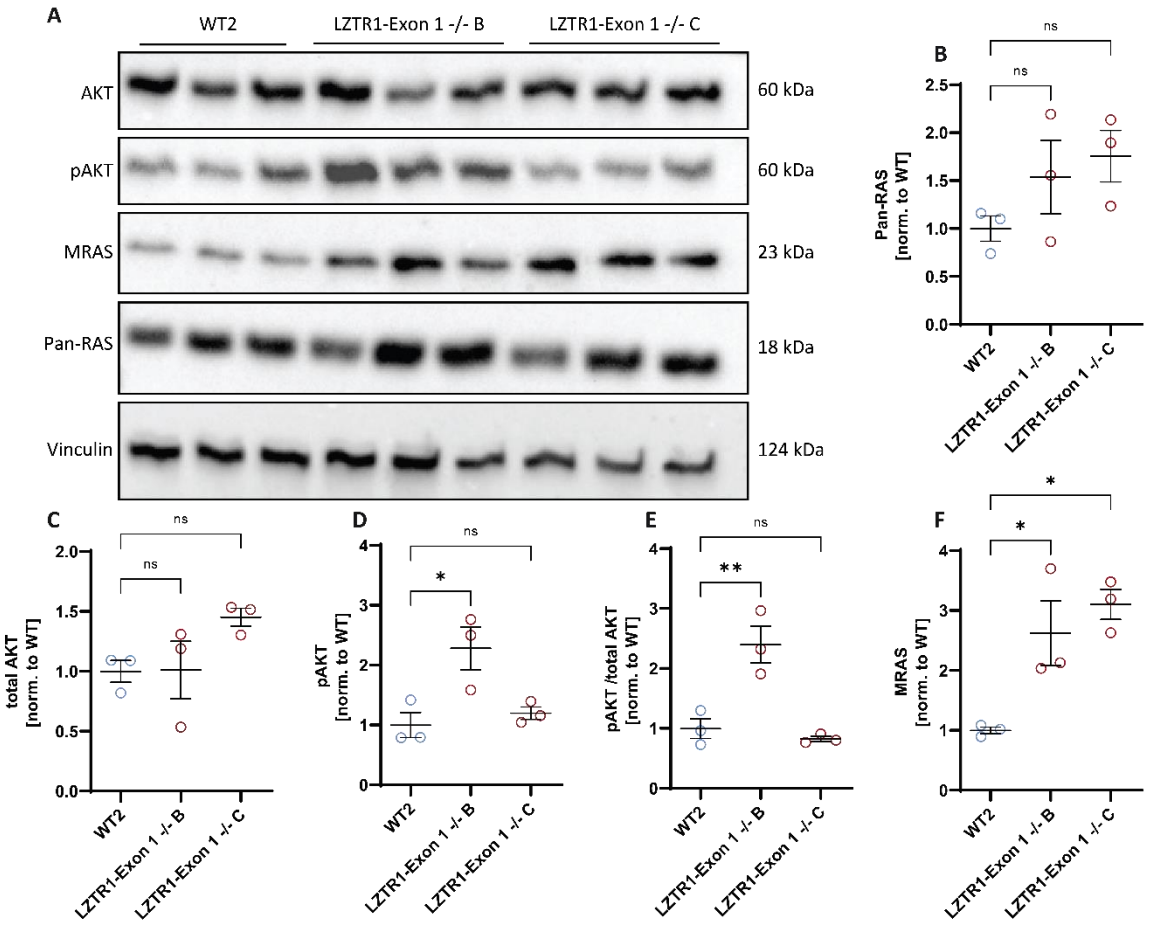

Figure 17: RAS protein levels are elevated in *LZTR1*-deficient iPSC-CMs

A, Analysis of RAS-MAPK and AKT signaling activity in unstimulated WT and indicated *LZTR1*-KO iPSC-CMs at day 60-89, assessed by western blot for pan-RAS and MRAS, and housekeeping protein vinculin. Three independent differentiations of WT iPSC-CMs and each *LZTR1*-KO iPSC-CMs were analyzed. **B-F,** Quantitative analysis of **B,** pan-RAS, **C,** total AKT, **D,** pAKT, **E,** Overall ratio of phosphorylated to total AKT expression and **F,** MRAS. Data were normalized to vinculin expression and WT. Data are presented as mean±SEM. *P<0.05, **P<0.01, ns, not significant. Determined by one-way ANOVA test.

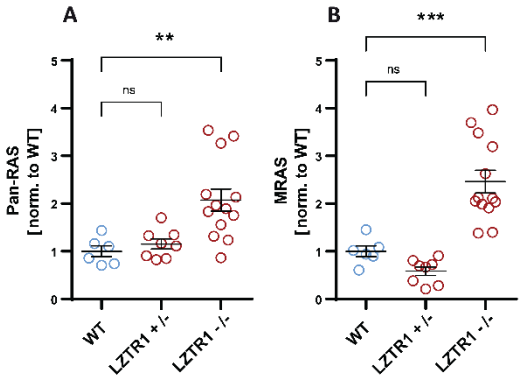

Figure 18: pan-Ras and MRAS levels are elevated in *LZTR1* -/- iPSC-CMs

Quantification of western blots from unstimulated iPSC-CMs at d60-89 immunoblotted for **A,** pan-RAS and **B,** MRAS showed a significant elevated protein levels in *LZTR1* -/- but not in *LZTR1* +/- iPSC-CMs. Both WT cell lines were pooled (WT1 and WT2), all 4 homozygous lines were pooled (LZTR1 Exon 1 -/-, LZTR1 Exon 1 -/- B, LZTR1 Exon 1 -/- C, LZTR1 Exon 17 -/-) and both heterozygous lines were pooled (LZTR1 Exon 1 +/-, LZTR1 Exon 17 +/-). Data were normalized to vinculin expression and isogenic WT controls. Data are presented as mean±SEM. Determined by one-way ANOVA test. *P<0.05; **P<0.001; ns, not significant.

Taken together, we conclude that protein levels of pan-RAS and MRAS are elevated in iPSC-CMs with complete loss of *LZTR1*, while heterozygous loss had no significant influence. As immunoblots for phosphorylated members of the RAS-MAPK or PI3K-Akt pathway in iPSC-CMs resulted in unsteady signals and might be an inappropriate readout in these cell types.

4.6 Overexpression of *LZTR1* in iPSC-CMs

4.6.1 Truncated LZTR1 shows altered localization in iPSC-CMs

The intracellular localization of LZTR1 is under debate in the recent years and was mainly studied in HEK293T or HeLa cells systems. Localization studies in cardiac specific cells were not conducted so far. Since *LZTR1* loss is associated with a severe cardiac phenotype, we aimed to obtain deeper insights into the intracellular localization of LZTR1 in cardiac cells. In lack of antibodies that are capable to detect endogenous levels of LZTR1, the overexpression constructs previously established in HEK293T cells (Figure 8) were used for overexpression in iPSC-CMs. Based on Lipofectamine, WT-iPSC-CMs (WT1) were transfected with constructs coding for either the full-length or truncated LZTR1 variant which introduces an artificial stop codon in exon 17. Additionally, both constructs carry an N-terminal HA protein tag. Concordant with the results from the HEK293T cell experiments, the intracellular localization of WT-LZTR1

appeared in a clearly spotted pattern when immunostained for HA (Figure 19A). In contrast, the localization of the mut-LZTR1 variant is strikingly different. The spotted pattern is lost and LZTR1 is homogenously distributed throughout the whole cell (Figure 19B). This localization divergence caused by loss of function mutations in *LZTR1* was previously shown in HEK293T and HeLa cells (Bigenzahn et al. 2018; Steklov et al. 2018) and is reproducible in iPSC-CMs with the specific *LZTR1* variant that remodels the mutation of intron 16 of the paternal variant of the NS family case presented above. The overall LZTR1 signal strength from immunostainings of HA-mut-LZTR1 appeared higher when compared to HA-WT-LZTR1, in line with the results from western blots from overexpression in HEK293T cells showing strongly elevated levels of HA-mut-LZTR1 when compared to HA-WT-LZTR1 signals. This finding further fortifies the prediction that truncated LZTR1 accumulates in the cytoplasm.

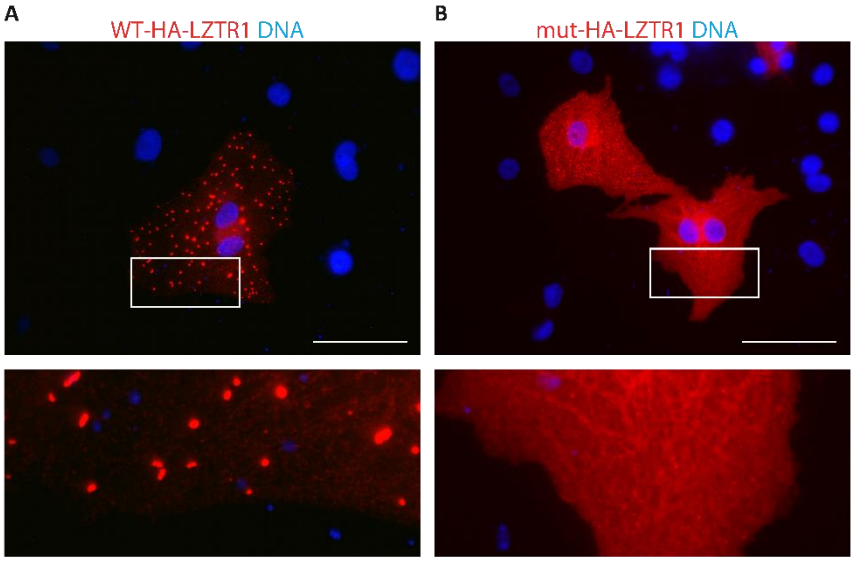

Figure 19: Truncated LZTR1 causes altered subcellular localization in iPSC-CMs

Representative images of WT-iPSC-CMs at d60 overexpressing either **A,** WT-HA-LZTR1 or **B,** mut-HA-LZTR1 via Lipofectamine. WT-LZTR1 is localized in a spotted manner while overexpressed truncated LZTR1 appears in an evenly distributed manner throughout the cytoplasm. Scale bar, 50 µm.

4.6.2 Full length LZTR1 co-localizes to RAS isoforms and CUL3

To evaluate potential co-localization of LZTR1 and RAS isoforms in iPSC-CMs, HA-tagged *LZTR1* constructs were co-overexpressed with one of three different FLAG-tagged constructs, coding for one RAS isoform each (MRAS, NRAS or HRAS). Immunostaining for HA and FLAG

resulted in a very similar pattern for all three RAS isoforms. Overexpressed MRAS showed a spotted pattern that co-localized with full-length LZTR1, indicated by the white arrowheads (Figure 20A). The spotted localization pattern was lost when MRAS was co-overexpressed with the truncated LZTR1 variant and both proteins were homogenously distributed in the cytoplasm (Figure 20B). The same effect was observed for NRAS (Figure 21A-B) and HRAS (Figure 22A-B). Quantitative analysis revealed a high level of co-localization of WT-LZTR1 and all three evaluated RAS variants. (MRAS mean= 0.75; NRAS mean= 0.75, HRAS mean= 0.79), determined by for Pearson's Correlation Coefficient (Figure 24).

CUL3 is part of the Cullin-RING E3 ubiquitin ligase complex and is described as a mediator of protein ubiquitination and proteasomal degradation for BTB-Kelch proteins (Furukawa et al. 2003; Geyer et al. 2003). Following the result of LZTR1 co-localizing with all three tested RAS isoforms, the potential co-localization of CUL3 was assessed in WT-iPSC-CMs. In a first step, only the MYC-CUL3 construct was overexpressed in iPSC-CMs (Figure 23A), presenting a mainly homogenous distribution within the cytoplasm of the cells. Co-overexpression of WT-HA-LZTR1 and MYC-CUL3 changed the subcellular localization of CUL3, which now mainly co-localized with LZTR1 (Figure 23B), showing the same spotted pattern that was observed for WT-LZTR1 before. Quantitative analysis revealed a high level of co-localization of WT-LZTR1 and CUL3 determined by for Pearson's Correlation Coefficient with a mean value of 0.85 (Figure 24). Notably, change of localization of MYC-CUL3 is less affected in cells with only weak WT-HA-LZTR1 overexpression. Co-overexpression of MYC-CUL3 and mut-HA-LZTR1 abolishes the observed change of localization of MYC-CUL3. As described above, mut-HA-LZTR1 loses the spotted pattern and is evenly distributed in the cytoplasm. The intracellular localization of MYC-CUL3 is not changed when co-overexpressed with mut-HA-LZTR1 (Figure 23C), compared to overexpression without LZTR1. Calculation of co-localization always requires a specific pattern in immunostaining. Homogenous distribution of two non-interaction proteins would result in a misleading high co-localization value. Therefore, co-localization of RAS or CUL3 with the truncated LZTR1 was not determined.

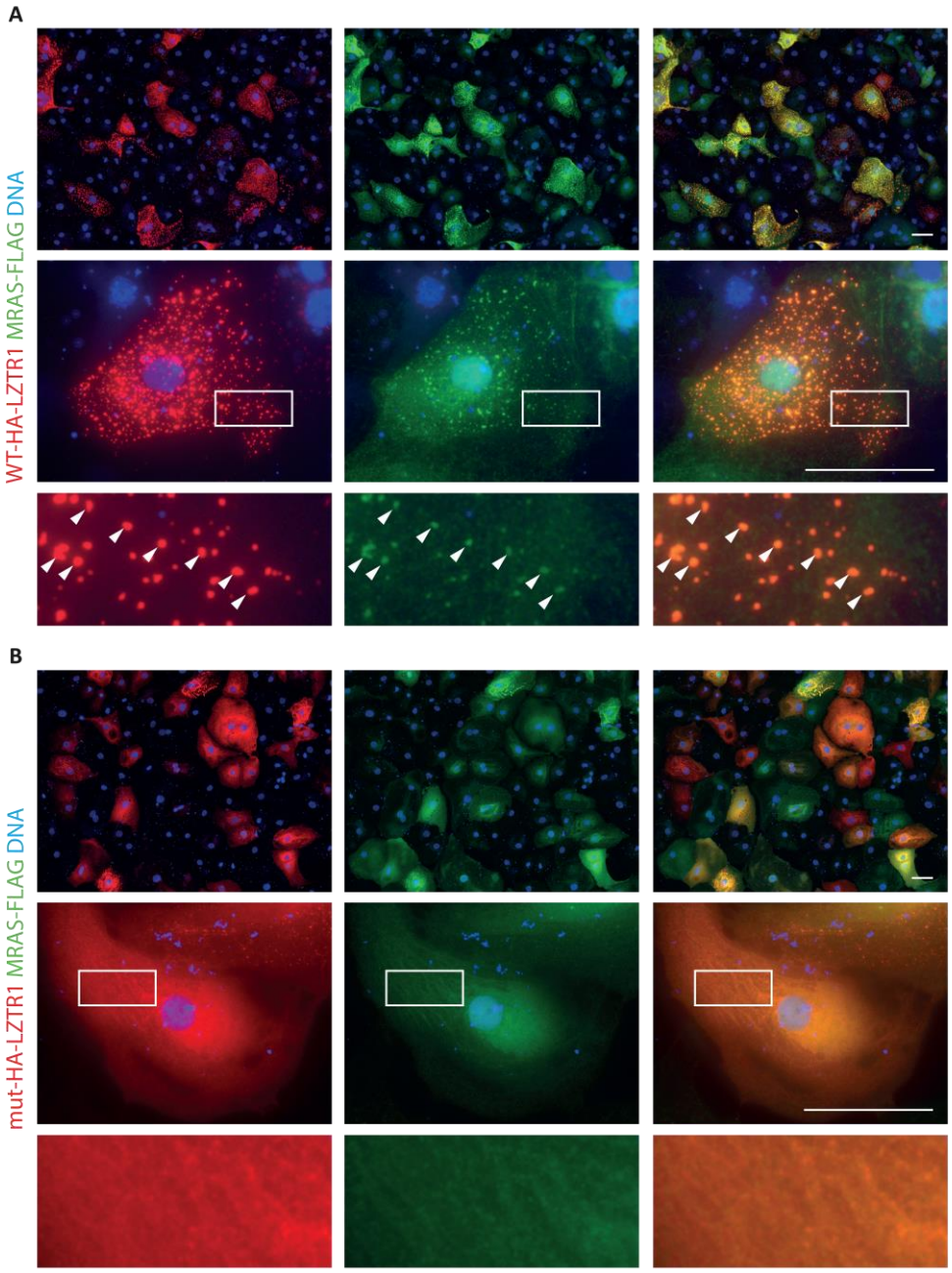

Figure 20: MRAS co-localizes with WT-LZTR1

Representative images of d60 WT-iPSC-CMs overexpressing the indicated constructs. **A,** Overexpression of MRAS-FLAG and WT-HA-LZTR1. The upper row shows an overview. Higher magnifications in middle and lower row reveal a co-localization of WT-HA-LZTR1 and MRAS-FLAG, indicated by white arrowheads. **B,** Overexpression of MRAS-FLAG and mut-HA-LZTR1 results in altered intracellular localization. Scale bar= 50 µm.

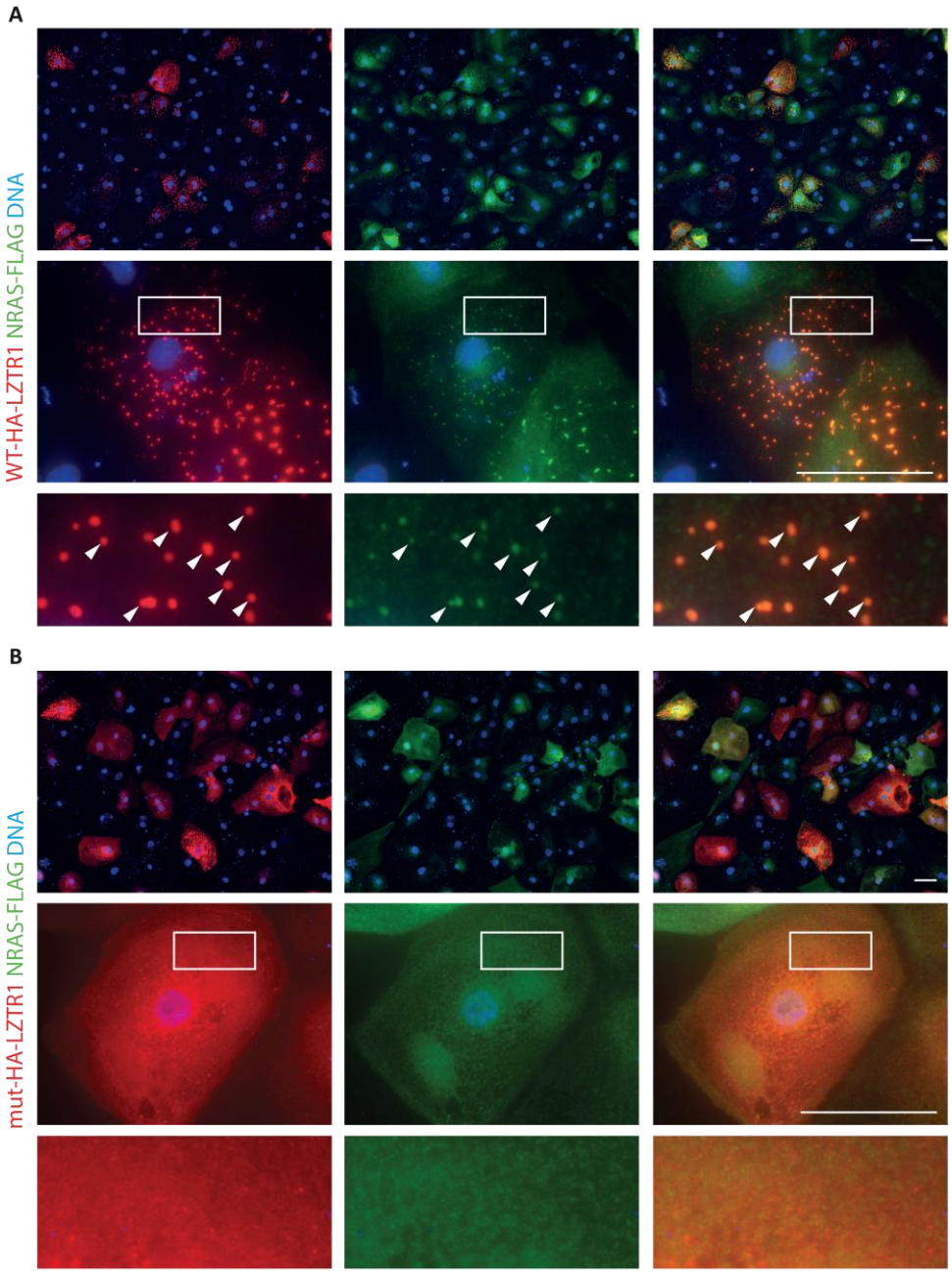

Figure 21: NRAS co-localizes with WT-LZTR1

Representative images of d60 WT-iPSC-CMs overexpressing the indicated constructs. **A,** Overexpression of NRAS-FLAG and WT-HA-LZTR1. The upper row shows an overview. Higher magnifications in middle and lower row reveal a co-localization of WT-HA-LZTR1 and NRAS-FLAG, indicated by white arrowheads. **B,** Overexpression of NRAS-FLAG and mut-HA-LZTR1 results in altered intracellular localization. Scale bar= 50 µm.

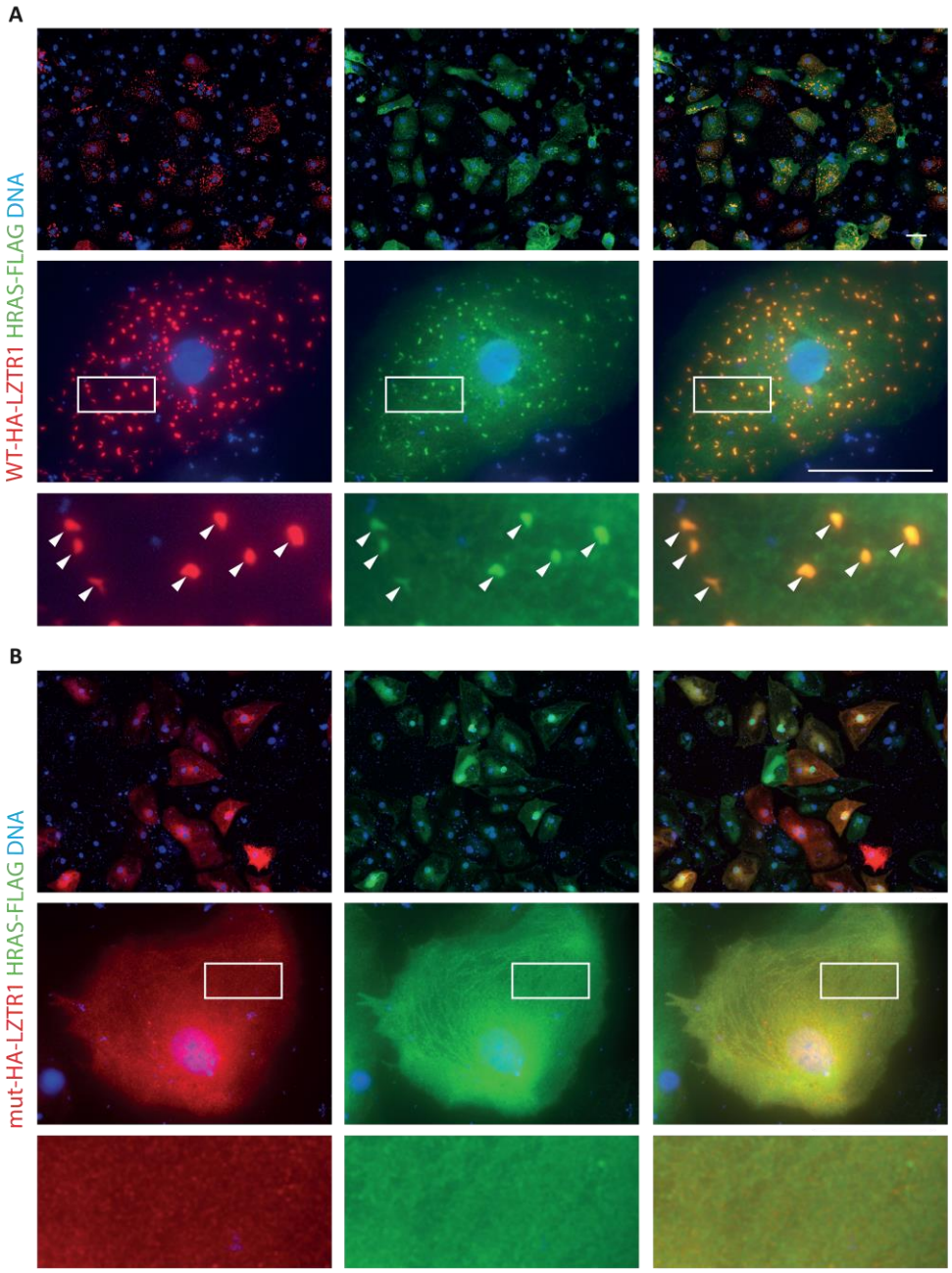

Figure 22: HRAS co-localizes with WT-LZTR1

Representative images of d60 WT-iPSC-CMs overexpressing the indicated construct. **A,** Overexpression of HRAS-FLAG and WT-HA-LZTR1. The upper row shows an overview. Higher magnifications in middle and lower row reveal a co-localization of WT-HA-LZTR1 and HRAS-FLAG, indicated by white arrowheads. **B,** Overexpression of HRAS-FLAG and mut-HA-LZTR1 results in altered intracellular localization. Scale bar= 50 µm.

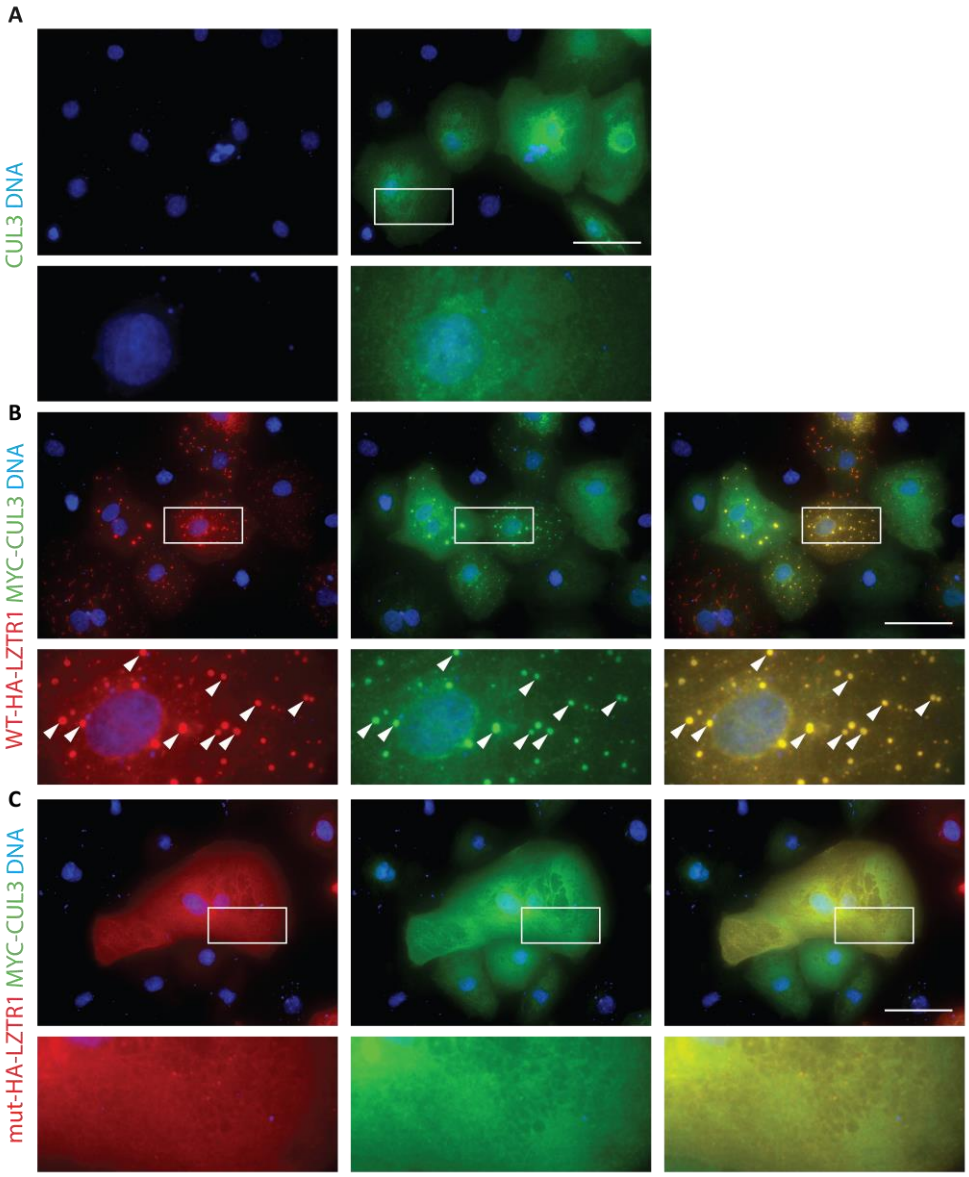

Figure 23: WT-HA-LZTR1 co-localizes with CUL3

Representative images of WT-iPSC-CMs at d53 overexpressing WT-HA-LZTR1 or mut-HA-LZTR1 and MYC-CUL3. **A,** Overexpression of MYC-CUL3. **B,** Co-overexpression WT-HA-LZTR1 and MYC-CUL3 reveals the co-localization indicated by white arrowheads. **C,** Co-overexpression of mut-HA-LZTR1 and MYC-CUL3. Scale bar= 50 µm.

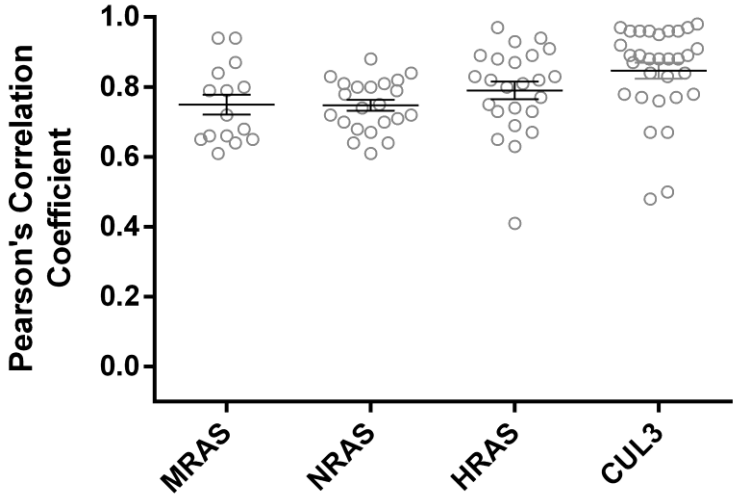

Figure 24: Quantified co-localization of LZTR1 with RAS and CUL3

Quantification of co-localization of WT-HA-LZTR1 overexpressed in WT iPSC-CMs with FLAG-tagged RAS variants or MYC-tagged CUL3. Assessed by Pearson´s Correlation Coefficient with n= 15-31, where n is the number of analyzed cells per condition. Data are presented as mean ±SEM.

4.6.3 Presence of truncated LZTR1 causes localization change of RAS isoforms

When the RAS isoforms are overexpressed in iPSC-CMs, the subcellular localization appears in two different forms, either in the spotted pattern or evenly distributed in the cytosol. Depending on the RAS isoforms, the ratios of these forms were different. When only RAS is overexpressed, the spotted pattern was observed in 59% of iPSC-CMs for MRAS, 43% for NRAS and 81% for HRAS (Figure 25). This distribution is not significantly changed when WT-HA-LZTR1 is co-overexpressed, with the spotted pattern present in 63% of cells transfected with MRAS, 58% in NRAS and 86% in HRAS. In contrast, the presence of mut-HA-LZTR1 led to a shift of this distribution towards the cytosolic form, with the highest impact on NRAS and HRAS which showed the spotted pattern in only 2% and 0% of counted cells, respectively. MRAS was affected to a lesser extend with 36% of cells that showed the spotted pattern when co-overexpressed with the truncated LZTR1 variant.

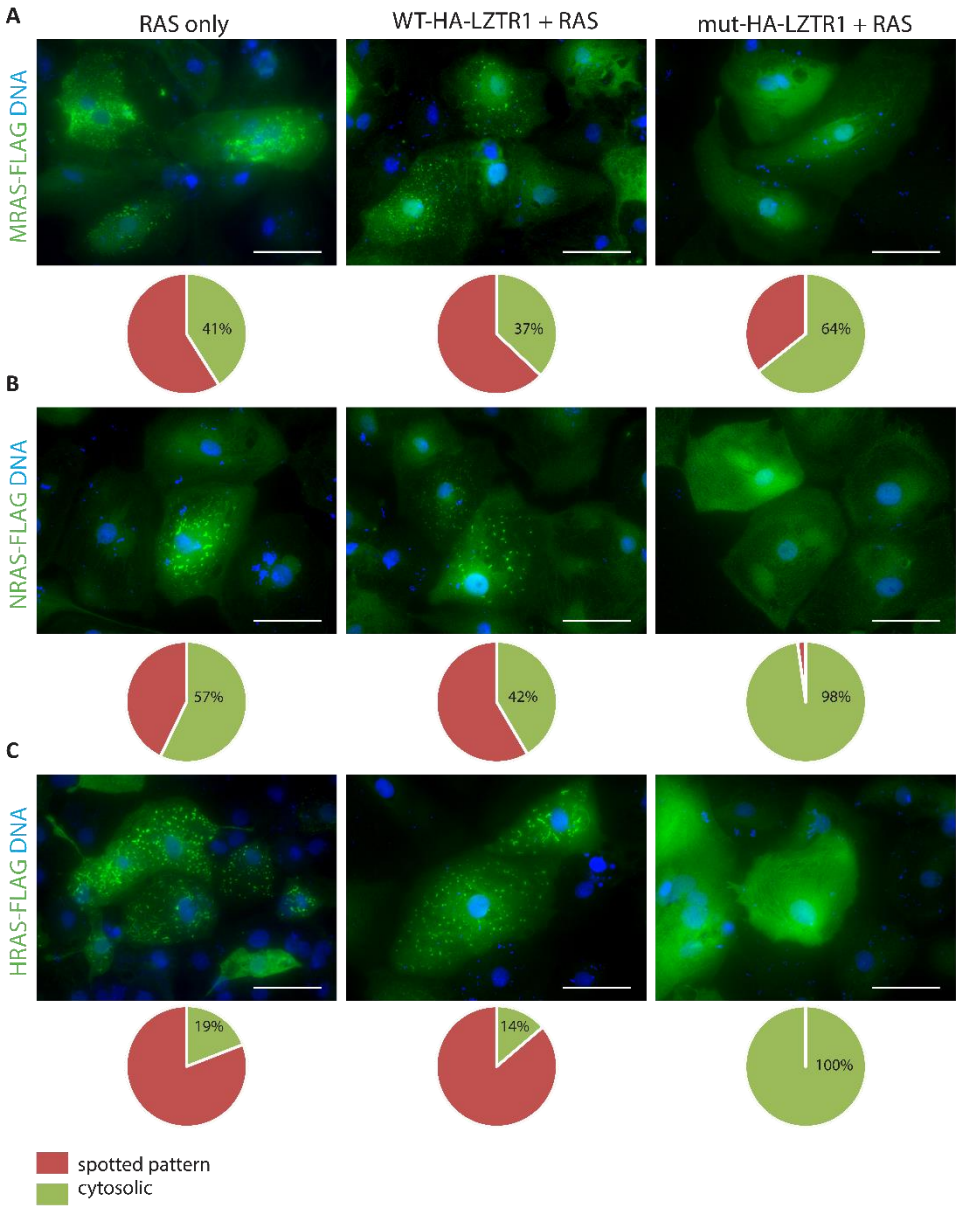

Figure 25: Overexpression of truncated LZTR1 changes intracellular RAS localization

Representative images of WT iPSC-CMs at d60 overexpressing HA-WT-LZTR1 or HA-mut-LZTR1 and **A,** MRAS **B,** NRAS or **C,** HRAS with pie charts below, showing the percentage of cells showing a spotted pattern (red) or cytosolic (green) localization of RAS. n= 30-80, where n is the number of analyzed cells per condition. Scale bar= 50 µm.

4.7 LZTR1 does not co-localize with peroxisomes or lysosomes

The overserved pattern of overexpressed LZTR1, RAS, and CUL3 suggests an accumulation of this complex at small cell compartments such as peroxisomes, endosomes, or lysosomes. To test if LZTR1 localizes to these compartments, HA-WT-LZTR1 was overexpressed in WT-iPSC-CMs and cells were immunostained for the peroxisomal marker Peroxisomal membrane protein PEX14 (PEX14) (Figure 26A). Although the localization of peroxisomes in iPSC-CMs appeared comparable to the LZTR1-positive vesicle like structures, no relevant overlapping was observed. This was confirmed by automated analysis for Pearson's Correlation Coefficient, showing a poor co-localization score with LZTR1 (mean= 0.26). Further, Lysosomal-associated membrane protein 1 (LAMP1) was immunostained as a marker for late endosomes and lysosomes (Figure 26B), but also showed no relevant co-localization with LZTR1 (mean= 0.32). The co-localization of α-actinin and LZTR1 was determined as a negative control (Images not shown). Additional immunostainings for the early endosome makers Ras-related protein Rab-5A (RAB5) and Early Endosome Antigen 1 (EEA1) and the recycling endosome marker Ras-related protein Rab-11A (RAB11) resulted in unspecific signals and non-meaningful results and could not be used for analysis of possible co-localization with LZTR1 (data not shown).

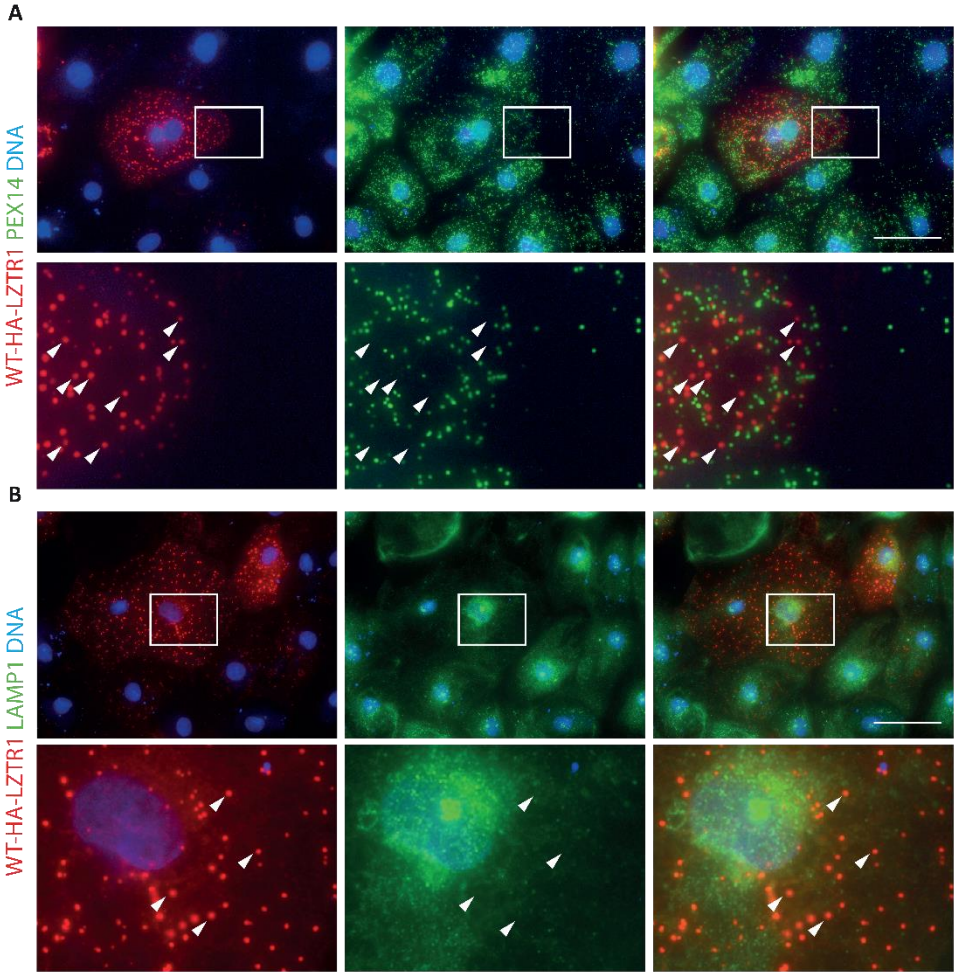

Figure 26: LZTR1 is not localized at peroxisomes or lysosomes

WT-iPSC-CMs transiently overexpressing full-length HA-tagged LZTR1 were immunostained for endogenous **A,** PEX14 as a peroxisomal marker or **B,** LAMP1 as a marker for late endosomes and lysosomes. A co-localization with LZTR1 was not observed for both proteins. Scale bar= 50 µm.

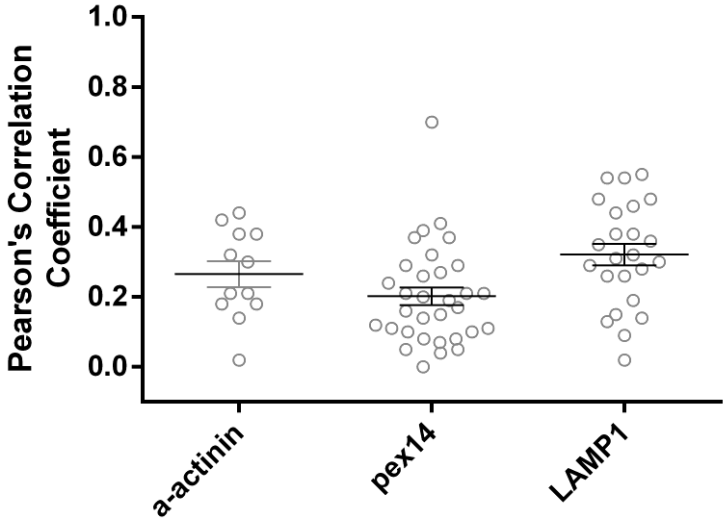

Figure 27: Quantified co-localization of LZTR1 with peroxisomes and lysosomes

Quantification of co-localization of WT-HA-LZTR1 overexpressed in WT iPSC-CMs with FLAG-tagged RAS variants, peroxisomal and lysosomal markers. Assessed by Pearson´s Correlation Coefficient with n= 12-32, where n is the number of analyzed cells per condition. Data are presented as mean ±SEM.

4.8 *LZTR1*-deficient iPSC-CMs show altered calcium handling characteristics

A normal calcium homeostasis within cardiomyocytes is an important determinant of myocardial contractility and calcium dysregulation is associated with cardiac diseases. On single cell level, myocytes from failing hearts exhibit an increased overall calcium leak and calcium transients (CaTs) with a reduced amplitude (Hoang-Trong et al. 2015). The elevated calcium leak is caused by increased occurrence of spontaneous diastolic calcium releases via the ryanodine receptor from the sarcoplasmic reticulum, known as calcium sparks (Cheng et al. 1993) and are described to prolong the calcium transients (Fowler et al. 2020). Our previous study showed that calcium handling genes are higher expressed in NS-patient derived iPSC-CMs and that calcium transients in these cells show abnormal characteristics (Hanses et al. 2020). Driven by this finding, iPSC-CMs between d68-89 were stained with Fluo-4 AM for recording of CaTs and cytosolic calcium sparks in *LZTR1*-deficient iPSC-CM lines (LZTR1-Exon 1 -/- B and LZTR1-Exon 1 -/- C) and isogenic controls (WT2) by confocal line scanning. The cells were paced at 0.25 Hz with 18 V and a 3 ms stimulus duration. Representative 3D surface plots and the corresponding original recordings at basal conditions and after treatment with 100 nM verapamil, an L-type calcium channel blocker are displayed in Figure 28A. The

diastolic area analyzed for spontaneous calcium sparks measured 1 second with a width of 40 µm. Quantification of the overall SR calcium leak (including the parameters amplitude, width, and duration of single sparks) revealed a slight but nonsignificant increased tendency in *LZTR1*-deficient iPSC-CMs. Treatment with verapamil significantly reduced the SR calcium leak compared to basal conditions in all cell lines (Figure 28B).

The calcium transients of *LZTR1*-deficient iPSC-CMs were prolonged compared to isogenic controls. Representative plots of calcium traces with the corresponding original recordings of calcium transients are shown in Figure 28C. Quantification confirmed the significantly increased CaT rise time in LZTR1-Exon 1 -/- B but not in LZTR1-Exon 1 -/- C compared to isogenic controls (Figure 28D). However, the duration of CaTs at 50% decay of both *LZTR1*-KO iPSC-CM lines were prolonged when compared to isogenic control, which resulted in extended overall transients in both *LZTR1*-deficient cell lines (Figure 28E). Administration of 100 nM verapamil reduced the rise time for all cell lines, thereby aligning the CaT rise time of LZTR1-Exon 1 -/- B to the level of the untreated WT. Further, verapamil also reduced the CaT decay 50 values, normalized to the level of untreated control iPSC-CMs. Additionally, the amplitude [F/F0] of CaTs was significantly reduced in *LZTR1*-KO iPSC-CMs compared to control. Additionally, verapamil treatment reduced the CaT amplitude in all cell lines. (Figure 28F). Taken together, *LZTR1*-KO iPSC-CMs showed a phenotype with an overall higher duration and reduced amplitude of CaTs which was partially rescued by verapamil treatment.

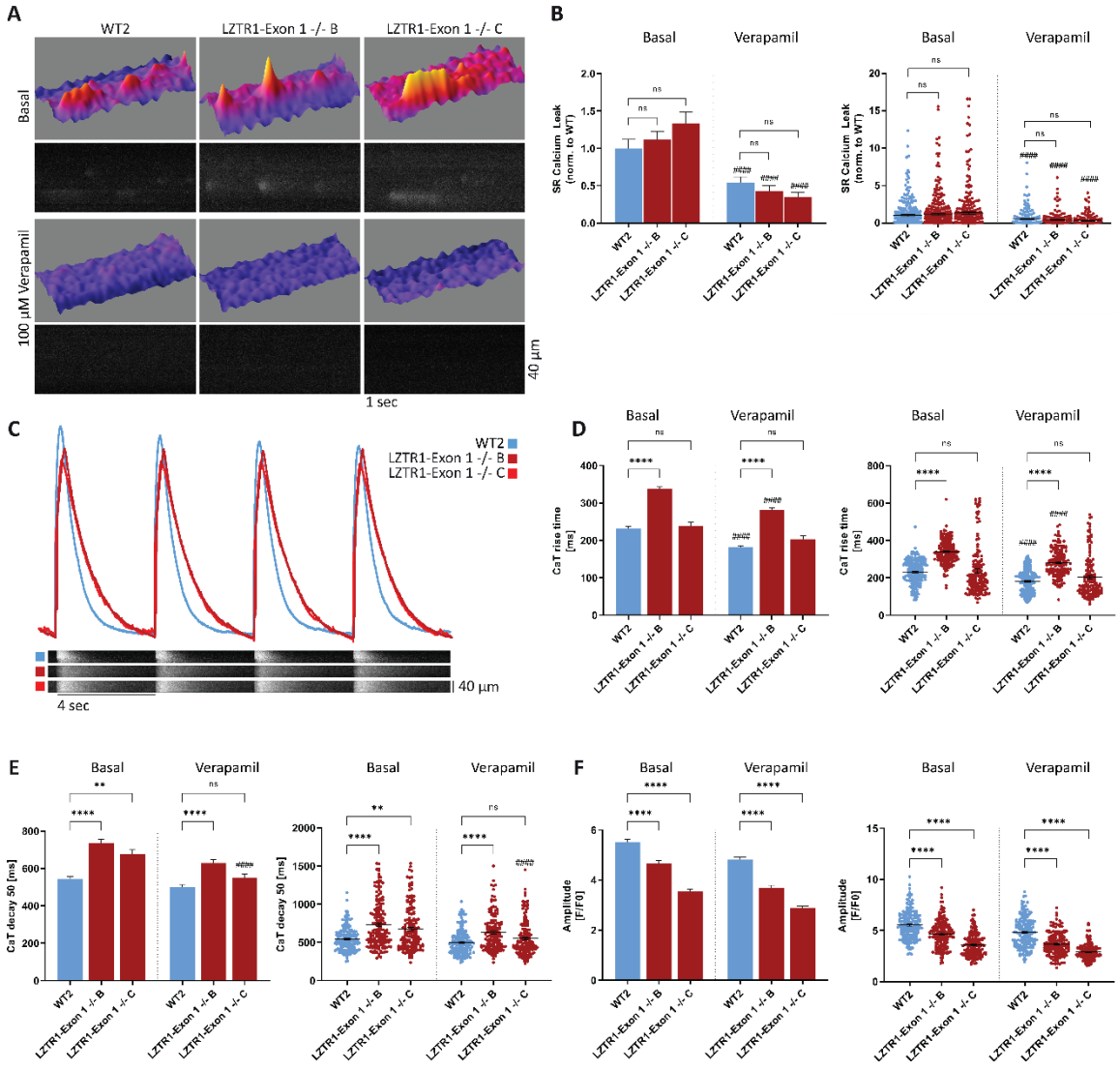

Figure 28: *LZTR1*-deficient cardiomyocytes show altered calcium handling characteristics

For calcium tracing in live cells, iPSC-CMs at days 68 to 89 were stained with calcium indicator Fluo-4 AM, paced at 0.25 Hz (3 ms stimulus, 20 V) and analyzed via confocal imaging under basal conditions and after administration of 100 nmol/L verapamil (for WT2: basal: n= 180 cells, verapamil: n= 180 cells, 3 independent differentiations; for LZTR1-Exon 1 -/- B: basal: n= 180 cells, verapamil: n=155 cells, 3 independent differentiations; for LZTR1-Exon 1 -/- C: basal: n=160 cells, verapamil: n=159 cells, 3 independent differentiations. **A,** Representative 3D surface plots of diastolic calcium sparks of indicated iPSC-CM lines with the corresponding original recordings below. **B,** Quantitative analysis of overall diastolic calcium leak of indicated WT and *LZTR1*-deficient iPSC-CM lines at basal conditions and after treatment with verapamil, displayed as bar graphs and dot plots. **C,** Representative plots of calcium transients (CaTs) of the indicated iPSC-CM lines with the corresponding original recordings below. Quantitative analysis of **D,** CaT rise time and **E,** CaT decay at 50%. Data are presented as mean±SEM. ns= not significant; **= P<0.01; ****/####= P<0.0001 by nonparametric Kruskal-Wallis test with Dunn correction. # indicates significance to basal condition.

4.9 Cell size measurements in *LZTR1*-deficient iPSC-CMs

In order to investigate whether *LZTR1*-deficient iPSC CMs recapitulate the hypertrophic cardiac phenotype of NS patients, the cell diameter of iPSC-CMs were measured in suspension with the CASY cell counter system For the cell lines LZTR1 Exon 1 +/-, LZTR1 Exon 1 -/-, LZTR1 Exon 17 +/- and LZTR1 Exon 17 -/-, no significant difference in cell size compared to their corresponding WT line (WT1) could be measured. Further, both *LZTR1*-deficient cell lines generated from WT2 (LZTR1-Exon 1 -/- B, LZTR1-Exon 1 -/- C) showed no significant differences compared to their isogenic control line in cell diameter in CASY measurements (Figure 29A).

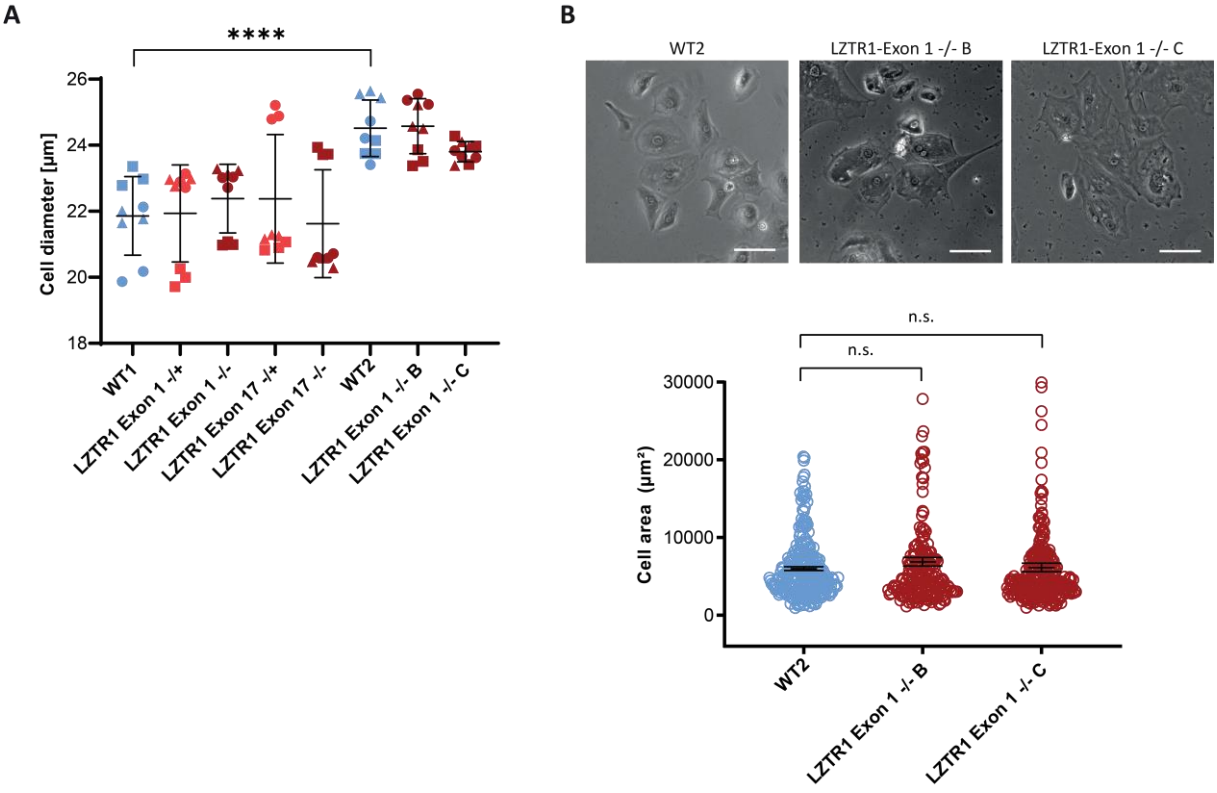

Figure 29: Cell size analysis

A, Quantitative analysis of cell diameter in suspension of singularized WT and indicated *LZTR1*-KO iPSC-CMs. Cell size measurements were obtained from WT and *LZTR1*-KO-iPSC-CM cultures between days 60 to 82, plated in densities of 6580 CMs/cm² (25.000 CMs/ 12well). Measurements were obtained with CASY cell counter system. 3 independent differentiations per cell line. **B,** Quantitative analysis of cell area in adherent iPSC-CM cultures. Cell size measurements were obtained from WT and *LZTR1*-KO-iPSC-CM cultures between days 60 to 82. 3 independent differentiations per cell line. Total cells assessed: 188-267 cells per cell line. Individual differentiations are indicated by symbols: triangle, circle and square. Data are presented as mean±SEM. n.s., not significant. Determined by nonparametric Mann-Whitney test. *P<0.05, **P<0.01, ****P<0.0001. Scale bar: 20 µm.

All cell lines showed a strong tendency for clustering of cell sizes within one differentiation. Measured differences between individual differentiations (indicated by symbols: square, circle, triangle) within one cell line were greater than the differences between the cell lines. It is to note that the two different WT lines showed significant differences in cell sizes which are recapitulated by their associated *LZTR1*-deficient cells lines, underlining the importance of isogenic controls. Cell areas of both *LZTR1*-deficient iPSC-CM lines based on WT2 were further assessed in adherent cultures. iPSC-CMs were seeded in low densities (Figure 29B) and cell areas were measured manually but no significant differences were detected compared to isogenic controls (Figure 29C).

4.10 Electrophysiological analysis of *LZTR1*-deficient iPSC-CMs

Multi electrode array (MEA) is a method that allows to investigate the electrophysiological properties of iPSC-CMs. The field potential (FP) comprises the spatiotemporal electrical activity of adherent cells measured by electrodes in the culture dish. The FP is formed by the spreading cardiac action potential throughout the cells relative to the recording electrodes and is comparable to clinical echocardiograms (Yamamoto et al. 2016; Kussauer et al. 2019). To assess whether *LZTR1* loss causes a change of these electrophysiological properties, the FPs of spontaneously beating iPSC-CMs were measured using the Maestro PRO MEA platform.

The recorded field potential duration (FPD) was normalized to beat rate via Fridericia correction (FPDc). FPDc values for all iPSC-CM lines showed a strong tendency for clustering between differentiations of individual cell lines and no significant differences were detected except for LZTR1 Exon 1 +/-, which also showed only little variability between the three independent differentiations (Figure 30A). The Conduction velocity (CV) and the contraction amplitude were reduced in all *LZTR1*-deficient cell lines compared to WT (Figure 30B-C). A high degree of beat regularity was observed in all recorded iPSC-CMs lines with even lower beat-to-beat variability in the *LZTR1*-deficient cell lines compared to the isogenic control line (Figure 30D).

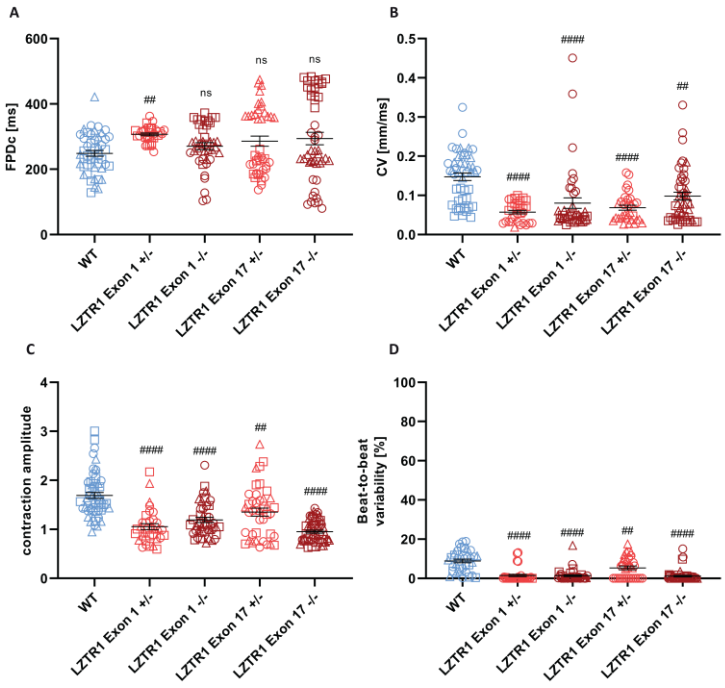

Figure 30: *LZTR1*-KO iPSC-CMs show altered electrophysiological parameters

Contraction and field potential parameters of iPSC-CM cultures at days 65 to 82 were analyzed via multielectrode array. **A,** Analysis of FPDc, normalized to beat rate by Fridericia correction. **B**, Conduction velocity. **C,** Analysis of contraction amplitude by impedance change. **D,** Beat-to-beat variability For WT cell line: 3 independent differentiations, 6 technical replicates per differentiation. For *LZTR1*-deficient cell lines: 4 independent differentiations with 6 technical replicates per differentiation. Samples were measured 3 times within one week and results of measurements were pooled. Data are presented as mean±SEM. ##*P*<0.01, ####*P*<0.0001 by nonparametric Kruskal-Wallis test. # indicates significance to WT. CV, conduction velocity; FPDc, corrected field potential duration.

5 Discussion

5.1 *LZTR1*-deficient iPSC-CMs as a model system for NS and its limitations

iPSCs are extensively used to model human diseases. Especially iPSC-CMs are well suited to model cardiac diseases as they are capable to recapitulate pathogenic phenotypes of the donors for many diseases such as long-QT syndrome (Moretti et al. 2010), catecholaminergic polymorphic ventricular tachycardia (Itzhaki et al. 2012; Kujala et al. 2012), or cardiomyopathies such as HCM (Lan et al. 2013) or dilated cardiomyopathy (Sun et al. 2012). For NS, four patient specific iPSC-CM models were reported so far, one generated from our group. Interestingly, they are based on mutations in different genes, *MRAS* (Higgins et al. 2019), *RAF1* (Sakai et al. 2018; Jaffré et al. 2019), and *LZTR1* (Hanses et al. 2020).

Although causative mutations in *LZTR1* were reported to cause NS in 2015 (Yamamoto et al. 2015), the role of *LZTR1* was not revealed until 2018 (Steklov et al. 2018; Bigenzahn et al. 2018). Most of these results were gathered from experiments conducted in HEK293T and HeLa cell systems, which are indeed a great and easy to handle experimental platform that led to fundamental findings of the RAS-MAPK regulation mediated by LZTR1. However, these cell systems were mainly based on transient overexpression. As a major drawback, these cells are not capable to model the disease in a more realistic setting to investigate functional parameters in physiological settings. Particularly, the influence of elevated RAS activity on development of HCM and other cardiac dysfunctions cannot be investigated in HEK293T cells. In contrast, mouse models have the advantage to display the effects of mutations on the whole organism and are capable to reveal phenotypes that are not present in cell cultures. However, this murine system is not optimal either because unlike in humans, homozygous depletion of *Lztr1* in mice is prenatally lethal (Dickinson et al. 2016; Steklov et al. 2018). On the other hand, mice with heterozygous loss of *Lztr1* are viable and are described to develop a NS-like phenotype including facial abnormalities and cardiac phenotype with hypertrophic CMs (Steklov et al. 2018). In humans, heterozygous loss of *LZTR1* does not necessarily lead to NS (Johnston et al. 2018; Hanses et al. 2020). Moreover, isolated MEFs of embryonic *Lztr1* -/- and *Lztr1* +/- mice did not show elevated protein levels of HRAS and KRAS, which was reported in two independent publications (Steklov et al. 2018; Castel et al. 2019). Taken together, this might indicate that murine and human variants of LZTR1 are not functionally identical to full extend and conclusions drawn from these models might be limited.

To close this gap, iPSCs offer the possibility to model NS based on *LZTR1* mutations in a versatile human system. To my best knowledge, our group is the only one that generated an iPSC-CMs based model system for NS that is caused by pathogenic LZTR1 variants, either by directly reprogramming fibroblasts from NS patients into iPSCs or by CRISPR/Cas9 based genome editing to introduce *LZTR1* mutations into WT iPSCs. Another advantage of iPSCs is their capability of being differentiated into other cell types such as cardiomyocytes, cardiac fibroblasts, or neuronal cell types for possible future studies. As a multisystemic disorder, NS affects several organs and in a novel approach, it was reported that cerebral organoids differentiated from iPSCs that were generated from NS patients with a mutation in *PTPN11* displayed aberrant neural development (Ju et al. 2020). These studies have proven that iPSCs are well suited as an *in vitro* platform to model NS based on *LZTR1* loss or other causative genetic defects as they are capable to recapitulate the patient's phenotypes. They are applicable for patient specific approaches that cannot be provided by HEK293T cells or murine systems. Further, iPSCs offer fast growing methodologies and easy readouts for drug screening studies or serve a platform to test CRISPR/Cas9 based genomic repair strategies (Hanses et al. 2020) that could be used as a future treatment for NS.

Besides all the advantages that come with iPSC-CMs in disease modeling over animal models, they have their limitations. Although not as resource demanding as animal models, iPSC-CMs are cost and time intensive which impedes the usage of large sample numbers. Since independent differentiations from the same cell line can exhibit divergent physiological properties, appropriate numbers of replicates and proper controls are crucial to generate meaningful results. It is commonly accepted that iPSC-CMs resemble a more fetal-like or embryonic state and differ from adult CMs in several aspects regarding metabolic signature, electrophysiological properties, and gene expression. Continuing development of protocols allows the generation of iPSC-CMs with more mature characteristics which is important to unlock the full potential of this model system. For instance, optimized media targeting the fatty acid metabolism is reported to improve maturation (Horikoshi et al. 2019; Feyen et al. 2020) and seeding iPSC-CMs on micropatterned surfaces that steers the morphology in a stretched form, resembling the form of human CMs (Carson et al. 2016). These technologies improve the fidelity of iPSC-CMs as disease models. Despite ongoing optimization, iPSC-CMs still carry a strong fetal footprint which requires caution when interpreting experimental data, since most cardiac diseases are chronic and develop over years in the elderly. However, NS is an exception here due to its manifestation during pregnancy and early childhood. In cause of the familial NS case described previously, the HCM for the younger child (II_2) was even

diagnosed prenatally. On this account, iPSC-CMs might be especially suited as a model system for NS.

For this thesis, multiple *LZTR1*-deficient iPSC lines were generated via CRISPR/Cas9 to study the impact of *LZTR1* loss in a cardiac related cell system. Frame shifting mutations were introduced into well-established WT cell lines from our group. With the aim to remodel the gene variants from the Noonan family presented before, mutations were introduced in exon 1 or exon 17. For both approaches, homozygous and heterozygous KOs were generated, resulting in four cell lines in total and the indels were verified on gDNA and mRNA level. After thoroughly confirmation of the pluripotency and correct karyotype, the cell lines were used for differentiation into iPSC-CMs and subsequent experiments. Initial experiments showed a higher RAS-MAPK signaling activity only in the homozygous KO lines and no differences were observed regarding the position of the introduced mutation (exon 1 vs. exon 17). To validate these findings, two additional iPSC with biallelic loss of *LZTR1* were used for additional experiments.

5.2 Cell sizes of *LZTR1*-deficient iPSC-CMs

On cellular level, sizes of ventricular CMs from patients suffering from HCM are altered due to increased number of contractile units. The additionally incorporated sarcomeres lead to increased cellular diameters. Symptoms of NS often include severe forms of HCM even at early ages (Figure 3). It has been reported that the histology of the left ventricular myocardium from NS patients is indistinguishable compared to hypertrophic myocardium that were gathered from patients with idiopathic HCM (Burch et al. 1992). Further, iPSC-CMs generated from HCM patients were shown to recapitulate the hypertrophic phenotype (Lan et al. 2013). Additionally, iPSC-CMs display hypertrophic effects when exposed to the stress factor endothelin 1 for extended time periods (Johansson et al. 2020). It is commonly accepted that iPSC-CMs are capable to recapitulate the hypertrophic phenotype from various cardiac diseases (Eschenhagen and Carrier 2019) including NS (Sakai et al. 2018; Hanses et al. 2020). Sakai et al. demonstrated that maturation of iPSC-CMs is an important factor, as iPSC-CMs derived from NS patients with mutations in *RAF1* showed no differences at ages of d30 and d45 but were significantly larger at d60 compared to WT iPSC-CMs. This report further showed that iPSC-CMs from NS patients might show a less pronounced hypertrophy compared to iPSC-CMs from idiopathic HCM. Another important factor for modeling hypertrophic effects in iPSC-CMs is cell density, as it was shown that iPSC-CMs show a clear

tendency to be smaller when seeded at higher confluence regardless of the underlying diseases (Hanses et al. 2020). To further validate the hypertrophic phenotype of iPSC-CMs caused by *LZTR1* depletion, cell sizes of iPSC-CMs with heterozygous and homozygous *LZTR1* loss were measured in suspension and in adherent conditions and compared to isogenic controls. Automated measurements with the CASY cell counter system revealed that cell size from *LZTR1*-KO iPSC-CMs in suspension were not significantly different compared to their respective WT cell line (Figure 29A). On the other hand, differences within one cell line were observed between separate differentiations. The reasons for this phenomenon remain speculative. Besides natural variability between differentiations, differences in overall confluence of cultures could be causative. Although viability of cells was assessed and a defined cell number was used per well, this does not guarantee a stable survival rate after seeding. Hence, no clear conclusion for recapitulation of the hypertrophic phenotype could be drawn. Noticeably, the size of both WT iPSC-CM lines showed significant differences, underlining once more the importance of isogenic controls for meaningful results. Manually measured areas of adherent cells showed a small but insignificant trend for increased growth (Figure 29B). Overall, the hypertrophic phenotype of CMs from NS patients could not be reproduced in iPSC-CMs. For future experiments, it could be beneficial to evaluate additional methods for cell size measurements like flow cytometry-based approaches with the use of size beads for reference.

5.3 Calcium handling of *LZTR1*-deficient iPSC-CMs

A normal calcium homeostasis within cardiomyocytes is an important determinant of myocardial contractility and calcium dysregulation is associated with cardiac diseases. On single cell level, myocytes from failing hearts exhibit an increased overall calcium leak and calcium transients (CaTs) with a reduced amplitude (Hoang-Trong et al. 2015). The elevated calcium leak is caused by increased occurrence of spontaneous diastolic calcium releases via the ryanodine receptor from the sarcoplasmic reticulum, known as calcium sparks (Cheng et al. 1993) and is described to prolong the calcium transients (Fowler et al. 2020). Our previous study showed that calcium handling genes are higher expressed in NS-patient derived iPSC-CMs and that calcium transients in these cells show abnormal characteristics (Hanses et al. 2020). Driven by this finding, calcium transients of *LZTR1*-KO iPSC-CMs were analyzed via confocal line scanning. The calcium transients were prolonged in *LZTR1* -/- iPSC-CMs. Verapamil is a specific inhibitor for L-type calcium channels and used as a drug for patients

with HCM, especially when treatment with β-blockers is contraindicated (Elliott et al. 2014). Strikingly, verapamil treatment changed the phenotype by shortening of calcium transients to the duration of the untreated isogenic control iPSC-CMs. Interestingly, transient durations of WT cells showed differences to recently published data from our group (Hanses et al. 2020), although performed following similar protocols and using the identical experimental setup. In my setup, CaT rise and CaT decay 50 values for untreated WT iPSC-CMs averaged at ~200 ms and ~500 ms, respectively. Very similar results for rise times of CaTs were reported in a study with WT iPSC-CMs using a comparable setup (Sakai et al. 2018). In contrast, CaT values in our publication averaged around ~450 ms for CaT rise and 1000 ms for CaT decay 50. The only difference are the cell lines that were used. In my setup, WT2 was used as control line exclusively due to the isogenic background with the *LZTR1* -/- iPSC-CMs. In our previous paper, WT2 and two additional WT cell lines were used, and results were pooled for analysis. Since individual cell lines were shown to have different physiological characteristics, this might, at least in parts, explain the differences. Further, verapamil showed contradictory effects in both experimental set ups. Administration of verapamil shortened the prolonged calcium transients in all cell lines in my hands. The drug showed the opposite effect in (Hanses et al. 2020), where shortened calcium transients of iPSC-CMs derived from NS patients were extended with the use of verapamil while it had no effect on WT iPSC-CMs. The divergence in observations remains undetermined and cannot be explained with the use of different cell lines. However, a higher diastolic calcium content as reported in (Sakai et al. 2018) and a trend for a higher SR diastolic calcium leak caused by spontaneous releases of the ryanodine receptor, calcium sparks, indicate that prolonged calcium transients in *LZTR1*-deficient iPSC-CMs are comprehensible.

5.4 RAS-MAPK and AKT activity in *LZTR1*-deficient iPSC-CMs

The pERK/ERK ratio assessed via western blots is commonly used to compare the activity of the RAS-MAPK pathway across different samples and conditions. Overexpression of *LZTR1* in HEK293T cells was shown to reduce endogenous protein levels of pERK while total ERK remained unchanged (Abe et al. 2020). Further, a dose dependent reduction of endogenous RAS assessed via pan-RAS antibodies was observed. These experiments indicated that RAS levels can serve as readout for LZTR1 dependent change in RAS-MAPK signaling. In my hands, overexpression of full length *LZTR1* only showed a small but insignificant reduction of pan-RAS levels in HEK293T cells (Figure 9E-F). Since these experiments require a well-

adjusted balance of the overexpressed protein, it is possible that stronger overexpression of *LZTR1* would show an increased impact on RAS levels.

In the iPSC-CM model, biallelic *LZTR1* loss in iPSC-CMs led to a strong increase of endogenous pan-RAS and MRAS levels (Figure 18). Interestingly, only *LZTR1* -/- cell lines showed a response in RAS-MAPK signaling activity while pan-RAS and MRAS levels remained unaffected in *LZTR1* +/- regardless whether the mutation was introduced in exon 1 or exon 17. This underlines that these *LZTR1* variants mimic the recessive form of NS. The fact that elevated LZTR1 levels reduce RAS, whereas loss of LZTR1 increases RAS levels proves the causative role of LZTR1 in regulation the RAS-MAPK signaling pathway. Since this effect was reproducible in a reliable fashion, a similar clear impact was expected for the pERK/ERK ratio in *LZTR1*-deficient iPSC-CMs. However, pERK and ERK protein levels were elevated in all *LZTR1*-deficient cell lines except for LZTR1 Exon 17 -/-. Although the pERK/ERK ratio was not changed in the samples with elevated ERK and pERK levels, this still indicates a higher overall activity in all *LZTR1*-deficient cell lines (Figure 16). This raises several questions, as no increased pan-RAS and MRAS levels were observed in the *LZTR1* +/- iPSC-CMs (Figure 16A-C). Further, to my best knowledge, increased total ERK levels caused by *LZTR1* loss were not reported before for other cell systems. Since the ERK and pERK protein levels tend to be a highly dynamic and fragile system in iPSC-CMs, this might be a cell type specific effect. As RAS protein levels can be used for quantification of RAS-MAPK activity, this might be better suited as a reliable and stable readout for *LZTR1* mediated disturbances than other members of the pathway.

The effect of *LZTR1* loss on the activity of the AKT signaling pathway was under debate and resulted in different conclusions. Motta et al. demonstrated that overexpression of dominant NS-causing LZTR1 variants in HEK293T cells did not affect the AKT signaling activity (Motta et al. 2019). In contrast, Steklov et al. showed that the pAKT/AKT ratio was elevated in *Lztr1* -/- MEFs after serum stimulation. Further, knockdown of *LZTR1* in primary human Schwann cells did not result in an elevated pAKT/AKT ratio (Steklov et al. 2018). Due to that, they concluded that LZTR1-dependent AKT signaling activity might be cell type specific. Previous results from our group showed that iPSC-CMs from NS patients had stable levels of total AKT, whereas pAKT showed variable protein levels in all samples. Overall, no difference in pAKT/AKT ratio was observed (Hanses et al. 2020). In my hands, total AKT levels of *LZTR1* -/- iPSC-CMs showed no significant difference compared to controls. The pAKT/AKT ratio was upregulated in one *LZTR1*-KO cell line while the second line showed no elevated levels (Figure 17). Since both cell lines carry a biallelic *LZTR1* loss in the first exon, similar results for both cell lines were expected. Presumably, the high variability of pAKT levels are responsible for

the observed differences between both *LZTR1*-KO cell lines. It is to note that other reports required serum stimulation to get signals in immunoblotting. Although stimulation is not necessary to visualize pAKT in iPSC-CMs, additional stimulation could be beneficial to even out the natural variability in CM cultures. In follow up studies, this could allow to observe more robust responses of WT and *LZTR1*-deficient iPSC-CMs in AKT signaling.

5.5 Affinity of LZTR1 for different RAS isoforms

A growing body of studies demonstrates that LZTR1 acts as a regulator for RAS-MAPK signaling by ubiquitination of endogenous RAS proteins including MRAS, NRAS, HRAS, and KRAS (Abe et al. 2020; Bigenzahn et al. 2018; Steklov et al. 2018) as well as RAS related GTPases such as RIT1 (Castel et al. 2019). Although these publications mainly agree on the overall role of LZTR1 to negatively regulate RAS-MAPK activity, striking differences are observed which RAS isoforms exactly are interacting with LZTR1. While Castel et al. reported that LZTR1 interacts with RIT1 and MRAS but not with the other RAS-GTPases by polyubiquitination and degradation (Castel et al. 2019), Abe et al. showed that LZTR1 is able to reduce RAS levels regardless of the specific isoforms. Here, the strongest reduction was seen for MRAS and NRAS while HRAS and KRAS levels were reduced to a lesser extent (Abe et al. 2020). In experiments with HEK293T cells, I observed a similar trend. MRAS level were affected strongly while no change was detected for NRAS and HRAS. Artificial overexpression systems are sensitive to disturbances as endogenous processes are not reflected exactly, meaning that a high overexpressing level of RAS might mask LZTR1-mediated degradation caused by aberrant proportions of these proteins. Bringing together my results and other published data, it is most likely that the affinity of LZTR1 is highest for RIT1 and MRAS and considerably lower for other GTPases or RAS isoforms. However, one limitation for further research regarding the affinity of LZTR1 to different RAS isoforms is the quality of available antibodies. The amino acid sequences of NRAS, HRAS, and KRAS share a very high degree of identity (Hobbs et al. 2016). Although antibodies for the specific isoforms exist, they are very likely to also recognize other RAS isoforms, as demonstrated in a report that evaluated 22 commercially available anti-RAS antibodies. Further, none of the tested antibodies was suited to be used for immunofluorescence of endogenous RAS (Waters et al. 2017). MRAS is an exception, as the amino acid sequence has a weaker alignment with other RAS isoforms (Figure 31). This allows a high degree of antibody specificity (Figure 40). These differences of MRAS compared to other RAS isoforms could also explain the altered affinity for LZTR1.

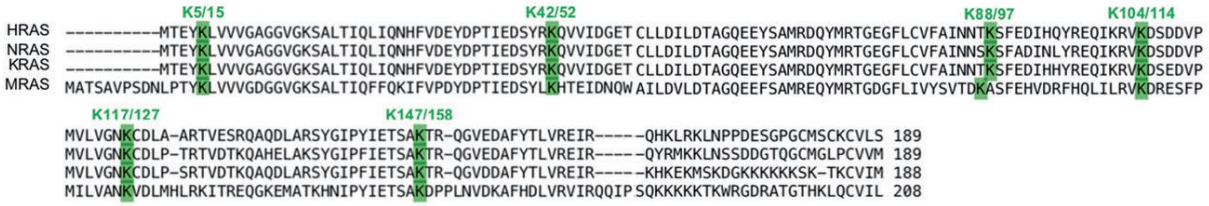

Figure 31: Alignment of RAS isoforms

Alignment of the amino acid sequences demonstrates the high level of identity of HRAS, NRAS, and KRAS, while the sequence of MRAS is less conserved. Reprinted with permission of "*Cell Death & Differentiation" (Abe et al. 2020).*

5.6 LZTR1 antibodies and protein tags

To validate the generated *LZTR1*-KO cell lines on protein level in immunoblotting and to elucidate the subcellular localization of endogenous LZTR1 in iPSC-CMs, reliable antibodies are required. Although *LZTR1* is expressed ubiquitously (Thierry-Mieg and Thierry-Mieg 2006; Wu et al. 2009) which was confirmed via RT-qPCR in iPSCs, HEK293T cells and human fibroblasts (Figure 10E), all antibodies tested did not detect LZTR1 in immunostaining or western blots in these cell types or resulted in unspecific signals. However, one antibody (sc-390166) successfully detected overexpressed LZTR1 in HEK293T cells while it failed to detect endogenous levels in my hands (Figure 8B), although this antibody was reported to detect endogenous levels of LZTR1 via western blots in lysates from human fibroblasts (Castel et al. 2019). Besides that, immunostainings of endogenous LZTR1 especially in cardiac cells was not shown before, since most publications in recent years used overexpression constructs to visualize LZTR1 in HEK293T, HeLa, or similar easy to handle cell systems (Steklov et al. 2018; Bigenzahn et al. 2018). To generate an iPSC line with stable expression of a fluorophore linked to LZTR1, we first attempted a CRISPR/Cas9 based C-terminal insertion of mNeonGreen, a fluorescent protein that is described to be more stable and less sensitive to laser induced bleaching than GFP (Shaner et al. 2013; Hostettler et al. 2017). This was unsuccessful in multiple attempts, presumably due to the high length of the sequence which is less likely to integrate compared to smaller sequences. Because of that, we decided to insert a V5 protein tag instead, which is much smaller (42 bp vs 711 bp). Although the sequence was successfully integrated in LZTR1, either at the C-terminal or the N-terminal part in independent approaches (Figure 10), it was not detectable in immunostainings or western blots. This could be caused by mainly two reasons. The abundance of LZTR1 could be too low for the applied western blot system, which is in line with the finding that LZTR1 specific antibodies can detect

overexpressed LZTR1 but not on endogenous levels. Alternatively, insertion of the V5 sequence in *LZTR1* could cause abnormal splicing events and disrupt protein synthesis. For instance, the paternal mutation (c.1943-256C>T) in NS patients described above prove that a simple deep-intronic SNP can be sufficient to abolish proper protein synthesis. However, PCRs of cDNA for V5-tagged *LZTR1* worked, making the latter scenario unlikely, especially in both cases C-terminal, and N-terminal. Because of that, I conclude that low expression is the plausible reason that endogenous and V5-tagged *LZTR1* remained undetectable. Therefore, we established an overexpression system specifically adjusted for iPSC-CMs.

5.7 Intracellular localization of the LZTR1-CUL3-RAS complex

Full-length LZTR1 overexpressed in HEK293T cells showed a spotted pattern in immunostaining, whereas the subcellular localization was changed to a homogenous cytosolic distribution for the truncated LZTR1 variant that lacks the BTB II and BACK II domains (Figure 8C). This effect was reproducible (and even more pronounced) in iPSC-CMs (Figure 19). This localization change is likely to be specific for autosomal recessive variants of *LZTR1*, as variants with point mutations in the kelch region, representing the autosomal dominant form, where shown to maintain the spotted pattern associated with the WT variant (Steklov et al. 2018; Motta et al. 2019). The clear round shaped and dotted appearance of WT-LZTR1 suggested a co-localization with small cell compartments. In an earlier publication, it was assumed that LZTR1 localizes to golgi (Nacak et al. 2006). I was able to show that LZTR1 does not co-localize with peroxisomes, late endosomes, or lysosomes in iPSC-CMs (Figure 27). More recent reports suggest a possible co-localization with recycling endosomes (Steklov et al. 2018; Bigenzahn et al. 2018).

MRAS, NRAS, and HRAS showed a high degree of co-localization with full-length LZTR1, indicating an interaction with all three isoforms. The truncated LZTR1 variant on the other hand induced a switch of intracellular localization for all RAS isoforms, which then showed the same homogenous distribution as the truncated LZTR1 variant (Figure 25). From that, I conclude that the binding of both proteins is still intact, but cannot be degraded, thus accumulating in the cells. A very similar effect was observed for CUL3, showing the interaction with full length LZTR1 (Figure 23). However, I was not able to directly show the interaction of LZTR1 and RAS isoforms or CUL3 via co-immunoprecipitation due to unspecific signals. Further optimization of this setup could prove this binding in future experiments.

5.8 Proposed model for function of LZTR1

It is now commonly accepted that LZTR1 negatively regulates RAS-MAPK signaling. However, a complete image regarding the role of LZTR1 and specifically its contribution to NS was not drawn yet due to controversies in literature. Part of the debate were possible scenarios of RAS inactivation. It was reported that RAS protein levels were not elevated in *Lztr1* -/- MEFs (Steklov et al. 2018; Castel et al. 2019). Based on these finding from mass spectrometry, Steklov et al. suggested that LZTR1 dependent RAS regulation is a non-degradative mechanism. While this could be true for the murine model, it disagrees with other publications, where a dose dependent LZTR1-mediated RAS protein level reduction was shown in human cell systems (Abe et al. 2020). This also supports my results, where pan-RAS and MRAS protein levels showed increased abundance in immunoblots of *LZTR1* -/- iPSC-CMs (Figure 17). With that findings, I conclude that LZTR1 regulates RAS activity via a degradative mechanism.

Although NS causing mutations in most genes are mainly autosomal dominant, defects in *LZTR1* can elicit NS in an autosomal dominant form as well as in an autosomal recessive form. Comparing both forms, Motta et al. showed that RAS-MAPK signaling is elevated in the autosomal dominant form while pathway activity is not affected by the autosomal recessive form (Motta et al. 2019). These results were based on overexpression of disease causing *LZTR1* variants in COS-1 cells with subsequent analysis of RAS-MAPK activity via immunoblots. Since recessive *LZTR1* variants were shown to be loss-of-function mutations, overexpression of these constructs would not interfere with the endogenous LZTR1-mediated RAS degradation machinery and changes in RAS-MAPK activity are not expected. The conclusion drawn here, that recessive variants of LZTR1 do not cause RAS-MAPK disturbances might be incorrect. To display the effects of recessive forms of LZTR1 on RAS-MAPK signaling, a cell system without a functional endogenous LZTR1 system is required. In adequate cell models, our group demonstrated that *LZTR1* variants responsible for recessive NS indeed resulted in elevated RAS-MAPK signaling in patient specific iPSC-CMs (Hanses et al. 2020). This was reproducible in the CRISPR/Cas9 based *LZTR1*-KO iPSC-CMs generated in this thesis (Figure 17). However, elevated RAS protein levels caused by overexpression of autosomal dominant LZTR1 variants indicate interference with endogenous WT-LZTR1 proteins which hamper its function in a dominant negative way. These autosomal dominant mutations mostly cluster around the substrate binding kelch domains 1-4 near the N-terminus

(Pagnamenta et al. 2019; Motta et al. 2019; Yamamoto et al. 2015). Presumably, these variants can still form dimers due to the intact BTB II and BACK II domains but are unable to bind RAS. In terms of disease development, heterozygous kelch mutant variants would competitively bind to WT-LZTR1, which results in a dominant form of NS. Dimers consisting of two WT proteins still exist in this scenario. Hence, LZTR1 mediated RAS degradation is reduced but still rendered weakly active (Figure 32C). Steklov et al. showed that LZTR1 variants with mutations near the C-terminus in the BTB II and BACK II domain most likely lose the capability to dimerize, as demonstrated for the variant LZTR1-L812P (Steklov et al. 2018). They concluded that the BACK II domain is required for dimerization and determines the subcellular localization. In contrast to that, Castel et al. showed in detail that mainly the BTB I and BACK I domain facilitate LZTR1 dimerization (Castel et al. 2019). Although this question might not be finally answered, our proposed model for LZTR1 is based on the results from Castel et al. Heterozygous expression of autosomal recessive LZTR1 variants with mutations in regions that lead to improper subcellular localization or a complete loss of the protein are non-pathogenic since the remaining WT allele can compensate the loss (Figure 32A-B). On the other hand, biallelic expression of autosomal recessive LZTR1 variants abolishes LZTR1 function completely, resulting in the most serious form of NS. Depending on the position of the mutation, RAS and CUL3 could still bind, but loss of the BTB II and BACK II domains would impair proper localization of the protein complex and possibly also proteasomal degradation (Figure 32D). Our data support this theory as we showed that these protein variants have an abnormal subcellular localization (Figure 19) but still changed RAS localization (Figure 25).

This model could explain how the highly variable severity of the disease correlates with levels of LZTR1 function (Figure 32D) and fits to the observation that recessive forms of NS are suspected to cause the most serious cardiac conditions (Güemes et al. 2019). In a study that compared symptoms of children displaying the recessive form of NS caused by biallelic *LZTR1* loss, 16 out of 20 patients were diagnosed with HCM. Since the prevalence of HCM is described with a prevalence of 20% of all NS cases, this indicates an increased occurrence in the autosomal recessive form (Johnston et al. 2018). Carriers of heterozygous mutations of recessive *LZTR1* variants are considered healthy but in rare cases, these variants were associated with very slight symptoms that are associated with NS (short stature, ptosis) (Johnston et al. 2018). Since heterozygous mutations of these variants are non-pathogenic, carriers are commonly only detected after their children are diagnosed with NS. Taken together, we assume that even LZTR1 variants that are still capable of binding both, RAS and CUL3 can still be NS-causing as intact BTB II and BACK II domains are required for correct localization at recycling endosomes for subsequent proteasomal degradation. Nevertheless,

the proposed model that LZTR1 abundance shows a correlation with severity of NS will require a detailed monitoring of the clinical presentation of NS patients in both, the dominant and recessive form. Also, further in-depth studies are needed to validate the hypothesis.

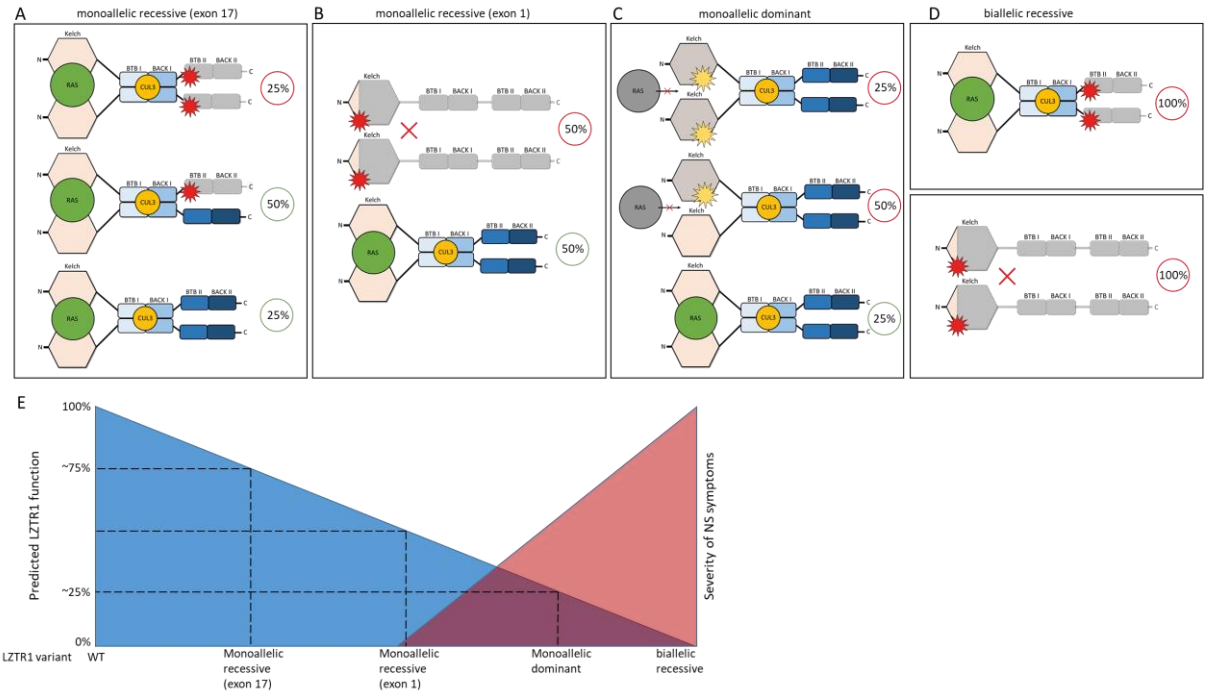

Figure 32: Proposed model of LZTR1

A, Monoallelic LZTR1 variants without functional BTB II and BACK II domains can dimerize, resulting in 3 possible combinations. This leads to a mild, non-pathogenic reduction of LZTR1 function. Sites of frame shifting mutations are marked with a red star. Percentage numbers encircled in red mark non-functional LZTR1 interactions, while numbers encircled in green indicate functional LZTR1 dimers. **B,** Monoallelic recessive LZTR1 variants with frameshifting mutations in the Kelch domain lead to early termination of protein synthesis. This form is non-pathogenic, since the truncated variants do not competitively bind to WT-LZTR1, keeping protein function at ~50%. **C,** Monoallelic dominant LZTR1 variants have defective binding of RAS. These variants still form dimers and competitively bind to WT-LZTR1 which leads to a strong reduction of LZTR1 function, causing NS. Point mutations in the kelch domain are highlighted with a yellow star. **D,** Biallelic recessive LZTR1 variants with frame shifting mutations in the BTB II domain result in a complete loss of function by mislocalization. Depending on the site of mutation, biallelic recessive variants can lead to complete loss of protein function. **E,** Model for the proposed connection between LZTR1 activity and severity of NS.

5.9 Summary and Outlook

During the past 2 years, tremendous scientific progress was made regarding LZTR1 functions. It went from a nearly undescribed to a well characterized protein and its connection to NS was proven in many reports. However, it was not exactly understood in which way autosomal dominant and autosomal recessive LZTR1 variants contribute to the development of NS. With the use of CRISPR/Cas9 based *LZTR1* -/- and +/- iPSC-CMs models I was able to underscore the pathogenic role of the protein, showing in particular that recessive variants lead increased abundance of RAS and abnormal calcium handling. Further, by overexpression of full-length and recessive LZTR1 variants in iPSC-CMs, we showed that NS is caused by mislocalization of the RAS-LZTR1 complex. Although some aspects of the disease like increased cell size could not be recapitulated, iPSCs are a well-suited system to model NS.

In short, the main findings of this thesis are:

- Truncated LZTR1 variants that account to the recessive form of NS show abnormal subcellular localization and the protein accumulates in cells, although expression levels are not changed

- MRAS and pan-RAS protein levels are elevated in *LZTR1* -/- iPSC-CMs but not in *LZTR1* +/- iPSC-CMs. LZTR1 mediated RAS inactivation is a degradative mechanism

- WT-LZTR1 and recessive LZTR1 variants missing the BTB II and BACK II domains co-localize with MRAS, NRAS, HRAS and CUL3 in iPSC-CMs with a pronounced affinity for MRAS.

- *LZTR1* -/- iPSC-CMs show pathogenic calcium handling characteristics that can partially be rescued by verapamil treatment

In the following months, the generated *LZTR1*-deficient iPSC-CMs will be used for further work as a valuable tool to uncover possible alterations of metabolic gene expression and possible defects in metabolic functions. Proteomics data gathered from LZTR1 +/- and -/- iPSC-CMs will give valuable insights to answer the question which RAS isoforms are mainly affected by LZTR1 mediated protein degradation in cardiac cells. In another approach, it will be elucidated whether RAS silencing can rescue the enhanced activity of the RAS-MAPK signaling pathway in *LZTR1*-deficient iPSC-CMs.

6 Appendix

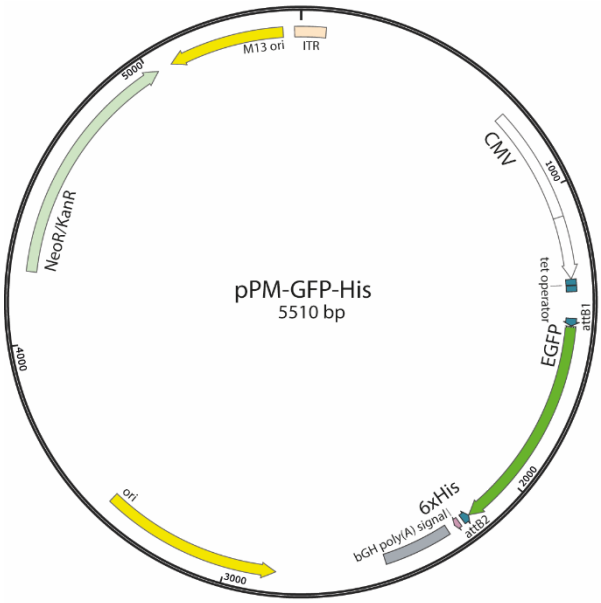

Figure 33: Plasmid pPM-GFP-His, 5510 bp. Designed with SnapGene

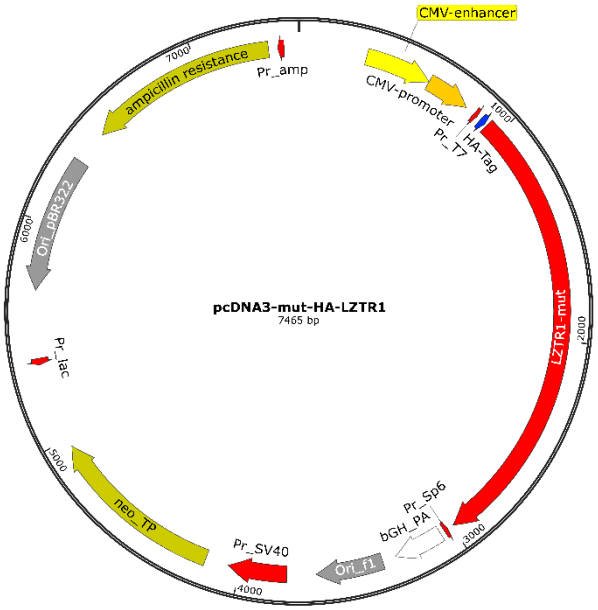

Figure 34: Plasmid pcDNA3-mut-HA-LZTR1, 7465 bp. Designed with SnapGene

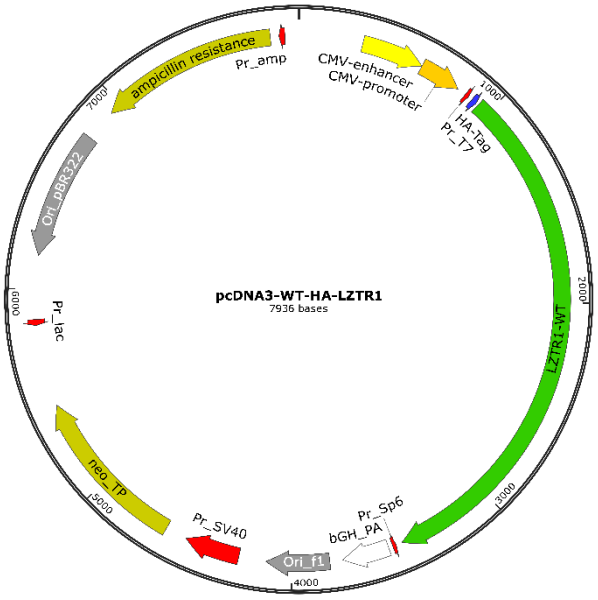

Figure 35: Plasmid pcDNA3-WT-HA-LZTR1, 7936 bp. Designed with SnapGene

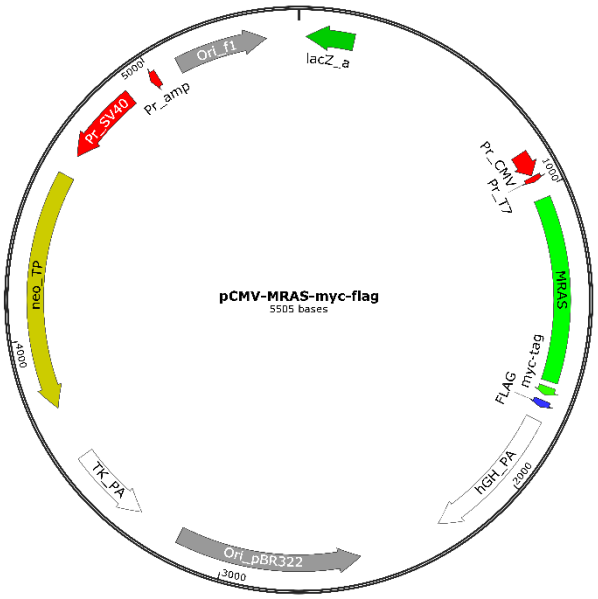

Figure 36: Plasmid pCMV-MRAS-myc-flag, 5505 bp Designed with SnapGene

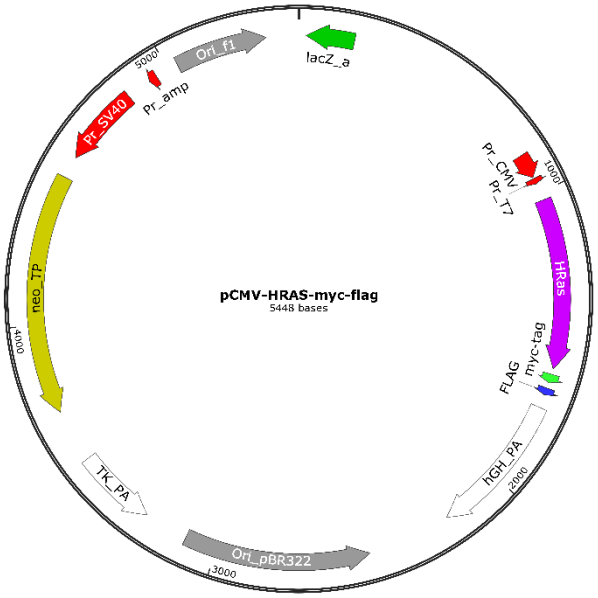

Figure 37: Plasmid pCMV-HRAS-myc-flag, 5448 bp. Designed with SnapGene

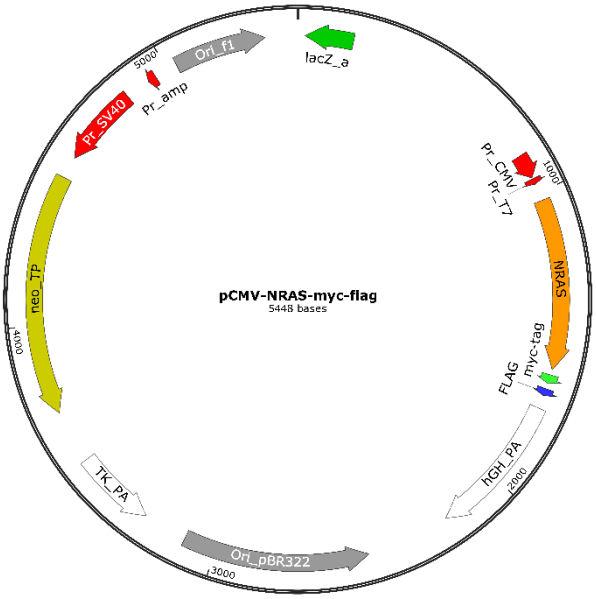

Figure 38: Plasmid pCMV-NRAS-myc-flag, 5448 bp. Designed with SnapGene

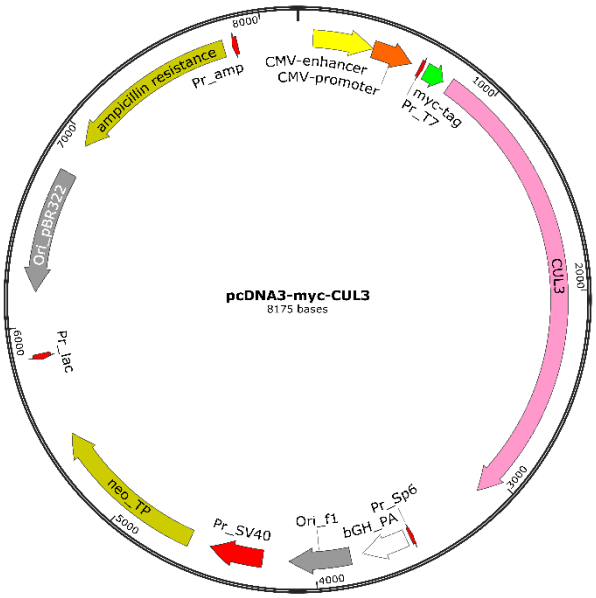

Figure 39: Plasmid pcDNA3-myc-CUL3, 8175 bp. Designed with SnapGene

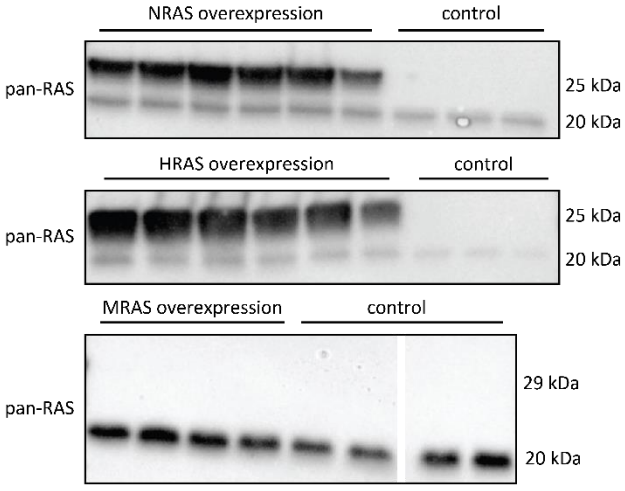

Figure 40: pan-RAS antibody does not detect MRAS

Lysates of HEK293T cells transiently overexpressing the indicated constructs were immunoblotted with pan-RAS antibody. The pan-RAS antibody detects endogenous RAS in all samples (lower, weaker band). Overexpressed NRAS-FLAG and HRAS-FLAG is also detected with the pan-RAS antibody. Due to the carried protein-tag, this band appears at a higher protein size. Overexpressed MRAS is not detected by the pan-RAS antibody.

7 References

Abe, Taiki; Umeki, Ikumi; Kanno, Shin-Ichiro; Inoue, Shin-Ichi; Niihori, Tetsuya; Aoki, Yoko (2020): LZTR1 facilitates polyubiquitination and degradation of RAS-GTPases. In: *Cell death and differentiation* 27 (3), S. 1023–1035. DOI: 10.1038/s41418-019-0395-5.

Aoki, Yoko; Niihori, Tetsuya; Banjo, Toshihiro; Okamoto, Nobuhiko; Mizuno, Seiji; Kurosawa, Kenji et al. (2013): Gain-of-function mutations in RIT1 cause Noonan syndrome, a RAS/MAPK pathway syndrome. In: *American journal of human genetics* 93 (1), S. 173–180. DOI: 10.1016/j.ajhg.2013.05.021.

Aoki, Yoko; Niihori, Tetsuya; Inoue, Shin-Ichi; Matsubara, Yoichi (2015): Recent advances in RASopathies. In: *Journal of human genetics* 61 (1), S. 33–39. DOI: 10.1038/jhg.2015.114.

Ben Jehuda, Ronen; Shemer, Yuval; Binah, Ofer (2018): Genome Editing in Induced Pluripotent Stem Cells using CRISPR/Cas9. In: *Stem cell reviews and reports* 14 (3), S. 323–336. DOI: 10.1007/s12015-018-9811-3.

Bigenzahn, Johannes W.; Collu, Giovanna M.; Kartnig, Felix; Pieraks, Melanie; Vladimer, Gregory I.; Heinz, Leonhard X. et al. (2018): LZTR1 is a regulator of RAS ubiquitination and signaling. In: *Science (New York, N.Y.)* 362 (6419), S. 1171–1177. DOI: 10.1126/science.aap8210.

Bos, J. L. (1989): ras oncogenes in human cancer: a review. In: *Cancer research* 49 (17), S. 4682–4689.

Burch, M.; Mann, J. M.; Sharland, M.; Shinebourne, E. A.; Patton, M. A.; McKenna, W. J. (1992): Myocardial disarray in Noonan syndrome. In: *British heart journal* 68 (6), S. 586–588. DOI: 10.1136/hrt.68.12.586.

Carson, Daniel; Hnilova, Marketa; Yang, Xiulan; Nemeth, Cameron L.; Tsui, Jonathan H.; Smith, Alec S. T. et al. (2016): Nanotopography-Induced Structural Anisotropy and Sarcomere Development in Human Cardiomyocytes Derived from Induced Pluripotent Stem Cells. In: *ACS applied materials & interfaces* 8 (34), S. 21923–21932. DOI: 10.1021/acsami.5b11671.

Castel, Pau; Cheng, Alice; Cuevas-Navarro, Antonio; Everman, David B.; Papageorge, Alex G.; Simanshu, Dhirendra K. et al. (2019): RIT1 oncoproteins escape LZTR1-mediated proteolysis. In: *Science (New York, N.Y.)* 363 (6432), S. 1226–1230. DOI: 10.1126/science.aav1444.

Castellano, Esther; Santos, Eugenio (2011): Functional specificity of ras isoforms: so similar but so different. In: *Genes & cancer* 2 (3), S. 216–231. DOI: 10.1177/1947601911408081.

Chen, Peng-Chieh; Yin, Jiani; Yu, Hui-Wen; Yuan, Tao; Fernandez, Minerva; Yung, Christina K. et al. (2014): Next-generation sequencing identifies rare variants associated with Noonan syndrome. In: *Proceedings of the National Academy of Sciences of the United States of America* 111 (31), S. 11473–11478. DOI: 10.1073/pnas.1324128111.

Chen, Xu; Mitsutake, Norisato; LaPerle, Krista; Akeno, Nagako; Zanzonico, Pat; Longo, Valerie A. et al. (2009): Endogenous expression of Hras(G12V) induces developmental defects and neoplasms with copy number imbalances of the oncogene. In: *Proceedings of the National Academy of Sciences of the United States of America* 106 (19), S. 7979–7984. DOI: 10.1073/pnas.0900343106.

Cheng, H.; Lederer, W. J.; Cannell, M. B. (1993): Calcium sparks: elementary events underlying excitation-contraction coupling in heart muscle. In: *Science (New York, N.Y.)* 262 (5134), S. 740–744. DOI: 10.1126/science.8235594.

Cirstea, Ion C.; Kutsche, Kerstin; Dvorsky, Radovan; Gremer, Lothar; Carta, Claudio; Horn, Denise et al. (2010): A restricted spectrum of NRAS mutations causes Noonan syndrome. In: *Nature genetics* 42 (1), S. 27–29. DOI: 10.1038/ng.497.

Cordeddu, Viviana; Di Schiavi, Elia; Pennacchio, Len A.; Ma'ayan, Avi; Sarkozy, Anna; Fodale, Valentina et al. (2009): Mutation of SHOC2 promotes aberrant protein N-myristoylation and causes Noonan-like syndrome with loose anagen hair. In: *Nature genetics* 41 (9), S. 1022–1026. DOI: 10.1038/ng.425.

Dickinson, Mary E.; Flenniken, Ann M.; Ji, Xiao; Teboul, Lydia; Wong, Michael D.; White, Jacqueline K. et al. (2016): High-throughput discovery of novel developmental phenotypes. In: *Nature* 537 (7621), S. 508–514. DOI: 10.1038/nature19356.

DuBridge, R. B.; Tang, P.; Hsia, H. C.; Leong, P. M.; Miller, J. H.; Calos, M. P. (1987): Analysis of mutation in human cells by using an Epstein-Barr virus shuttle system. In: *Molecular and cellular biology* 7 (1), S. 379–387. DOI: 10.1128/mcb.7.1.379.

El-Battrawy, Ibrahim; Lan, Huan; Cyganek, Lukas; Zhao, Zhihan; Li, Xin; Buljubasic, Fanis et al. (2018): Modeling Short QT Syndrome Using Human-Induced Pluripotent Stem Cell-Derived Cardiomyocytes. In: *Journal of the American Heart Association* 7 (7). DOI: 10.1161/JAHA.117.007394.

Elliott, Perry M.; Anastasakis, Aris; Borger, Michael A.; Borggrefe, Martin; Cecchi, Franco; Charron, Philippe et al. (2014): 2014 ESC Guidelines on diagnosis and management of hypertrophic cardiomyopathy: the Task Force for the Diagnosis and Management of Hypertrophic Cardiomyopathy of the European Society of Cardiology (ESC). In: *European heart journal* 35 (39), S. 2733–2779. DOI: 10.1093/eurheartj/ehu284.

Eschenhagen, Thomas; Carrier, Lucie (2019): Cardiomyopathy phenotypes in human-induced pluripotent stem cell-derived cardiomyocytes-a systematic review. In: *Pflugers Archiv : European journal of physiology* 471 (5), S. 755–768. DOI: 10.1007/s00424-018-2214-0.

Feyen, Dries A. M.; McKeithan, Wesley L.; Bruyneel, Arne A. N.; Spiering, Sean; Hörmann, Larissa; Ulmer, Bärbel et al. (2020): Metabolic Maturation Media Improve Physiological Function of Human iPSC-Derived Cardiomyocytes. In: *Cell reports* 32 (3), S. 107925. DOI: 10.1016/j.celrep.2020.107925.

Flex, Elisabetta; Jaiswal, Mamta; Pantaleoni, Francesca; Martinelli, Simone; Strullu, Marion; Fansa, Eyad K. et al. (2014): Activating mutations in RRAS underlie a phenotype within the RASopathy spectrum and contribute to leukaemogenesis. In: *Human molecular genetics* 23 (16), S. 4315–4327. DOI: 10.1093/hmg/ddu148.

Fowler, Ewan D.; Wang, Nan; Hezzell, Melanie; Chanoit, Guillaume; Hancox, Jules C.; Cannell, Mark B. (2020): Arrhythmogenic late Ca2+ sparks in failing heart cells and their control by action potential configuration. In: *Proceedings of the National Academy of Sciences of the United States of America* 117 (5), S. 2687–2692. DOI: 10.1073/pnas.1918649117.

Frattini, Veronique; Trifonov, Vladimir; Chan, Joseph Minhow; Castano, Angelica; Lia, Marie; Abate, Francesco et al. (2013): The integrated landscape of driver genomic alterations in glioblastoma. In: *Nature genetics* 45 (10), S. 1141–1149. DOI: 10.1038/ng.2734.

Furukawa, Manabu; He, Yizhou Joseph; Borchers, Christoph; Xiong, Yue (2003): Targeting of protein ubiquitination by BTB-Cullin 3-Roc1 ubiquitin ligases. In: *Nature cell biology* 5 (11), S. 1001–1007. DOI: 10.1038/ncb1056.

Garg, Priyanka; Oikonomopoulos, Angelos; Chen, Haodong; Li, Yingxin; Lam, Chi Keung; Sallam, Karim et al. (2018): Genome Editing of Induced Pluripotent Stem Cells to Decipher Cardiac Channelopathy Variant. In: *Journal of the American College of Cardiology* 72 (1), S. 62–75. DOI: 10.1016/j.jacc.2018.04.041.

Gelb, Bruce D.; Roberts, Amy E.; Tartaglia, Marco (2015): Cardiomyopathies in Noonan syndrome and the other RASopathies. In: *Progress in pediatric cardiology* 39 (1), S. 13–19. DOI: 10.1016/j.ppedcard.2015.01.002.

Geyer, Rory; Wee, Susan; Anderson, Scott; Yates, John; Wolf, Dieter A. (2003): BTB/POZ Domain Proteins Are Putative Substrate Adaptors for Cullin 3 Ubiquitin Ligases. In: *Molecular Cell* 12 (3), S. 783–790. DOI: 10.1016/s1097-2765(03)00341-1.

Gonzalez, Rodolfo; Lee, Jae Wook; Schultz, Peter G. (2011): Stepwise chemically induced cardiomyocyte specification of human embryonic stem cells. In: *Angewandte Chemie (International ed. in English)* 50 (47), S. 11181–11185. DOI: 10.1002/anie.201103909.

Gripp, Karen W.; Aldinger, Kimberly A.; Bennett, James T.; Baker, Laura; Tusi, Jessica; Powell-Hamilton, Nina et al. (2016): A novel rasopathy caused by recurrent de novo missense mutations in PPP1CB closely resembles Noonan syndrome with loose anagen hair. In: *American journal of medical genetics. Part A* 170 (9), S. 2237–2247. DOI: 10.1002/ajmg.a.37781.

Guatimosim, Silvia; Guatimosim, Cristina; Song, Long-Sheng (2011): Imaging calcium sparks in cardiac myocytes. In: *Methods in molecular biology (Clifton, N.J.)* 689, S. 205–214. DOI: 10.1007/978-1-60761-950-5_12.

Güemes, María; Martín-Rivada, Álvaro; Ortiz-Cabrera, Neimar Valentina; Martos-Moreno, Gabriel Ángel; Pozo-Román, Jesús; Argente, Jesús (2019): LZTR1: Genotype Expansion in Noonan Syndrome. In: *Hormone research in paediatrics* 92 (4), S. 269–275. DOI: 10.1159/000502741.

Hamada, Atsuko; Akagi, Eri; Obayashi, Fumitaka; Yamasaki, Sachiko; Koizumi, Koichi; Ohtaka, Manami et al. (2020): Induction of Noonan syndrome-specific human-induced pluripotent stem cells under serum-, feeder-, and integration-free conditions. In: *In vitro cellular & developmental biology. Animal* 56 (10), S. 888–895. DOI: 10.1007/s11626-020-00515-9.

Hanke, T.; Szawlowski, P.; Randall, R. E. (1992): Construction of solid matrix-antibody-antigen complexes containing simian immunodeficiency virus p27 using tag-specific monoclonal antibody and tag-linked antigen. In: *The Journal of general virology* 73 (Pt 3), S. 653–660. DOI: 10.1099/0022-1317-73-3-653.

Hanses, Ulrich; Kleinsorge, Mandy; Roos, Lennart; Yigit, Gökhan; Li, Yun; Barbarics, Boris et al. (2020): Intronic CRISPR Repair in a Preclinical Model of Noonan Syndrome-Associated Cardiomyopathy. In: *Circulation* 142 (11), S. 1059–1076. DOI: 10.1161/CIRCULATIONAHA.119.044794.

Hickey, Edward J.; Mehta, Rohit; Elmi, Maryam; Asoh, Kentaro; McCrindle, Brian W.; Williams, William G. et al. (2011): Survival implications: hypertrophic cardiomyopathy in Noonan syndrome. In: *Congenital heart disease* 6 (1), S. 41–47. DOI: 10.1111/j.1747-0803.2010.00465.x.

Higgins, Erin M.; Bos, J. Martijn; Dotzler, Steven M.; John Kim, C. S.; Ackerman, Michael J. (2019): MRAS Variants Cause Cardiomyocyte Hypertrophy in Patient-Specific Induced Pluripotent Stem Cell-Derived Cardiomyocytes: Additional Evidence for MRAS as a Definitive Noonan Syndrome-Susceptibility Gene. In: *Circulation. Genomic and precision medicine* 12 (11), e002648. DOI: 10.1161/CIRCGEN.119.002648.

Hoang-Trong, Tuan M.; Ullah, Aman; Jafri, M. Saleet (2015): Calcium Sparks in the Heart: Dynamics and Regulation. In: *Research and reports in biology* 6, S. 203–214. DOI: 10.2147/RRB.S61495.

Hobbs, G. Aaron; Der, Channing J.; Rossman, Kent L. (2016): RAS isoforms and mutations in cancer at a glance. In: *Journal of cell science* 129 (7), S. 1287–1292. DOI: 10.1242/jcs.182873.

Hockemeyer, Dirk; Jaenisch, Rudolf (2016): Induced Pluripotent Stem Cells Meet Genome Editing. In: *Cell stem cell* 18 (5), S. 573–586. DOI: 10.1016/j.stem.2016.04.013.

Horikoshi, Yuichi; Yan, Yasheng; Terashvili, Maia; Wells, Clive; Horikoshi, Hisako; Fujita, Satoshi et al. (2019): Fatty Acid-Treated Induced Pluripotent Stem Cell-Derived Human Cardiomyocytes Exhibit Adult Cardiomyocyte-Like Energy Metabolism Phenotypes. In: *Cells* 8 (9). DOI: 10.3390/cells8091095.

Hostettler, Lola; Grundy, Laura; Käser-Pébernard, Stéphanie; Wicky, Chantal; Schafer, William R.; Glauser, Dominique A. (2017): The Bright Fluorescent Protein mNeonGreen Facilitates Protein Expression Analysis In Vivo. In: *G3 (Bethesda, Md.)* 7 (2), S. 607–615. DOI: 10.1534/g3.116.038133.

Human Protein Atlas. Online verfügbar unter https://www.proteinatlas.org/ENSG00000158186-MRAS/tissue, zuletzt geprüft am 23.03.2021.

Itzhaki, Ilanit; Maizels, Leonid; Huber, Irit; Gepstein, Amira; Arbel, Gil; Caspi, Oren et al. (2012): Modeling of catecholaminergic polymorphic ventricular tachycardia with patient-specific human-induced pluripotent stem cells. In: *Journal of the American College of Cardiology* 60 (11), S. 990–1000. DOI: 10.1016/j.jacc.2012.02.066.

Jaffré, Fabrice; Miller, Clint L.; Schänzer, Anne; Evans, Todd; Roberts, Amy E.; Hahn, Andreas; Kontaridis, Maria I. (2019): Inducible Pluripotent Stem Cell-Derived

Cardiomyocytes Reveal Aberrant Extracellular Regulated Kinase 5 and Mitogen-Activated Protein Kinase Kinase 1/2 Signaling Concomitantly Promote Hypertrophic Cardiomyopathy in RAF1-Associated Noonan Syndrome. In: *Circulation* 140 (3), S. 207–224. DOI: 10.1161/CIRCULATIONAHA.118.037227.

Johansson, Markus; Ulfenborg, Benjamin; Andersson, Christian X.; Heydarkhan-Hagvall, Sepideh; Jeppsson, Anders; Sartipy, Peter; Synnergren, Jane (2020): Cardiac hypertrophy in a dish: a human stem cell based model. In: *Biology open* 9 (9). DOI: 10.1242/bio.052381.

Johnston, Jennifer J.; van der Smagt, Jasper J.; Rosenfeld, Jill A.; Pagnamenta, Alistair T.; Alswaid, Abdulrahman; Baker, Eva H. et al. (2018): Autosomal recessive Noonan syndrome associated with biallelic LZTR1 variants. In: *Genetics in medicine : official journal of the American College of Medical Genetics* 20 (10), S. 1175–1185. DOI: 10.1038/gim.2017.249.

Jorge, Alexander A. L.; Malaquias, Alexsandra C.; Arnhold, Ivo J. P.; Mendonca, Berenice B. (2009): Noonan syndrome and related disorders: a review of clinical features and mutations in genes of the RAS/MAPK pathway. In: *Hormone research* 71 (4), S. 185–193. DOI: 10.1159/000201106.

Ju, Younghee; Park, Jun Sung; Kim, Daejeong; Kim, Bumsoo; Lee, Jeong Ho; Nam, Yoonkey et al. (2020): SHP2 mutations induce precocious gliogenesis of Noonan syndrome-derived iPSCs during neural development in vitro. In: *Stem cell research & therapy* 11 (1), S. 209. DOI: 10.1186/s13287-020-01709-4.

Karnoub, Antoine E.; Weinberg, Robert A. (2008): Ras oncogenes: split personalities. In: *Nature reviews. Molecular cell biology* 9 (7), S. 517–531. DOI: 10.1038/nrm2438.

Kleinsorge, Mandy; Cyganek, Lukas (2020): Subtype-Directed Differentiation of Human iPSCs into Atrial and Ventricular Cardiomyocytes. In: *STAR protocols* 1 (1), S. 100026. DOI: 10.1016/j.xpro.2020.100026.

Kodo, Kazuki; Ong, Sang-Ging; Jahanbani, Fereshteh; Termglinchan, Vittavat; Hirono, Keiichi; InanlooRahatloo, Kolsoum et al. (2016): iPSC-derived cardiomyocytes reveal abnormal TGF-β signalling in left ventricular non-compaction cardiomyopathy. In: *Nature cell biology* 18 (10), S. 1031–1042. DOI: 10.1038/ncb3411.

Kujala, Kirsi; Paavola, Jere; Lahti, Anna; Larsson, Kim; Pekkanen-Mattila, Mari; Viitasalo, Matti et al. (2012): Cell model of catecholaminergic polymorphic ventricular tachycardia reveals early and delayed afterdepolarizations. In: *PloS one* 7 (9), e44660. DOI: 10.1371/journal.pone.0044660.

Kussauer, Sophie; David, Robert; Lemcke, Heiko (2019): hiPSCs Derived Cardiac Cells for Drug and Toxicity Screening and Disease Modeling: What Micro- Electrode-Array Analyses Can Tell Us. In: *Cells* 8 (11). DOI: 10.3390/cells8111331.

La Roche, Jeanne de; Angsutararux, Paweorn; Kempf, Henning; Janan, Montira; Bolesani, Emiliano; Thiemann, Stefan et al. (2019): Comparing human iPSC-cardiomyocytes versus HEK293T cells unveils disease-causing effects of Brugada mutation A735V of NaV1.5 sodium channels. In: *Scientific reports* 9 (1), S. 11173. DOI: 10.1038/s41598-019-47632-4.

Lam, Albert Q.; Freedman, Benjamin S.; Morizane, Ryuji; Lerou, Paul H.; Valerius, M. Todd; Bonventre, Joseph V. (2014): Rapid and efficient differentiation of human pluripotent stem cells into intermediate mesoderm that forms tubules expressing kidney proximal tubular

markers. In: *Journal of the American Society of Nephrology : JASN* 25 (6), S. 1211–1225. DOI: 10.1681/ASN.2013080831.

Lan, Feng; Lee, Andrew S.; Liang, Ping; Sanchez-Freire, Veronica; Nguyen, Patricia K.; Wang, Li et al. (2013): Abnormal calcium handling properties underlie familial hypertrophic cardiomyopathy pathology in patient-specific induced pluripotent stem cells. In: *Cell stem cell* 12 (1), S. 101–113. DOI: 10.1016/j.stem.2012.10.010.

Lee, D. H.; Goldberg, A. L. (1996): Selective inhibitors of the proteasome-dependent and vacuolar pathways of protein degradation in Saccharomyces cerevisiae. In: *The Journal of biological chemistry* 271 (44), S. 27280–27284. DOI: 10.1074/jbc.271.44.27280.

Lian, Xiaojun; Zhang, Jianhua; Azarin, Samira M.; Zhu, Kexian; Hazeltine, Laurie B.; Bao, Xiaoping et al. (2013): Directed cardiomyocyte differentiation from human pluripotent stem cells by modulating Wnt/β-catenin signaling under fully defined conditions. In: *Nature protocols* 8 (1), S. 162–175. DOI: 10.1038/nprot.2012.150.

Livak, K. J.; Schmittgen, T. D. (2001): Analysis of relative gene expression data using real-time quantitative PCR and the 2(-Delta Delta C(T)) Method. In: *Methods (San Diego, Calif.)* 25 (4), S. 402–408. DOI: 10.1006/meth.2001.1262.

Maegley, K. A.; Admiraal, S. J.; Herschlag, D. (1996): Ras-catalyzed hydrolysis of GTP: a new perspective from model studies. In: *Proceedings of the National Academy of Sciences of the United States of America* 93 (16), S. 8160–8166. DOI: 10.1073/pnas.93.16.8160.

Malik, Nasir; Rao, Mahendra S. (2013): A review of the methods for human iPSC derivation. In: *Methods in molecular biology (Clifton, N.J.)* 997, S. 23–33. DOI: 10.1007/978-1-62703-348-0_3.

Marino, Bruno; Digilio, Maria Cristina; Toscano, Alessandra; Giannotti, Aldo; Dallapiccola, Bruno (1999): Congenital heart diseases in children with Noonan syndrome: An expanded cardiac spectrum with high prevalence of atrioventricular canal. In: *The Journal of Pediatrics* 135 (6), S. 703–706. DOI: 10.1016/s0022-3476(99)70088-0.

Martinelli, Simone; Luca, Alessandro de; Stellacci, Emilia; Rossi, Cesare; Checquolo, Saula; Lepri, Francesca et al. (2010): Heterozygous germline mutations in the CBL tumor-suppressor gene cause a Noonan syndrome-like phenotype. In: *American journal of human genetics* 87 (2), S. 250–257. DOI: 10.1016/j.ajhg.2010.06.015.

McDermott-Roe, Chris; Lv, Wenjian; Maximova, Tania; Wada, Shogo; Bukowy, John; Marquez, Maribel et al. (2019): Investigation of a dilated cardiomyopathy-associated variant in BAG3 using genome-edited iPSC-derived cardiomyocytes. In: *JCI insight* 4 (22). DOI: 10.1172/jci.insight.128799.

Mendez, H. M.; Opitz, J. M. (1985): Noonan syndrome: a review. In: *American journal of medical genetics* 21 (3), S. 493–506. DOI: 10.1002/ajmg.1320210312.

Moore, J. K.; Haber, J. E. (1996): Cell cycle and genetic requirements of two pathways of nonhomologous end-joining repair of double-strand breaks in Saccharomyces cerevisiae. In: *Molecular and cellular biology* 16 (5), S. 2164–2173. DOI: 10.1128/mcb.16.5.2164.

Moretti, Alessandra; Bellin, Milena; Welling, Andrea; Jung, Christian Billy; Lam, Jason T.; Bott-Flügel, Lorenz et al. (2010): Patient-specific induced pluripotent stem-cell models for

long-QT syndrome. In: *The New England journal of medicine* 363 (15), S. 1397–1409. DOI: 10.1056/NEJMoa0908679.

Motta, Marialetizia; Fidan, Miray; Bellacchio, Emanuele; Pantaleoni, Francesca; Schneider-Heieck, Konstantin; Coppola, Simona et al. (2019): Dominant Noonan syndrome-causing LZTR1 mutations specifically affect the Kelch domain substrate-recognition surface and enhance RAS-MAPK signaling. In: *Human molecular genetics* 28 (6), S. 1007–1022. DOI: 10.1093/hmg/ddy412.

Mutlak, Michael; Kehat, Izhak (2015): Extracellular signal-regulated kinases 1/2 as regulators of cardiac hypertrophy. In: *Frontiers in pharmacology* 6, S. 149. DOI: 10.3389/fphar.2015.00149.

Nacak, Tanju G.; Leptien, Kerstin; Fellner, Doris; Augustin, Hellmut G.; Kroll, Jens (2006): The BTB-kelch protein LZTR-1 is a novel Golgi protein that is degraded upon induction of apoptosis. In: *The Journal of biological chemistry* 281 (8), S. 5065–5071. DOI: 10.1074/jbc.M509073200.

Noonan, J. A. (1968): Hypertelorism with Turner phenotype. A new syndrome with associated congenital heart disease. In: *American journal of diseases of children (1960)* 116 (4), S. 373–380. DOI: 10.1001/archpedi.1968.02100020377005.

Pagnamenta, Alistair T.; Kaisaki, Pamela J.; Bennett, Fenella; Burkitt-Wright, Emma; Martin, Hilary C.; Ferla, Matteo P. et al. (2019): Delineation of dominant and recessive forms of LZTR1-associated Noonan syndrome. In: *Clinical genetics* 95 (6), S. 693–703. DOI: 10.1111/cge.13533.

Pandit, Bhaswati; Sarkozy, Anna; Pennacchio, Len A.; Carta, Claudio; Oishi, Kimihiko; Martinelli, Simone et al. (2007): Gain-of-function RAF1 mutations cause Noonan and LEOPARD syndromes with hypertrophic cardiomyopathy. In: *Nature genetics* 39 (8), S. 1007–1012. DOI: 10.1038/ng2073.

Rauen, Katherine A. (2013): The RASopathies. In: *Annual review of genomics and human genetics* 14, S. 355–369. DOI: 10.1146/annurev-genom-091212-153523.

Roberts, Amy E.; Allanson, Judith E.; Tartaglia, Marco; Gelb, Bruce D. (2013): Noonan syndrome. In: *The Lancet* 381 (9863), S. 333–342. DOI: 10.1016/S0140-6736(12)61023-X.

Romano, Alicia A.; Allanson, Judith E.; Dahlgren, Jovanna; Gelb, Bruce D.; Hall, Bryan; Pierpont, Mary Ella et al. (2010): Noonan syndrome: clinical features, diagnosis, and management guidelines. In: *Pediatrics* 126 (4), S. 746–759. DOI: 10.1542/peds.2009-3207.

Rössler, Uta; Hennig, Anna Floriane; Stelzer, Nina; Bose, Shroddha; Kopp, Johannes; Søe, Kent et al. (2021): Efficient generation of osteoclasts from human induced pluripotent stem cells and functional investigations of lethal CLCN7-related osteopetrosis. In: *Journal of bone and mineral research : the official journal of the American Society for Bone and Mineral Research*. DOI: 10.1002/jbmr.4322.

Sakai, Taku; Naito, Atsuhiko T.; Kuramoto, Yuki; Ito, Masamichi; Okada, Katsuki; Higo, Tomoaki et al. (2018): Phenotypic Screening Using Patient-Derived Induced Pluripotent Stem Cells Identified Pyr3 as a Candidate Compound for the Treatment of Infantile Hypertrophic Cardiomyopathy. In: *International heart journal* 59 (5), S. 1096–1105. DOI: 10.1536/ihj.17-730.

Santarpia, Libero; Lippman, Scott M.; El-Naggar, Adel K. (2012): Targeting the MAPK-RAS-RAF signaling pathway in cancer therapy. In: *Expert opinion on therapeutic targets* 16 (1), S. 103–119. DOI: 10.1517/14728222.2011.645805.

Savitzky, Abraham.; Golay, M. J. E. (1964): Smoothing and Differentiation of Data by Simplified Least Squares Procedures. In: *Anal. Chem.* 36 (8), S. 1627–1639. DOI: 10.1021/ac60214a047.

Schubbert, Suzanne; Zenker, Martin; Rowe, Sara L.; Böll, Silke; Klein, Cornelia; Bollag, Gideon et al. (2006): Germline KRAS mutations cause Noonan syndrome. In: *Nature genetics* 38 (3), S. 331–336. DOI: 10.1038/ng1748.

Sewduth, Raj Nayan; Pandolfi, Silvia; Steklov, Mikhail; Sheryazdanova, Aidana; Zhao, Peihua; Criem, Nathan et al. (2020): The Noonan Syndrome Gene Lztr1 Controls Cardiovascular Function by Regulating Vesicular Trafficking. In: *Circulation research* 126 (10), S. 1379–1393. DOI: 10.1161/CIRCRESAHA.119.315730.

Shaner, Nathan C.; Lambert, Gerard G.; Chammas, Andrew; Ni, Yuhui; Cranfill, Paula J.; Baird, Michelle A. et al. (2013): A bright monomeric green fluorescent protein derived from Branchiostoma lanceolatum. In: *Nature methods* 10 (5), S. 407–409. DOI: 10.1038/nmeth.2413.

Simanshu, Dhirendra K.; Nissley, Dwight V.; McCormick, Frank (2017): RAS Proteins and Their Regulators in Human Disease. In: *Cell* 170 (1), S. 17–33. DOI: 10.1016/j.cell.2017.06.009.

Staerk, Judith; Dawlaty, Meelad M.; Gao, Qing; Maetzel, Dorothea; Hanna, Jacob; Sommer, Cesar A. et al. (2010): Reprogramming of human peripheral blood cells to induced pluripotent stem cells. In: *Cell stem cell* 7 (1), S. 20–24. DOI: 10.1016/j.stem.2010.06.002.

Steklov, M.; Pandolfi, S.; Baietti, M. F.; Batiuk, A.; Carai, P.; Najm, P. et al. (2018): Mutations in LZTR1 drive human disease by dysregulating RAS ubiquitination. In: *Science (New York, N.Y.)* 362 (6419), S. 1177–1182. DOI: 10.1126/science.aap7607.

Sun, Ning; Yazawa, Masayuki; Liu, Jianwei; Han, Leng; Sanchez-Freire, Veronica; Abilez, Oscar J. et al. (2012): Patient-specific induced pluripotent stem cells as a model for familial dilated cardiomyopathy. In: *Science translational medicine* 4 (130), 130ra47. DOI: 10.1126/scitranslmed.3003552.

Takahashi, Kazutoshi; Tanabe, Koji; Ohnuki, Mari; Narita, Megumi; Ichisaka, Tomoko; Tomoda, Kiichiro; Yamanaka, Shinya (2007): Induction of pluripotent stem cells from adult human fibroblasts by defined factors. In: *Cell* 131 (5), S. 861–872. DOI: 10.1016/j.cell.2007.11.019.

Takahashi, Kazutoshi; Yamanaka, Shinya (2006): Induction of pluripotent stem cells from mouse embryonic and adult fibroblast cultures by defined factors. In: *Cell* 126 (4), S. 663–676. DOI: 10.1016/j.cell.2006.07.024.

Tartaglia, M.; Mehler, E. L.; Goldberg, R.; Zampino, G.; Brunner, H. G.; Kremer, H. et al. (2001): Mutations in PTPN11, encoding the protein tyrosine phosphatase SHP-2, cause Noonan syndrome. In: *Nature genetics* 29 (4), S. 465–468. DOI: 10.1038/ng772.

Tartaglia, Marco; Pennacchio, Len A.; Zhao, Chen; Yadav, Kamlesh K.; Fodale, Valentina; Sarkozy, Anna et al. (2007): Gain-of-function SOS1 mutations cause a distinctive form of Noonan syndrome. In: *Nature genetics* 39 (1), S. 75–79. DOI: 10.1038/ng1939.

Thierry-Mieg, Danielle; Thierry-Mieg, Jean (2006): AceView: a comprehensive cDNA-supported gene and transcripts annotation. In: *Genome biology* 7 Suppl 1, S12.1-14. DOI: 10.1186/gb-2006-7-s1-s12.

Tidyman, William E.; Rauen, Katherine A. (2016): Pathogenetics of the RASopathies. In: *Human molecular genetics* 25 (R2), R123-R132. DOI: 10.1093/hmg/ddw191.

Tohyama, Shugo; Hattori, Fumiyuki; Sano, Motoaki; Hishiki, Takako; Nagahata, Yoshiko; Matsuura, Tomomi et al. (2013): Distinct metabolic flow enables large-scale purification of mouse and human pluripotent stem cell-derived cardiomyocytes. In: *Cell stem cell* 12 (1), S. 127–137. DOI: 10.1016/j.stem.2012.09.013.

Tuveson, David A.; Shaw, Alice T.; Willis, Nicholas A.; Silver, Daniel P.; Jackson, Erica L.; Chang, Sandy et al. (2004): Endogenous oncogenic K-rasG12D stimulates proliferation and widespread neoplastic and developmental defects. In: *Cancer Cell* 5 (4), S. 375–387. DOI: 10.1016/s1535-6108(04)00085-6.

van der Burgt, Ineke; Brunner, Han (2000): Genetic heterogeneity in Noonan syndrome: Evidence for an autosomal recessive form. In: *American journal of medical genetics* 94 (1), S. 46–51. DOI: 10.1002/1096-8628(20000904)94:1<46::aid-ajmg10>3.0.co;2-i.

Wang, Gang; McCain, Megan L.; Yang, Luhan; He, Aibin; Pasqualini, Francesco Silvio; Agarwal, Ashutosh et al. (2014): Modeling the mitochondrial cardiomyopathy of Barth syndrome with induced pluripotent stem cell and heart-on-chip technologies. In: *Nature medicine* 20 (6), S. 616–623. DOI: 10.1038/nm.3545.

Waters, Andrew M.; Ozkan-Dagliyan, Irem; Vaseva, Angelina V.; Fer, Nicole; Strathern, Leslie A.; Hobbs, G. Aaron et al. (2017): Evaluation of the selectivity and sensitivity of isoform- and mutation-specific RAS antibodies. In: *Science signaling* 10 (498). DOI: 10.1126/scisignal.aao3332.

Wilkinson, James D.; Lowe, April M.; Salbert, Bonnie A.; Sleeper, Lynn A.; Colan, Steven D.; Cox, Gerald F. et al. (2012): Outcomes in children with Noonan syndrome and hypertrophic cardiomyopathy: a study from the Pediatric Cardiomyopathy Registry. In: *American heart journal* 164 (3), S. 442–448. DOI: 10.1016/j.ahj.2012.04.018.

Wu, Chunlei; Orozco, Camilo; Boyer, Jason; Leglise, Marc; Goodale, James; Batalov, Serge et al. (2009): BioGPS: an extensible and customizable portal for querying and organizing gene annotation resources. In: *Genome biology* 10 (11), R130. DOI: 10.1186/gb-2009-10-11-r130.

Yamamoto, Guilherme Lopes; Aguena, Meire; Gos, Monika; Hung, Christina; Pilch, Jacek; Fahiminiya, Somayyeh et al. (2015): Rare variants in SOS2 and LZTR1 are associated with Noonan syndrome. In: *Journal of medical genetics* 52 (6), S. 413–421. DOI: 10.1136/jmedgenet-2015-103018.

Yamamoto, Wataru; Asakura, Keiichi; Ando, Hiroyuki; Taniguchi, Tomohiko; Ojima, Atsuko; Uda, Takaaki et al. (2016): Electrophysiological Characteristics of Human iPSC-Derived

Cardiomyocytes for the Assessment of Drug-Induced Proarrhythmic Potential. In: *PloS one* 11 (12), e0167348. DOI: 10.1371/journal.pone.0167348.

Yoon, Seunghee; Seger, Rony (2006): The extracellular signal-regulated kinase: multiple substrates regulate diverse cellular functions. In: *Growth factors (Chur, Switzerland)* 24 (1), S. 21–44. DOI: 10.1080/02699050500284218.

Zhou, Ting; Benda, Christina; Duzinger, Sarah; Huang, Yinghua; Li, Xingyan; Li, Yanhua et al. (2011): Generation of induced pluripotent stem cells from urine. In: *Journal of the American Society of Nephrology : JASN* 22 (7), S. 1221–1228. DOI: 10.1681/ASN.2011010106.

(Human Protein Atlas) 23.03.2021 <https://www.proteinatlas.org/ENSG00000158186-MRAS/tissue>

8 Acknowledgements

I would like to express my deep and honest gratitude to the many people who supported me during the past years during my Ph.D. thesis.

First and foremost, I want to thank Lukas Cyganek for giving me the opportunity for working on this exciting project. His visions and ideas greatly contributed to this project. I learned a lot.

I would also like to thank my thesis committee members Bernd Wollnik, Wolfram-Hubertus Zimmermann, and Ralf Dressel who supported this project with their knowledge in our annual meetings.

Further, I thank Sven Thoms, Laura Zelarayán-Behrend and Katrin Streckfuß-Bömeke for joining the extended examination board.

My warm thanks go to my colleagues Alex, Mandy, Jakob, Oscar and Mario. For your help, the great atmosphere, and guaranteed laughter.

My sincere thanks go to the whole SCU technician team. You taught me all I know about iPSC culture. Laura, Lisa, Yvonne, Nadine, Yvonne, Kerstin and Kristian, thanks for your endless effort to keep the lab running!

A special shoutout goes to the UMG road bike team, especially Leandro and Felix for organizing amazing tours and challenging training sessions. The sunny afterwork rides in the beautiful scenery around Göttingen made me forget all the stressful things.

I also want to thank my parents, and my awesome siblings Kimberley and Marvin for always supporting and loving me as I come.

My final thanks go to my wife Vanessa and my wonderful daughter Hanna. Your love and unbelievable support helped me immensely during the last years of my studies. I know it was challenging for you.